ANKARA YILDIRIM BEYAZIT UNIVERSITY

GRADUATE SCHOOL OF NATURAL AND APPLIED SCIENCES

THEORETICAL AND EXPERIMENTAL INVESTIGATION OF PLASMA-WALL INTERACTION AND MATERIAL RELIABILITY IN FUSION BASED TOKAMAK REACTOR

Phd. Thesis by

Alper PAHSA

Department of Energy Systems Engineering

December, 2023

ANKARA

THEORETICAL AND EXPERIMENTAL INVESTIGATION OF PLASMA-WALL INTERACTION AND MATERIAL RELIABILITY IN FUSION BASED TOKAMAK REACTOR

A Thesis Submitted to

The Graduate School of Natural and Applied Sciences of

Ankara Yıldırım Beyazıt University

In Partial Fulfillment of the Requirements for the Degree of Doctor of Philosophy in Energy System Engineering, Department of Energy Systems Engineering

by

Alper PAHSA

December, 2023

ANKARA

Phd. THESIS EXAMINATION RESULT FORM

We have read the thesis entitled **"THEORETICAL AND EXPERIMENTAL INVESTIGATION OF PLASMA-WALL INTERACTION AND MATERIAL RELIABILITY IN FUISON BASED TOKAMAK REACTOR"** completed by **ALPER PAHSA** under the supervision of **PROF. DR. FAHRETTİN GÖKTAŞ** and we certify that in our opinion it is fully adequate, in scope and in quality, as a thesis for the degree of Doctor of Philosophy.

Prof. Dr. Fahrettin GÖKTAŞ

Supervisor

Prof. Dr. Yıldırım AYDOĞDU

Jury Member

Prof. Dr. Metin AKTAŞ

Jury Member

Prof. Dr. Sefer Bora Lişesivdin

Jury Member

Doç. Dr. Mustafa Kurban

Jury Member

Prof. Dr. Sadettin ORHAN

Director

Graduate School of Natural and Applied Sciences

ETHICAL DECLARATION

I hereby declare that, in this thesis which has been prepared in accordance with the Thesis Writing Manual of Graduate School of Natural and Applied Sciences,

All data, information and documents are obtained in the framework of academic and ethical rules,

All information, documents and assessments are presented in accordance with scientific ethics and morals,

All the materials that have been utilized are fully cited and referenced,

No change has been made on the utilized materials,

All the works presented are original,

and in any contrary case of above statements, I accept to renounce all my legal rights.

Date:

2023, December 29 **Signature:…….**

Name&Surname:ALPER PAHSA

ACKNOWLEDGMENTS

Firstly, I would like to express my sincere gratitudes to my supervisor, Prof. Dr. Fahrettin GÖKTAŞ and Prof. Dr. Yıldırım AYDOĞDU for their tremendous support and motivation during my study. Their immense knowledge and precious recommendations constituted the milestones of this study. Their guidance assisted me all the time of my research and while writing this thesis.

Beside I would like to thank to The Scientific and Technological Research Council of Turkey (TUBITAK) and Ankara Yıldırım Beyazıt University Scientific Research Projects Coordination Unit for their support on this study. This work is supported by the The Scientific and Technological Research Council of Turkey (TUBITAK) under grant number 118F052.

Finally, I would like to thank to my family for encouraging me in all of my pursuits, supporting me in all conditions and inspiring me to follow my career objectives.

2023, December **Alper PAHSA**

THEORETICAL AND EXPERIMENTAL INVESTIGATION OF PLASMA-WALL INTERACTION AND MATERIAL RELIABILITY IN FUSION BASED TOKAMAK REACTOR

ABSTRACT

Fusion reactions involve the nuclei of deuterium (D) and tritium (T), transforming into nuclei of helium (He). However, the repulsion force that exists between two positively charged nuclei obstruct their ability to combine. A collision between two nuclei would require them to be propelled toward each another at exceedingly high velocities resulting in elevated temperatures. The amalgamation of these two atoms at an approximate temperature of 100 million degrees Celsius is required. Plasma is produced when D and T atoms are ionized at this temperature. For the nuclei to merge, the plasma must remain warm.

Tokamak reactors are specifically designed for this purpose. The geometry Tokamak is designed to ensure the confinement of the plasma within the magnetic field. The dissipation of impact-induced heat is hindered. To commence and maintain the reaction, it is imperative that the plasma density and temperature must reach a specific threshold. Approximately 4 kiloelectron volts (keV) of energy is necessary to achieve an initial temperature of about 45 million degrees Celsius. The plasma's movement at high speeds within a magnetic field, generates an electric current, which in turn, creates a secondary magnetic field. The presence of this magnetic field induces irregularities or turbulence in the plasma, causing certain ions to break up and become free from the magnetic field. So that the escaped ions collide with the reactor wall. During the reaction process, the positive and negative ions that escape from the magnetic field environment interact with the walls of the Tokamak, resulting in deformation. As a consequence, the plasma wall gradually degrades, leading to the emission of neutrons into the surrounding environment. The interaction between plasma and the wall is a critical issue that causes distribution in the fusion process in Tokamak reactors. Graphite, Beryllium, Aluminum, and Tungsten are the most resilient materials against ion abrasion in the plasma wall as stated in the literature.

In this thesis we investigate the interaction between plasma and wall materials both theoretically and experimentally. The theoretical part of the thesis is concentrated on investigating the physical and chemical erosion of different wall materials (graphite, aluminum, and tungsten) employed in the fusion reactor due to plasma interaction. This degradation is a result of plasma interactions. The Monte Carlo approach is utilized to examine these erosion effects.

In addition, the study examines the effects of these erosion on the durability and longevity of the reactor's wall material. This study also aims to examine the physical and chemical changes that occur when a plasma of helium ions, created by applying a high direct current (DC) voltage in a vacuum, interacts with an aluminum surface. The interaction of the samples with the plasma, the cracks caused by physical erosion, and the deformations caused by sputtering were determined by employing atomic force microscopy and electron microscopy for structural characterization. The reliability of the material samples is assessed by utilizing the Weibull method to calculate the mean depth of the pits formed on the material's surface as a result of deformations.

Keywords: Tokamak reactors, plasma material interaction, sputtering, structural material reliability prediction.

FÜZYON TABANLI TOKAMAK REAKTÖRÜNDE PLAZMA-DUVAR ETKİLEŞİMİ VE MALZEME GÜVENİLİRLİĞİNİN TEORİK VE DENEYSEL OLARAK İNCELENMESİ

ÖZ

Füzyon reaksiyonlarında döteryum (D) ve trityum (T) çekirdekler birleşerek Helyum (He) çekirdeklerine dönüşür. Bununla beraber, pozitif yüklü iki çekirdek arasında var olan itme kuvveti, birleşme etkilerini engeller. İki çekirdek arasındaki bir çarpışma, birbirlerine doğru son derece yüksek hızlarda itme kuvveti gerektiğinden birbirlerine yaklaşmaları gerekir. Füzyon süreci, yüksek hız ve sıcaklıklara neden olur. Bu iki atomun yaklaşık 100 milyon santigrat derece sıcaklıkta birleşmesi gerekir. D ve T atomları bu sıcaklıkta iyonize olduğunda, plazma üretilir. Çekirdeklerin birleşebilmesi için plazmanın sıcak kalması gerekir.

Tokamak reaktörleri bu amaç için özel olarak tasarlanmıştır. Plazmanın geometrisi, manyetik alan içinde hapsedilmesini sağlayacak şekilde tasarlanmıştır. Böylece, plazma hapsolur. Darbe kaynaklı ısının yayılması engellenir. Reaksiyonu başlatmak ve sürdürmek için plazma yoğunluğunun ve sıcaklığının belirli bir eşiğe ulaşması zorunludur. Yaklaşık 45 milyon santigrat derecelik bir başlangıç sıcaklığına ulaşmak için yaklaşık 4 kiloelektron voltluk (keV) bir enerji gereklidir. Plazmanın bir manyetik alan içinde yüksek hızlarda hareket etmesi bir elektrik akımı oluşturur ve bu da ikincil bir manyetik alan yaratır. Bu manyetik alanın varlığı, plazmada düzensizlik ya da türbülans yaratarak bazı iyonların manyetik alandan kurtulmasına ve reaktör duvarına çarpmasına neden olur. Reaksiyon süreci sırasında, manyetik alan ortamından kaçan pozitif ve negatif iyonlar Tokamak reaktörünün duvarlarıyla etkileşime girerek deformasyona neden olur. Sonuç olarak, plazma kenarı kademeli olarak bozulur ve nötronların çevreye yayılmasına yol açar. Plazma ve duvar arasındaki etkileşim, Tokamak tipi reaktörlerde füzyonun bozulmasına yol açan kritik bir konudur. Bu reaktörlerde Grafit, berilyum, alüminyum ve tungsten kullanılması durumunda plazma duvarında iyon korozyonuna karşı en yüksek dirence sahip olmaktadır.

Bu çalışma, teorik analiz ve deneysel incelemenin bir arada kullanarak plazma ve malzemeler arasındaki etkileşimi araştırmaktadır. Çalışmanın teorik aşamasında,

füzyon reaktöründe kullanılan farklı duvar malzemelerinin (grafit, alüminyum ve tungsten) fiziksel ve kimyasal erozyonunu araştırmaya odaklanmıştır. Bu bozulma plazma etkileşimlerinin bir sonucudur. Bu erozyonları incelemek için Monte Carlo yaklaşımı kullanılarak teorik simülasyonlar ile incelenmiştir. Ayrıca çalışmada, aşınmaların reaktörün duvar malzemesinin dayanıklılığı ve uzun ömürlülüğü üzerindeki etkileri de incelenmiştir. Deneysel çalışma aşamasında ise vakumda doğru akım (DC) voltajı uygulanarak oluşturulan bir helyum iyonu plazmasının alüminyum yüzeyle temas ettiğinde meydana gelen fiziksel ve kimyasal değişiklikleri incelenmiştir. Numunelerin plazma ile etkileşimi, fiziksel erozyonun neden olduğu çatlaklar ve püskürtmenin neden olduğu deformasyonlar, yapısal karakterizasyon için atomik kuvvet mikroskobu ve elektron mikroskobu altında incelenmiştir. Malzeme numunelerinin güvenilirliği ise deformasyonların bir sonucu olarak malzeme yüzeyinde oluşan çukurların ortalama derinlik miktarları kullanılarak Weibull yöntemi ile incelenmiştir.

Anahtar Kelimeler: Tokamak reaktörleri. plazma malzeme etkileşimi, püskürme, yapısal malzeme güvenilirlik kestirimi.

CONTENTS

NOMENCLATURE

Greek Letter Symbols

α	Scale parameter (characteristic life) in Weibull Formula/correction factor in Yamamura formula
β	Shape parameter (slope) in Weibull formula/target Characterization factor in Yamamura formula
γ	Gamma ray/location parameter in Weibull formula
δ	Derivation
Δ	Difference
ε	Reduced energy
θ	The angle of incidence
ρ	Interaction energy between atoms
μ	Micro
Σ	The sum operator

Subscripts

c	Current
exp	Exponential
f	Failure probability
i	Potential energy
j	Electron into electron cloud
n, 0, 1, 2	Denotes the number of the item in formula
N	Number of particle
opt	Optimum
TF	Thomas-Fermi
pi	Pixel
vi	Lowest valley

Acronyms

AFM	Atomic Force Microscope
ASE	Atomic Simulation Environment
ASME	American Society of Mechanical Engineers
Burr III	Generalized logistic function distribution

CERN	The European Organization for Nuclear Research
DC	Direct Current
DEMO	Demonstration Power Plant
EAM	Embedded Atom Model
EDS	Energy-dispersive X-ray spectroscopy
EDX	Energy dispersive X-ray analysis
EMT	Effective Medium Theory
ESP	Electron Stopping Power
EUROfusion	European Union Fusion Projects
EUROfusion WP PFC	Eurofusion Work Package Plasma Facing Components
eV	Electron Volt
FORM	First-order second moment"
Fortran	Formula Translation
IA PrgCS-II	Improved Adaptive Progressive Censoring Type II
IAEA	International Atomic Energy Agency
ImageJ	Image for Java
ITER	International Thermonuclear Reactor
IT	Information Technology
JET	Joint European Thorus
LAMMPS	Large Scale Atomic/Molecular Massively Parallel Simulator
LIDAR	Light Detection and Ranging
MAGNUM-PSI	Magnetised plasma generator and numerical modelling for Plasma-surface interaction
MeV	Mega Electron Volt
MHD	Magnetohydrodynamic
PFC	Plasma Facing Component
RES	Radiation Enhanced Sublimation
RMS	Root Mean Square
SCC	Stress corrosion cracking
SEM	Scanning Electron Microscopy
SORM	Second-order reliability methods
SPM	Scanning Probe Microscope

SSRe	Repeated sample size re-estimation
TOKAMAK	тороидальная камера с магнитными катушками (Toroidal chamber with magnetic coils)
XRF analysis	X-ray Fluorescence analysis

LIST OF TABLES

LIST OF FIGURES

CHAPTER 1

INTRODUCTION

The energy demand resulting from population growth and rising living standards is one of the most challenging issues of the 21st century. Unfortunately, the primary energy sources, fossil fuels, are depleting. Therefore, new energy sources must be identified to replace the extraction of fossil fuels, which has become economically questionable. By combining renewable and conventional energy sources and minimizing greenhouse gas emissions, nuclear energy is one of the only viable solution. The nuclear energy, provides a sustainable energy regime [1, 2].

After exothermic nuclear reactions occur, nuclear energy is produced. The two main nuclear reactions are known as fission and fusion. Nuclear fission is the process by which a heavy, unstable nucleus is divided into more smaller nuclei, releasing vast amounts of energy. Today, nearly all nuclear power facilities rely on nuclear fission reactions.

Nuclear fusion is a type of nuclear process in which two or more atomic nuclei combine to form one or more new nuclei and subatomic particles. This phenomenon is the main power source of the universe, since it is the process producing energy at the center of all stars, including the sun. The nuclear power plants based on fission are in progress in many country. However, generating energy by nuclear fission faces challenges related to radioactive waste management, nuclear reactor security, and the economics of fuel production. In contrast, nuclear fusion is an extremely desirable energy source for future generations due to a variety of reasons. Initially, fusion energy produces no greenhouse gas emissions and runs on abundant, economical, and limitless fuel resources. Second, fusion reactors will generate radioactive waste with a short half-life which is inherently safe.

In a fusion reaction, due to the difference in total mass between reactants and products an energy is generated. However a, temperature of approximately 100 million degrees is required for a fusion reaction to occur. Nuclear fusion is a unique

solution with limitless fuel resources that can be found worldwide. Furthermore, fusion reactors will generate only radioactive waste with a short half-life and will be inherently secure [3-22]. The most well-known fusion reaction involves two hydrogen (H) isotopes, deuterium (D) and tritium (T). This reaction produces a neutron (n) with an energy of 14.1 MeV, which is then used to heat water for generating steam that drives the turbine. Additionally, a helium nucleus (He) with an energy of 3.5 MeV is produced [4, 8, 11, 19]. Due to the charged nature of helium nuclei, they will remain within the reactor and transfer their energy into the plasma to maintain its temperature [5, 6, 9, 10, 15, 19].

The fusion reaction is extremely efficient and produces a large amount of energy with a small amount of fuel; D-T fusion power plant can easily operate for an entire year on 250 kilograms of fuel. Plasma temperature must be held at 100 degree Celsius at least and its energy must be preserved within the plasma without transferring to the container walls for a sufficient duration for the relatively uncommon fusion events to occur. Otherwise, the plasma would transfer its energy with the walls, causing it to cool down and dissipate within the container. Numerous techniques have been discovered, but magnetic confinement and inertial confinement appear to be the two experimental methods most capable of accomplishing this objective [34-44].

After the laser was invented in 1960 at the Hughes Research Laboratory in California, scientists sought to swiftly ignite fusion fuels with a laser to prevent plasma from escaping before being consumed by the fusion reaction. It would be constrained by its own inertia, hence the term "inertial confinement", because implosion relies on inertia to draw nuclei closer together. Laser beams of the order of $10^{14}\,W/cm^2$ and $10^{15}\,W/cm^2$ are directed at a solid particle containing a low-density mixture of deuterium and tritium in the context of inertial confinement. Instantaneously, the laser's energy vaporizes the particle, generating a plasma ambient for a short duration. During the procedure, the density and temperature of the propellant reach levels sufficient to ignite the fusion reaction. The magnetic confinement method uses powerful magnetic fields to contain the heated plasma and prevent it from contacting the reactor walls. Magnetic fields maintain plasma in perpetually looping trajectories

due to the electrical charges on the separated ions and electrons, causing them to follow magnetic field lines. As a consequence, plasma does not come into contact with the interior of the container. There are numerous types of magnetic confinement systems, but only the Tokamak and stellarator devices have been sufficiently developed to be used in a nuclear reactor. Due to its versatility, the Tokamak is considered the most advanced magnetic confinement system [23]. The Tokamak reactor geometry is designed to confine plasma by compressing the magnetic field. This generates various forces in the inner and outer portions of the ring while keeping the plasma away from the reactor walls.

Plasma is confined within a magnetic field in a typical thermonuclear fusion reactor, thereby compelling fusion reagents of sufficient density to fuse. By confining plasma in a magnetic field, plasma is isolated the reactor's first wall. However, high energy ions may escape from the magnetic field and hit the first wall of the reactor, causing it to corrode and become radioactive. On the other hand, helium nuclei resulting from the fusion reaction must also be evacuated from the environment. These nuclei also hit the surrounding walls leading erosion. The greatest erosion occurs in the divertor region, where magnetic field lines deliberately direct lower-energy plasma to the divertor wall. Plasma-first wall interactions and wall materials are the primary focus of fusion research. The produced helium (debris of fusion) must be evacuated from Tokamak reactor. This interaction reduces the lifespan of the divertor and reactor walls and the collapse of the reactor walls causes the release of neutrons into the atmosphere. There many methods developed for removal of He without damaging divertor walls [37, 38, 41, 46, 47, 53, 55, 57, 59, 62, 66].

Graphite, beryllium, molybdenum, steel, and tungsten are the materials that resist the reactor wall attrition in a Tokamak. With its high atomic number and melting point, Tungsten is thought to be the most resistant material to plasma [33, 45, 50, 52, 54, 56, 58, 60].

The reliability of the materials used in the Tokamak reactor against radiation has been the subject of many studies. Methods and applications to estimate the lifetime and reliability of the materials to be used in Tokamak and risk analysis for nuclear fission reactor are reviewed in Ref. [45]. In nuclear fusion reactors, the reliability of

the materials that can be used in Tokamak is still under progress and more studies need to be done to estimate the best material. A summary of recent studies for this aim is given in Ref. [26]. This paper also offers a perspective on structural and thermomechanical analysis of Tokamak. In that review, the methods for breeding blankets, magnets, and diagnostic techniques have also been discussed. The reliability and safety analysis of fusion devices is an additional security concern in scientific literature [26]. It describes how analyses of reliability, availability, maintainability, and inspectability are conducted on international experimental ITER, DEMO, and Wendelstein 7-X fusion reactors to ensure efficient and reliable operations in energy production for researchers [25]. This investigation concentrates exclusively on the fundamental elements of fusion devices. The most widely known plasma research on estimating the structural reliability of industrial plasma activity is the application of surface coating in commercial plasma applications.

In structural reliability applications, probability distributions are widely employed. For instance, in reliability literature, the IA PrgCS-II method is employed as a novel censoring mechanism using a Burr III distribution, and then the Frequentist and Bayesian SSRe model parameter is obtained. According to these dependability analyses, no additional method exists for predicting the Tokamak fusion reactors. This study offers an innovative approach for selecting different materials against plasma and conducting reliability analysis by using the industrial structural prediction method of Weibull prediction to calculate the structural reliability of the reactor walls. To implement a statistical procedure in Tokamak fusion reactors, it is necessary to comprehend the operational process conditions and calculate the stability of the process. Calculations are based on actual experimental data, which also highlights that the results presented in the study resemble the template solution graphs of the Weibull prediction theorem.

Interactions between the structural materials of plasma-tokamak reactor raise numerous concerns. Recent studies have measured waste accumulation in the divertor regions of ITER and DEMO-type reactors. According to experimental fusion reactor research, the effects of alpha particle concentration on plasma operation are examined, and zero-dimensional power and particle balance equations are used to

calculate helium fusion reactions and determine optimal conditions. The research demonstrated that He is an inevitable consequence of the deuterium-tritium reaction. Particularly for ITER and DEMO-class reactors, experiments concentrate on low-activation materials such as steel, SiC ceramic composites, and vanadium alloys. New diagnostic instruments and measurement methods are investigated with the aid of research. Plasma burdens, including the influence of plasma impurities, are investigated on plasma-facing components as part of the EUROfusion WP PFC. As a plasma impurity, it is highly relevant to the study of plasma wall relations,since it exists as an intrinsic impurity in a fusion plasma. During plasma exposure, He has an effect on the surface morphology, causing the proliferation of surface hair. This phenomenon is more prevalent on the the wall material surfaces of the divertor region [27, 28, 48, 49, 53, 56, 61, 62, 64].

The aforementioned phenomena raise the question of how the structural reliability of Tokamak fusion reactors and the design criteria for reactor wall construction should be evaluated. How the durability will be determined based on the specified material? The structural reliability of Tokamak reactors involves evaluating and forecasting of the safety and dependability of reactor building materials. It involves assessing the structural integrity, durability, and effectiveness of materials and components under the extreme conditions of the fusion reactor. To evaluate the structural reliability of Tokamak reactors, it is vital to consider material selection, erosion and damage, heat and stress management, reliability analysis, maintenance, and inspection. Selecting a material that can withstand harsh operating conditions such as high temperatures, intense radiation, and particle bombardment is essential in terms of material selection.

In addition to being a design criteria, the structures of Tokamak reactors must be composed of materials that are inexpensive and extensively used. Aluminum (Al) cannot be used as a wall material in fusion reactors because of its low melting temperature [29]. Without coming into contact with plasma, it is used as an insulator. However, Al can be used as a substitute for beryllium. This is sometimes done because the toxic nature of beryllium particles hinders beryllium research. In this investigation, aluminum is therefore investigated as a test material.

Reliability analysis criteria are indispensable for determining the robustness and ensuring low-maintenance operation of reactor structures. Reliability methods quantify the probability of component failure and estimate the lifetime of reactor components using probabilistic risk assessment and random distribution methods, such as the Weibull distribution. This study investigated the interaction between plasma and Al surface in terms of surface roughness to calculate the Weibull prediction and evaluate the durability of the material.

1.1 Literature Summary

The purpose of study is to determine the material reliability and life cycle calculations of the deformations caused by the physical erosion and sputtering processes resulting from the interaction of materials on the walls of Tokamak-type nuclear fusion reactors focusing the plasma flux, using experimental verification. In this context, the relevant existing literature has been examined. The basic concepts and physical issues related to the subject of the thesis are underlined, engineering problems arising from these physical issues caused by the experimental methods are analyzed. Furthermore, international joint experimental studies in the literature are explored in following paragraphs.

The production of world energy sources is highly unstable and uncertain, and this is not solelydue to technological advances but also environmental, social or geopolitical relations. Rapidly developing countries have generally dependent on energy sources such as fossil fuels, nuclear reactors and alternative energy sources like solar and wind energy sources. As known, fossil fuels contribute to greenhouse effect and global warming. Fossil fuels have a limited reserves and their production is controlled by certain countries as a monopoly. It is known that fossil fuels are cheaper, but everyone knows that costs will rise when fossil fuels run out. In this sense, wind, thermal, wave and solar energy sources will be the leading renewable energy sources used as alternatives to fossil fuels. On the other hand, alternative energy sources are not cheap including environmental and operational costs. In this respect, studies on alternative energy resources proceeds continue to make energy consumption cheaper. Alternative energy sources are expensive to produce but they

have the fewest environmental impacts. However, the production of alternative energy sources still appears to be expensive and varies depending on the climate conditions. Although they have a certain production costs, nuclear energy sources (fission and fusion reactions) are preferred by developing countries due to their high rates of energy production and long-term sustainability. The fission energy of the nuclear energy, as seen in the Fukushima and Chernobyl accident, carries the risk of safety and environmental impacts Therefore, studies on safety engineering of nuclear fission reactors have been continued in light of these issues. On the other hand, nuclear fusion energy is another alternative source of electricity generation, that does not carry any safety risks. It offers high-quality production and intensive research is still being carried out to ensure its endurance [58, 59].

The study concentrates on plasma trapping in nuclear fusion energy systems to ensure the continuous energy and to provide on endurance study of plasma-facing materials, which pose a challenging problem in nuclear fusion reactors. Nuclear fusion has several advantages including minimal greenhouse gas emissions, safety and abundance as a fuel source. Plasma is a crucial aspect of fusion studies. This concept was first studied in 1920. Plasma can be referred to the fourth state of the matter, characterized by ionized gas. In order for a gas to become plasma, certainproperties must be defined. These parameters include plasma formation, plasma temperature, plasma flow, particle density, plasma confinement time. Examples of materials that can form plasma include lightning, sun and sun like stars, fluorescent lamps can be given as examples. Industrial applications of plasma are encountered in various fields, such as military technology, energy production, plasma based particle accelerators, electronic chip production, optics, textiles, paper technology, and natural events. These applications encompass the gas flow, space physics, solid state plasma, gas lasers, controlled thermonuclear fusion, plane turbine blades and the hardening of metals used in automobile parts, hydrogen bombs, nitriding of surfaces against corrosion, and decay processes [60, 61].

Nuclear fusion is the result of two light nuclei producing a heavier nucleus and releasing energy through the nuclear reaction. In fusion energy, the abundant amount of light hydrogen atom nuclei, can be considered as a source of energy because they

are generally lighter nuclei and more stable than heavy radioactive nuclei. In order to accomplish nuclear fusion, the reagent particles must first overcome the electric repulsion between them to get close enough for the attractive nuclear strong force to take over to fuse the particles. However, this process requires extremely high temperatures, if temperature alone is considered in the process. Fusion can not take place naturally due to Coulomb Barrier. Fusion does not occur spontaneously; however when the Coulomb barrier is overcome, the fusion takes place and the nuclei combine quickly with the least amount of energy. The Coulomb barrier is faced as a distance given as (1.1):

$$R = R_a + R_x \tag{1.1}$$

where R_a and R_b are radii of the interacting particles, respectively. The Coulomb barrier is electric potential at this distance.

$$V_C = \frac{e^2}{4\pi\varepsilon_0}\frac{Z_a Z_b}{R} \tag{1.2}$$

The effect of the Coulomb barrier on the fusion reaction is similar to its effect on alpha decay. The deuterium (a heavy isotope of hydrogen) and tritium (a hydrogen isotope with a very low abundance) have a Coulomb barrier of 0.4 MeV for the reaction. This value is small, but it is greater than the incoming energy range of 1-10 keV. The energies of the particles are higher than the Coulomb barrier, and there is a possibility of penetrating barrier similar to alpha decay. There are two important problems in fusion. The first one is the confinement of the plasma and the other is the interaction of the plasma with the materials. During plasma confinement, the most significant problem arisen from the dissipation of energy from the hot plasma fuel to the structural walls, leading to the erosion of the structural wall and posing a major challenge in plasma confinement. To address this issue, there are two methods for plasma confinement: magnetic confinement and inertial confinement. In inertial confinement, the fuel pellet is also confined using lasers and particle bundles. In this method, the fuel pellet is heated and bombarded in all directions simultaneously by a dense particle or photon beam (laser) to achieve confinement.

In the case of magnetic confinement, the fusion is achieved by using the species in the magnetic fields. In basic fusion reactions, very large temperatures are reached by this confinement.

To obtain the predicted energy in a fusion reaction, the reaction must occur at a low temperature. In this case, a large amount of energy will be released, and it will have a large cross section. The substances that will be involved in the reaction should be readily available. Hydrogen isotopes (deuterium and tritium) are easily available because they can be obtained from the vast amounts of water present in the world's seas and oceans. To reheat the plasma, ionized particles need to be obtained, and high energy neutrons must be present to prevent various interactions [62-73].

In the magnetic confinement fusion process, the historical approach has always been to understand the physics of the core plasma. Theoretical foundations and diagnostic technology have advanced, and the core transport properties have been further developed through experiments that allows the study of global energy confinement. In the fusion reactors that used the Tokamak-type magnetic confinement process many years ago, designers dealt with the magnetic topology of the magnetic field lines in the core, and the field lines were collided with the material surfaces. This topology has enabled the management of more intense plasma-wall interactions by using a specially designed target container to direct the plasma away from the core. Although this spatial section is outside the core, the divertor is also known as the boundary layer of the plasma. Thus, plasma encounters, material structures in its environment [74].

In nuclear fusion reactors (such as Tokamak), deformation mechanisms for structural materials around the plasma can occur as follows:

a) The displacement of atoms in the structural material due to collisions with high-energy fusion neutrons. Neutron collisions may cause whole structural material become reactive.

b) The nuclear reactions that result in gas production in the structural material. Hydrogen isotopes may diffuse out of the structural material at high operating

temperatures, However, alpha particles remain in the metal structures, and He forms gas bubbles.

The first wall material exposes to high-energy neutrons, gamma rays and charged fluxes in plasma. The interaction leads to deformation of the walls and limits down the lifetime of the material. Therefore, different materials have been examined and different geometries of the reactor have been tested to prevent the contact of the plasma with structural materials in ITER and DEMO. A strong consensus has emerged in the context of advanced fusion plasma material research after ITER, the largest international study of the world after CERN. In line with the European Union roadmap, the most crucial challenge in achieving magnetic confinement-based fusion is the resolving the issue of reliable exhaust temperature. During projections for ITER, two types of research topic confirmed the importance of boundary layer placement.

Recent studies show that the point towards the magnetic director outside the core was narrow at the spatial region above the plasma flow energy. This heat flow channel width is insensitive to the size of the fusion device and the power flow is outside the core. Achieving alpha fusion output and making transient power inputs in the reactors is very demanding and essentially requires core plasma. In addition, the world's largest fusion reactor device, in the JET (Joint European Torus) Tokamak in the UK implemented by the one-to-one application for the wall materials recommended in ITER: tungsten was used as the plasma-facing region, and beryllium in the walls. In the operational experiments performed in ITER-like JET, it was observed that the walls were reduced by 20% -30% in terms of energy confinement.

However, reduction was improved through nitrogen injection, nitrogen seeding and ammonia production, The use of tritium vaccination planned for JET was found to be unsuitable for technical specification design. In this case, the effects of the boundary plasma, fusion with the core plasma, and the interaction with the wall material have led to the optimization of compatibility. In addition, the material that interact with the plasma determines the feasibility of fusion energy. Nano-scale fibrous structures have been observed on the surfaces of materials exposed to plasma effects such as

tungsten at high temperature. Therefore, safety issues have arisen due to dust formation or vice verse. This means that neutron-induced space formations will be taken into consideration in future fusion devices for materials that interact plasma. For example, in ITER, the possibility of increasing tritium separation in future leads to the risk of impacting field limits, in contrast to tritium. There is a need for tritium retention mechanisms in solids and liquids, including a thorough understanding of tritium transport and the effects of neutron irradiation [75, 76].

Based on the data described above, it has been observed the design of plasma-facing materials is crucial for the manufacture of the nuclear fusion reactors using the Tokamak type plasma magnetic confinement method. In order to create a perfect design, which minimize the effects of plasma flux on the material, especially the physical and chemical erosion issues, sputtering effects, plasma material transport interactions due to neutron radiation, the geometry of the reactor, the material reliability and lifetime of the materials must be initially determined. There have been many studies [77-82] investigating the plasma-material interactions, the reduction of lifetime caused by physical and chemical erosion, reduction of deformation, burrs and residues in the core plasma, fuel dilution and radiation cooling of the core plasma, deformation and continuous erosion of the wall surface, and tritium-related issues. For example, studies have shown that, it is possible to observe the bonding of carbon based directional or reactor walls with H ions, and storage of beryllium (Be) on application-specific carbon (C) or tungsten (W) material in the reactor, depending on the state of different regions. Based on the investigations, the events that happen during plasma material interaction may be summarized as given in Table 1.1:

Table 1.1 Physical Process and Its Physical Name

Process Name	Physical Name
Erosion	Physical Sputtering Chemical Erosion
Transport	Atom ionization Molecule ionization/Molecule Separation Ionized particle and established forces
Re-storage	Reflection/Atomic adhesion Reflection/Molecular adhesion

Process Name	Physical Name
Material Comparison	-

The actual testing of the aforementioned physical events through experimental validation is also an important issue. For example, using the MAGNUM-PSI Linear Plasma device was used to the material selection for ITER. A test setup was installed to observe the effects of plasma on the materials. The device has been tested how both the complex and high heat flux can be managed in components and future fusion reactors. The device was tested on carbon-based materials and heat-resistant metals. Material erosion issues, surface morphology changes, (such as H implantation, and diffusion), and inventory studies in materials were conducted [83-85].

Within the context of plasma fusion reactors, it has been determined that plasma diagnostics for fusion reactions, plasma parameters for fusion reactions, maintenance monitoring IT (information technology) need to be established for ITER. Material reliability calculations, which are generally sought in nuclear predictive maintenance applications, have only been found to utilize Weibull models for nuclear fusion reactors. However, in terms of predictive maintenance, it has been determined that material life cycle calculations are not applied to structural material samples, and physical erosion models included in the reliability calculations have not been investigated as a research subject thus far. All structural predictive maintenance applications have been determined for the industry and research literature pertaining to nuclear fission reactor components [86-93].

This study, aims to investigate the physical sputtering and chemical erosion in Tokamak-type nuclear fusion reactors. Thus, different materials have been examined. However, the cost of determined materials and the acquisition permission processes have resulted in some limitations. In the divertor region, where magnetic field lines deliberately direct low-energy plasma to the divertor wall, the most significant erosion occurs. Beryllium was used for long time as divertor material in Tokamak reactors. However, the toxic nature of beryllium prohibits research on beryllium in the experimental studies. In experimental studies, the use of non-toxic materials instead of beryllium is being considered. Due to its low melting temperature,

aluminum can not be utilized as a wall material in inner core of fusion reactors. Aluminum, however, can serve as a “substitute” for beryllium in the divertor region. In this investigation, therefore, aluminum is used as a test material; therefore, it can be evaluated as a candidate for the wall material.

This study fills a gap in the existing literature and presents promising results in fusion reactor material reliability studies. It also addresses the design issues of the nuclear fusion reactor materials based on physical sputtering and chemical erosion. Especially predictive maintenance calculation models have been developed. The most significant contribution of this thesis work is the rapid development of the material design criteria selection for Tokamak-type nuclear fusion reactors, since, nuclear fusion considered to be the most important source of energy in the future.

This results of this study can be used in industrial plasma applications such as plasma torch, plasma welding device design processes, and plasma sputtering technique for semiconductor production. They can also be applied to satellite / space plasma propulsion engine application calculations, and the development of structural material selection for defense-based fusion-based ammunition in the design of such applications.

1.2 Aim of the Thesis

The aim of this thesis is to study the plasma-wall interaction theoretically and experimentally. In the theoretical method, plasma’s of H, D, T, and He ions are sprayed on graphite, aluminum, or tungsten, and the physical sputtering and chemical erosion are studied using Molecular Dynamics and Monte Carlo methods. In experimental study, a plasma generated by ionizing He in a high potential field is directed on a target material (aluminum) and both physical and chemical influences are investigated. This investigation aims to to predict the reliability and lifetime of material.

CHAPTER 2

THEORETICAL BACKGROUND

2.1 Plasma and Nuclear Fusion Reactions

Plasma is the fourth state of matter. Plasma's ionized. A liquid is generated when a solid is heated enough to shatter the crystal lattice structure. Atoms evaporate and gas forms when liquid is heated. Plasma is generated when gas atoms clash and lose electrons. Ionized gases are special. Most materials are influenced by forces between adjoining locations. Plasma currents, magnetic fields, and electric fields result from charge separation between ions and electrons. Plasma was named by Nobel Prize winner Irving Langmuir, who pioneered the study of ionized gases. In the lab, radio waves or electric currents heat and ionize a tiny volume of gas. Either the container is actively chilled for a longer pulse or its thermal capacity is exploited to prevent it from melting, ionizing, and emitting a brief heating pulse.

A plasma is created by heating a material until it ionizes. Ionization and electron temperature are strongly connected under thermodynamic equilibrium. Plasma in local thermodynamic equilibrium, like many astrophysical plasma, are rare in labs. Ionization processes above thermal equilibrium may form plasma. The lab can create plasma with high or low density, temperature, stability, transience, and more.

Industrialized countries have been using both nuclear and renewable energy resources. Nuclear energy may be generated through two types of nuclear reactions. The first type of the nuclear reactions is called fission reaction, in which a heavy, unstable nucleus is split to less unstable or stable nuclei, and energy is released. On the other hand, in the second type of nuclear reaction Two light nuclei combine to form a heavier nucleus, and energy is again released. This type of nuclear reaction is called a nuclear fusion reaction. This type of nuclear reaction is called a nuclear fusion reaction.

The fuel used in nuclear fission is widely 235U in slow neutron reactors and 238U in fast neutron reactors. In both types of power plants, both the fuel and product species, are radioactive. They also particulate wave-type emitted radiation. Therefore, fission-based nuclear power plants require a high level of security precautions. These precautions are significant against risk of accidents, radioactive fuel supply and disposal of the radioactive wastes. On the other hand, studies have also been done in recent years to design fusion-based nuclear power plants despite many challenging problems. have not been solved yet. The reaction requires two isotopes of H, deuterium and tritium, to combine, which requires 100 million ºC temperatures. Though there is no problem in providing fuel, the high temperature needed to initiate the reaction is a challenging problem in fusion reactions. Because there is no material that can withstand or resist 100 ºC, the reaction must be carried out in another way. There have been two techniques developed so far. In the first technique, fuel is inertial confined in a very small region, and the reaction is initiated by very high-energy laser beams. On the other hand, in the second technique, deuterium and tritium isotopes are confined in the magnetic field region as plasma, and the reaction takes place in the magnetic field region. But in this case, the ions escaped from the magnetic field region strikes the reactor walls and causes erosion on the walls.

2.1.1 Noble Gas Plasma

In plasma literature, noble gases, typically helium or argon, are commonly referred to as "stabilizing" plasma. Temperature and density of electrons in pure He, Ar, and Xe plasma are predicted using zero-dimensional particle with power balance equations and measured using Langmuir probes and literature experiments, respectively. He plasma has the highest electron temperature and the lowest electron density for a given fill pressure and source power [102].

Since it is a noble gas, it is entirely inert to all aerosol materials and is used in situations where hydrogen or nitrogen secondary gases are harmful. He possesses excellent heat transfer properties and a high sensitivity for modulating plasma energy. Plasma is typically preserved in high-temperature or low-pressure conditions due to their inherent high energy. Due to the energy input required to maintain gas ionization and discharge. At atmospheric pressures, it is difficult to sustain a low-

temperature plasma [103]. Additionally, new techniques are being developed to address this concern. In this investigation, He plasma at constant room temperature is used to create a controlled environment of electrical charge and vacuum. Instead of using H, the electrical current would enhance the potential for deterrence, damage, and active reactant.

2.2 Plasma Material Interactions

In this thesis work, concentration is given to plasma material interactions. It is the most problematic issue in design of the spacecraft engines, power fusion reactors, industrial nuclear fusion reactors or nuclear electric propulsion structures. In fusion reactor, a hot plasma of 100 million ºC is confined in magnetic field region to keep plasma away from the chamber wall. However, confinement can not be completely achieved and the particles with the high energy leave the reactor. Moreover, positive charged particles from the edge plasma will crash to the chamber walls. These interactions in long time cause problems as they include high temperature. After a while, the reactor walls can not withstand high temperatures and collisions, and therefore chemical and physical erosion and melting of the reactor walls begin. In plasma-reactor material's interactions, the life time of the reactor wall material, the dust production from the deteriorated wall material and Tritium (T) inventory in the vacuum chamber are important topics to investigate. Figure 2.1 shows in general the possible events that may occur in plasma wall interaction.

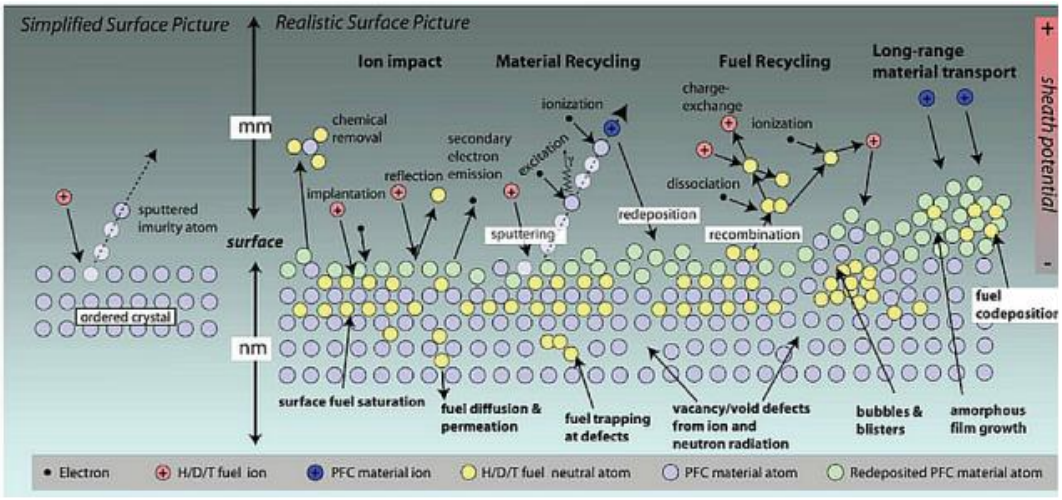

Figure 2.1 Complex Plasma Material Interactions in Solids [69]

In nuclear fusion research, dust particles are created by eroded thick damaged wall materials or thick increments of the wall materials. Dust particles are in nano meter or micrometer size range inside the reactor. Plasma reactor material relations consist of all kind of interactions between the atoms coming from the plasma, like high energy neutrons or H. Surface and bulk of the material are affected by these interactions. These interactions are counted as nuclear stopping, electronic stopping, implantation, reflection and erosion processes.

Nuclear stopping happens when positive charged particles enters to the target material and a bunch of collisions with target atoms until the positive charged particles stop at some depth in the material. This depth is called penetration depth. The collisions between the particles are governed by the interaction potential between them. Another plasma material interaction process is called electronic stopping. It is caused by interaction between atomic trajectories and bound electrons. As the speed of the inelastic collision between electrons decrease in the target, then recoils starts. The energy lost by recoils is spent through the electron cloud into thermal vibrations of the atoms in the target. This process is known for very high energy recoils, where the kinetic energy of recoil is in the order of MeV. Nuclear stopping on the other hand, is not massive at lower recoil energies and for heavier trajectories. It is called implantation plasma material interaction when an atom from the edge plasma comes in close touch with the target material or is thrown backwards during an irradiation event. When a positive charged particle crashes into a material and implants in a substrate, different processes are occurred. The processes in the substrate are trapping, de-trapping, desorption, bubble formation and etc.

Plasma ions can be reflected back from the surface on the reactor wall materials and injected into the plasma. In the case of high-energy atoms, an incident particle gives the target atom its charge and momentum, loses energy in a collision, and leaves the target object after going through a certain depth. When low-energy ions come in, they are reflected close to the top and don't go deep into the material.

Sputtering is influenced by several factors, including surface temperature, the mass ratio of incidence particles to surface atoms, the energy of the incoming particles, the flux, and the angle of the incident ion. Physical sputtering, chemical sputtering, and

electronic sputtering are the three distinct varieties of sputtering mechanisms. Electronic sputtering happens when the high energy electrons such as transition electron microscopy or because of very high energy ion bombardment where the electronic excitation can cause sputtering. Physical sputtering happens in all materials independent of their structures. It is made when the kinetic energy of an approaching particle is transferred to target atoms on the surface layers. Sputtering happens when the energy coming from the direction perpendicular to the surface is greater than the energy holding the surface together. When particles come in and break and make new chemical bonds with the top atoms, this is called chemical sputtering. The shape of the surface material and the temperature of the surface affect chemical sputtering. This leads to thermal desorption and evaporation.

Blistering is another plasma material interaction process that the reactor materials can be eroded by the blistering phenomena under the high irradiation fluxes and implantation fluency. When irradiated atoms are implanted in the target and incremented, they displace the target atoms from their lattice sites, cluster together, and eventually form bubbles.

2.3 Material Reliability in Reactor Environments

Nuclear reactors are robust in terms of energy production to safeguard people, society, and the environment. Safety standards are set during nuclear power plant design. Safety classification, design guidelines based on failure modes, thorough stress analysis, stress categorization, design basis events, failure likelihood, defect tolerance, and leak-before-break are guiding concepts. Engineering constructions have tiny flaws. Defects affect fatigue and fracture most. Defect tolerance is essential [94].

Nuclear power plants use fission reactors, therefore nuclear fusion reactors' reactor structure design fundamentals, including safety, use the same safeguard principles. Safety classification, failure mode-based design criteria, thorough stress analysis, stress categorization, design basis events, failure likelihood, flow tolerance, and leak-before-break were the guidelines.

Nuclear power plant structural parts and components need lifetime, reliability, and risk analysis methodologies and applications. These studies include structural, fracture, probability, material, and fluid mechanics. Accurate data on structure characteristics, loads, supports, relevant aging processes, and environmental variables are needed for a nuclear power plant structural system lifespan study. Probabilistic modeling is suitable for lifespan analysis since events have multiple natural causes. Risk analysis, uses system or component failure probability and consequences [95].

This study estimates failure probability in reliability calculation models for plasma-affected nuclear fusion reactor wall constructions using this technique. The failure mode findings categorize aging degradation processes into rupture and splitting mechanisms. Low-cycle fatigue, high-cycle thermal fatigue, and stress corrosion cracking break components. IAEA's technical definition of aging: regular service circumstances including regular operation and transient situations lead materials to age over time. Age-related changes in power facility metals, concrete, and other materials indicate deterioration. These compounds may modify size, ductility, fatigue resistance, and mechanical or dielectric strength. Fatigue, fracture, embrittlement, wear, erosion, corrosion, and oxidation induce aging-related deterioration. Due to their exposure to high heat and pressure, radiation, reactive chemicals, and synergistic effects, reactors age.

Attrition and sputtering in future nuclear fusion reactors will cause fatigue, fractures, embrittlement, thermal radiation, etc. Fatigue results from repeated mechanical or thermal stress. Material under changing loads that fractures at significantly lower stresses than necessary for a single application load. Cyclic hardening or softening, fissure nucleation, crack propagation, and fracture comprise the fatigue process [96].

Neutron irradiation alters material microstructure and characteristics. The material, neutron flux, flux spectrum, fluency, and irradiation temperature determine the changes. Reactions and fast neutron lattice defects may yield helium. Helium diffuses and produces voids at high temperatures. Thermal aging slowly alters a material's micro structure and characteristics [97].

This study examines structural lifetime and reliability prediction methods and applications for structural systems and components of conventional and nuclear fusion power plant wall structures. As a result of the dispersed nature of many of physical properties of fusion and plasma, probabilistic modeling techniques are acceptable and appropriate for lifetime analyses calculations. Failure probabilities combined with knowledge of the consequences of system or component failure enable risk analyses. A summary of conventional and nuclear power fusion plant wall structures and component environments, as well as a description of the numerous degradation mechanisms affecting fusion power plant wall structure systems and components. On the basis of the consequent failure, Ageing Degradation Mechanisms can be separated into two categories. 1) those that may result in rupture and 2) those that may result in fracture. Components may fracture due to low-cycle fatigue, high-cycle thermal fatigue, and stress corrosion cracking (SCC). Small-diameter piping may rupture due to radiation embrittlement, thermal deterioration of cast stainless steel components, and Vibration fatigue. The prospective rupture-causing mechanisms are anticipated to have a significantly increased risk impact. Probabilistic analysis methods are frequently derived from deterministic analysis methods, with one or more model parameters considered probabilistic [30-35]. In reliability predictions the there are probabilistic analysis procedures are first-order second moment (FORM) methods, second-order reliability methods (SORM), and mean-value methods. Failure probability is frequently defined as the average frequency with which the specified failure event is anticipated to occur during a specified period of operation, typically one year. When calculating the likelihood of failure, it is crucial to account for the rate of future deterioration of all potential mechanisms. Interactions between mechanisms (e.g., corrosion and attrition) will accelerate the rate of degradation over time. Unpredictable factors such as excess, misconduct, and inadvertent injury should be presumed to occur at a constant average rate [72-74].

R is closely related to the failure probability and expresses the likelihood that a component will not malfunction as follows:

$$1 - P_f = R \tag{2.1}$$

A rigorous assessment of structural dependability involves taking into consideration all sources of uncertainty that may influence the component or system's failure. Clearly, this entails accounting for all fundamental quantities entering the problem as well as the uncertainties resulting from a lack of knowledge and idealized modeling. These concepts are known as fundamental variables. They represent common engineering quantities such as component diameter, wall thickness, material and content density, yield strength, maximum operating pressure, maximum operating temperature, corrosion rate, etc.

The procedure for structural reliability analysis is summarized as follows:

1. Identify all significant modes of function failure for each event of failure.
2. Formulate a failure criterion or function for each occurrence of failure.
3. Determine the sources of uncertainty influencing the event's failure.
4. Calculate the probability of failure or reliability for each failure event and, where necessary, combine these probabilities to assess the failure probability or reliability of the structural system.
5. Consider the input sensitivity of the reliability results, such as fundamental variables and parameters.
6. Compare the evaluated reliability to a standard to determine if it is sufficient.

The first-order reliability method (FORM) can manage any continuous distribution. However, the manner in which it manages truncated distributions may result in significant defects in the reliability analysis. When truncated random variables exist, it is necessary to increase accuracy.

In this study, the focus was on truncated probability distributions that result from domain restrictions on their original probability distributions. The original distributions analyzed in this article are those that are commonly employed in FORM and selected FORM method is Weibull reliability distribution. Weibull distributions are commonly applied to material failure distribution data in structural reliability calculations. Due to the fact that a Weibull distribution with three parameters can be

adapted to the distribution shape of material failure data, the Weibull distribution can be used to model a wide range of life behaviors. In Weibull distribution, employing a usage measure unsuitable for the failure mechanism under consideration [95, 96].

CHAPTER 3

MATERIALS & METHODS

The objective of this study is to determine the material reliability calculations of the deformations caused by the physical sputtering processes resulting from the interaction of the candidate reactor wall materials (tungsten, aluminum, beryllium, and graphite) with Tokamak type nuclear fusion reactor wall materials that face the plasma flux by employing simulating the theoretical calculations of sputtering yield and the boundary energies and experimental work to calculate the reliability of the material life cycle. Therefore, the subject and scope of the study are directly related to and overlap with the aforementioned subsidiary objectives.

3.1 Materials

This study utilizes aluminum (Al) in the experimental configuration as both anode and cathode pellets, serving as a representative material for the Tokamak reactor wall structure under investigation. This particular substance is widely recognized and extensively studied in the realms of literature, industrial structural engineering, aviation, and energy constructions. For instance, it finds application in a diverse range of commodities, encompassing cans, foils, window glass, aircraft components, and structures for space satellites. The low density, non-toxicity, high thermal conductivity, and corrosion resistance of aluminum can be attributed to a specific cause. Additionally, it has the capability to undergo machining processes and its form can be altered. The material in question possesses the characteristic of being non-magnetic and non-sparking. The most reliable sources of information and the sixth element with ductile properties. Copper exhibits excellent electrical conductivity, rendering it suitable for application in certain electrical transmission lines. The material in question is less expensive than copper and possesses a relatively low density.

When subjected to a vacuum, the process of evaporation of aluminum (Al) results in the formation of a reflective coating that exhibits great reflectivity for both light and

heat. The material lacks the ability to undergo deformation similar to that of a silver coating.

Aluminum has an atomic number of 13. The substance exhibits a correlation with oxygen, resulting in the formation of a defensive oxide layer upon exposure to atmospheric conditions. Aluminum exhibits a silver appearance and possesses the ability to reflect light. Aluminum (Al) is a post-transition metal that belongs to the boron group. It possesses a face-centered cubic crystal structure and is characterized by metallic bonding, which involves the sharing of electrons in the outermost energy levels of its constituent atoms. Despite being classified as a metal, aluminum exhibits these properties. The crystal metal structure of aluminum has similarities to that of lead and copper, since the size of a unit cell of aluminum may be compared to that of the other aforementioned metals [24].

In the context of experimental research aimed at simulating the plasma environment of a Tokamak reactor, helium plasma is employed. The effective confinement of high-density plasma within Tokamak reactors is crucial for efficient power generation, as it prevents any undesirable contact between the high-energy plasma and the surrounding reactor wall environment. Plasma material interactions are present in Tokamak type fusion reactors during both regular operation and off-normal scenarios, such as plasma disturbances. The generation of heated plasma gases is facilitated by various components, including uncombusted hydrogen fuel, fusion byproducts like helium, plasma electrons, and contaminants. The plasma itself consists of a mixture of particles, namely ions, electrons, and neutrons. After neon, he is the second-most reactive noble gas. In all typical settings, it exhibits inertness and exists as a mono atomic entity. The individual under consideration possesses a relatively low atomic mass, resulting in higher values of thermal conductivity, specific heat, and sound speed in the gaseous state, relative to other gases with the exception of hydrogen. In extremely hostile conditions such as outer space, he exists in a plasma state. For instance, stars exhibit the plasma state. In these particular environments, the properties exhibit notable distinctions from standard conditions. Within the plasma state, electrons exhibit a lack of attachment to the atomic nucleus, hence giving rise to a notable degree of electrical conductivity. Even in a state of

partial ionization, it exhibits a significantly elevated level of conductivity. The element possesses an atomic number of two, denoting the number of protons in its nucleus, and exhibits a mass of 4.00 atomic units, indicating the sum of protons and neutrons within its atomic structure.

3.2 Theoretical Methods

In the theoretical study, physical erosion and sputtering rates of Be, Al, C, and W used to meet plasma in the Tokamak reactor against neutron and He ions were calculated using a molecular dynamic Monte Carlo simulation model. This procedure is more effective and efficient than the previously mentioned methods. When conducting computer simulation executions, it is simple to establish the modeling context's boundaries and expedient to perform calculations on the molecular structure. LAMMPS Simulation Fortran Code Framework software and ASE (Atomic Simulation Environment) in Python [101] for energy levels were used for this purpose. Neutrons (H+) and helium (+) interactions with Be, Al, C, and W were investigated using the open source ASE Monte Carlo simulation software program. Physical sputtering yields, chemical sputtering yields, back scattering yields, total sputtering yields, and radiation enhanced sublimation (RES) were calculated as a consequence of the investigation of candidate materials for the reactor wall. The ASE package program is modified to examine the H-W interaction and it was determined whether the Lennard Jones and Morse potentials were suitable for the H-W interaction with test studies. In the experimental work there are two calculation methods are also used; Weibull reliability prediction and Optical Roughness computation. The detailed explanation is given also given in this section.

3.2.1 Calculation of Total Sputtering Yield

Sputtering yield is one of the most essential concepts in plasma-wall interaction. The yield of sputtering is the number of particles removed per particle that strikes the wall [37].

$$Y = \frac{A}{B} \tag{3.1}$$

In equation (3.1), A is the numer of particles removed and B is the number of incoming ions. As well as being held by the target, incoming ion atoms interact with the target atom and cause it to shatter. Therefore, sputtering is dependent on the properties of both the incoming ion (energy, mass, and kinetic energy) and the target atoms (atomic mass, surface binding energy, surface texture, and crystal orientation). Surface damage will occur if the kinetic energy of the bombardment particle is greater than the lattice displacement energy of the target atoms. The lattice displacement energy is the energy required to move the target element one atomic distance from its original position.

$$Y(E_0, \theta_0) = \beta \alpha N \; S_n(E_0) \tag{3.2}$$

In equation (3.2), β denotes target characterization factor (surface binding energy, crystal orientation) , N shows the density of atoms in the target, α shows the correction factor defined by the rate of the target atom mass over incoming ion mass and S_n denotes the nuclear stopping cross section. The preceding statement about diminishing yield is extremely general. The sputtering yield is also dependent on the bombardment energy (Eo) and θ_0 the angle of incidence of the incoming ions when analyzed comprehensively. If the electronic stimulation of the target is disregarded, a series of elastic scatterings is also conceivable.

Sputtering yield, considering elastic collisions and atomic recoil in the target. It can also be stated as is a factor that defines the target's properties, such as surface binding energy and crystal orientation. N represents the atomic density at the target, is the correction factor defined as the ratio of the target atoms to the incoming ions, and Sn is the nuclear arrest. The formula for cross section is calculated in sputtering yield equation in MD process is given in ref. [105]. Yamamura calculates the sputtering yield under normal incoming conditions based on the literature as follows [104]. In this ref [104] the backward sputtering yield is calculated which is proportional to the energy that is accumulated on the target surface:

$$Y(\Lambda_0) = \frac{\alpha(M_2 / M_1)}{U_S} S_n(E) \tag{3.3}$$

In the above formulation E is the incident energy, and U_S, is the surface binding energy, which is equal to sublimation energy. $S_n(E)$ is the nuclear stopping cross section, and $\alpha(M_2/M_1)$ is energy-independent function of the mass ratio between the target mass M_2 and the ion mass M_1. That is correlated with the equation (3.1) in simplest symbolic denotion. $\Lambda_0=3/4\,\pi^2 C_0$ denotes calculable constant which is the nuclear stopping cross section at low energies. The nuclear stopping cross section at low energies is given below:

$$\frac{dE_0}{dx} = -NC_0E_0 \tag{3.4}$$

E_0 denotes the energy of the recoil atom, N is the number density and:

$$C_0 = \frac{\pi}{2}\lambda_0 a^2 BM \tag{3.5}$$

where λ_0 and a_{BM} are known as the result of the low-energy inter atomic (Born-Mayer) potential, e.g. $\lambda_0=24$ and $a_{BM}=0.219$ A. When these parameters are used, $\lambda_0=0.042$. This value is used to determine the empirical formula of sputtering yield that is given in ref. [104]:

$$Y = 0.042\frac{\alpha(M_2/M_1)S_n(E)}{U_S}[1-(E_{th}/E)^{1/2}] \tag{3.6}$$

where E_{th} is the threshold energy of sputtering. In this case if the Littmark's treatment for the light-ion sputtering inelastic stopping effect is manipulated on equation (3.6) then Yamamura new empirical formula takes the form:

$$Y = 0.042\frac{\alpha(M_2/M_1)}{U_S}\frac{S_n(E)}{1+0.35U_S S_{e(\varepsilon)}}[1-(E_{th}/E)^{1/2}]^2 \tag{3.7}$$

In the above equation $S_e(\varepsilon)$ shows Lindhard's electronic stopping cross section and ε denotes the reduced energy. For the above equation if the least square method, the best fit-values of α and E_{th} in equation (3.7), 190 type of ion-target combinations are calculated in ref. [104]. Also the mass ratios are also graphed in ref. [104] against α and

$$\alpha_{II} = \{\ 0.10+0.155\,(M_2/M_1)^{0.73}\ M_2/M_1 < 50$$

$$\alpha_{II} = \{0.321+0.0332\ (M_2/M_1)^{1.1}\ M_2/M_1 > 50 \qquad (3.8)$$

Then the calculation of of ξ_{II} is given as:

$$\xi_{II} = \frac{E_{th}}{U_S} = 1.5[1 + 3.8(M_2/M_1)^n]^2/\gamma \qquad (3.9)$$

In the above equation the $\gamma = 4M_1M_2/(M_2/M_1)^2$, n=0.834 for $M_2/M_1>1$, and n=0.18 for $M_2/M_1< 1$. In order to know the Z_2-dependence of the deviation from α_{II}, the average deviation of the best-fit α for each target material:

$$Q = \frac{1}{K}\sum_{i=1}^{K} \alpha(M_2/M_1)/\alpha_{II}(M_2/M_1) \qquad (3.10)$$

in equation (3.10) i shows the i-th ion. If someone employs the Z_2-oscillation of the Q values whose parameters are systematically deviated in unity for atoms in column IV of the periodic table:

$$\alpha(M_2/M_1) = Q(Z_2)\alpha_{II}(M_2/M_1) \qquad (3.11)$$

when α_{II} is swapped with a better agreement between the empirical formula and the measured data can be obtained. In order to consider some rational to discuss the present Z_2-oscillation of the Q value. Initially, it can be possible to present Z_2-oscillation can be potential for the elastic collision between the between the low-energy recoil atom and the target atom. In this study, EAM potential is selected in MD calculations. In the Hartfree-Fock calculations in equation (3.5) λ_0 and a_{BM} is depending on the atomic number of the target material. Secondly the surface binding energy is not equal to the sublimation energy for the whole target atoms. It is already known that the sublimation energy is thermodynamic quantity, where the sputtering process is a dynamical process and the interatomic bond of the bulk crystals deformed with the elastic collisions. The linear cascade theory that the energy distribution of the sputtered atoms has the maximum at $E=U_S/2$, it can be concluded that the present Z_2-oscillations of the Q value is originated from the nuclear stopping

cross section at low energy. In other words, λ_0 in equation (3.3) shows the Z_2 - oscillation.

3.2.2 Molecular Dynamics

As part of the simulation experiments, molecular dynamics (MD) calculations were conducted with the open source code package program Large Scale Atomic/Molecular Massively Parallel Simulator (LAMMPS) [38]. MD involves solving Newton's classical equations for N elements in a predetermined simulation cell. According to Newton's classical equations, the force acting on an atom and its position are defined as follows:

$$F_i(t_0) = m_i \dot{r}_i(t_0) = \frac{fU}{fr_i(t_0)} \tag{3.12}$$

$$r_i(t_0 + \Delta t) = r_i(t_0) + r_i(t_0)\Delta t + \frac{1}{2} r_i(t_0)[\Delta t]^2 \tag{3.13}$$

Using the embedded-atom model (EAM) [100], the interatomic interaction potential (U) was calculated. Other potentials are also found in the literature such as Lennard Jones and Morse Potential and Effective Medium Theory [98, 99]. In EAM, i. potential energy for an atom, j. electron into the electron cloud of the atom, the sum of the energy resulting from embedding and the interaction energies between pairs of atoms is given as:

$$U = \sum_i G_\alpha(\sum_{i \neq j} \rho_\beta(r_{ij})) + \sum_{i,j(i \neq j)} U_{\propto\beta}(r_{ij}) \tag{3.14}$$

In numerical uses, it is said that the simulation cell starts with a suitable crystal structure. The virtual cell was made with three layers. First, the atoms in the layer stayed where they were supposed to be. The second layer was the temperature, and the plasma hit the third layer on top. The simulated cell is the same size as the unit cell of the crystal, and its orientations were found to be the same. They put the atoms at the points of the grid and wrote down where they were. For the simulation in the study, (30, 30, 30) unit cells were picked. To make sure that the modeling cell accurately shows how a real temperature system works. The system was brought to

thermal balance by using the integration method on the system's periodic boundary. As the simulation cell got bigger on its way to reaching thermal balance, conditions were set up. The edges of the original computer cell are set up the same way every time. To reach thermal balance, modeling cells of different sizes are made. It makes sure that the computer cell always has the same number of atoms. The system was in thermal balance after about 10,000 simulated steps. The machine's temperature stays the same. In the second stage, the top layer no longer needed to have a periodic boundary condition.

At third step 1–5 keV ion beam was used to bombard the surface of the simulation cell (100). The ion beam was situated 10 above the top stratum (on the z-axis) and an initial kinetic energy was provided. The bombardment simulation was repeated 2,000 times with 0.01 fs time increments, and the simulation was repeated 60 times as a function of the kinetic energy of the ions. Physical sputtering yield values were determined by counting neutral ions five centimeters above the surface of the target. In numerical applications, physical sputtering yield and chemical erosion yield are calculated using the generalized equations derived from the data obtained from Monte Carlo simulations utilizing empirical equations.

3.2.3 Large Scale Atomic/Molecular Massively Parallel Simulator (LAMMPS) Method

LAMMPS is a computational program that employs classical MD to simulate the behavior of collections of particles in various states, such as solid, liquid, or gas. The software has the ability to simulate systems at several levels, including atomic, polymeric, biological, solid-state (such as metals, ceramics, and oxides), granular, coarse-grained, and macroscopic. This is achieved by utilizing a wide range of interatomic potentials and boundary conditions. It is feasible to create models of 2D or 3D systems that vary in size from a small number of particles to billions [38].

While LAMMPS may run on personal computers or individual laptops, its primary purpose was to be used on parallel computing platforms. It is compatible with parallel and serial machines equipped with the MPI message-passing library. These encompass supercomputers, distributed-memory clusters, multicore servers with

shared memory, and multi-CPU servers. Furthermore, certain parts of LAMMPS have the capability to handle OpenMP multithreading, vectorization, and GPU acceleration. LAMMPS is coded in C++ and requires a compiler that is at least compatible with the C++-11 standard. The previous versions were built using F77, F90, and C++-98. Expanding the capabilities of LAMMPS by incorporating other features like force fields, atom kinds, boundary conditions, or diagnostics is a relatively simple procedure [38].

LAMMPS implements Newton's equations of motion to simulate the behavior of a system consisting of interacting particles in a comprehensive manner. A solitary particle can encompass a mesoscopic or macroscopic quantity of matter, such as an atom, molecule, or electron, or a conglomerate of atoms known as a coarse-grained cluster. Although most of the interaction models used in LAMMPS are short-range, there are also a few long-range models included. LAMMPS employs neighbor lists to track adjacent particles. The lists are designed to be efficient for systems that consist of particles with short-range repulsive interactions, hence preventing the local particle density from reaching unacceptably high values. This contrasts with the methodologies used in modeling gravitational bodies or plasma, such as the development of galaxies.

LAMMPS utilizes spatial decomposition and MPI parallelization to divide the simulation domain into subdomains with equal processing cost. Each subdomain is assigned a dedicated processor. Processors communicate about "phantom" items located at the edges of their subdomain. Furthermore, it is possible to incorporate acceleration through GPU and achieve multithreading parallelization by employing particle decomposition [38].

3.2.4 Monte Carlo Method

The Monte Carlo technique is a simulation approach that calculates the state of a system consisting of N particles in a constant volume V at any temperature T. The method was named after the mathematician and computer scientist who developed it. The Monte Carlo approach is based on the numerical solution of a problem that simulates the motion of objects interacting with their surroundings. This method

takes into consideration interactions between bodies as well as interactions between bodies and their environments. In the context of classical physics, the term "partition function" is defined as [115]:

$$Q=c\int dp^N dr^N exp[-H\ (r^N,p^N)/k_N\ T] \tag{3.15}$$

In this case, the coordinates of the N particle are denoted by r^N , c denotes rate constant and its momenta are denoted by p^N . The Hamiltonian of the system is denoted as $H(r^N, p^N)$. Hamiltonian is the energy of an isolated system and consists of the sum of kinetic and potential energy terms expressed in terms of the coordinates and momentum of the particles (H=K+U). In order to symbolize the physical constant $A(r^N, p^N)$ is denoted as:

$$(A)=\frac{\int dp^N dr^N A(p^N,r^N)exp[-H(r^N,p^N)/k_N T}{\int dp^N dr^N\ exp[-H(r^N,p^N)/k_N T]} \tag{3.16}$$

Since kinetic energy is a quadratic function of momentum, the integral over momentum can be easily performed analytically. Therefore, the average of a function that depends only on momentum can be easily calculated. The real problem is $A(r^N)$ function average calculation. The Monte Carlo Method makes it possible to solve this problem, which is impossible to solve analytically and numerically. In Monte Carlo technique in general $\int dp^N exp[-U(r^N)/k_N T]$ does not interested with the integral. In actual sense:

$$(A)=\frac{\int dr^N exp[-\frac{U(r^N)}{k_N T}]A(r^N)}{\int dr^N\ exp[-U(r^N)/k_N T]} \tag{3.17}$$

Interested with the above rate. Metropolis [105] developed Monte Carlo technique in numerical calculation form.

$$Z\equiv \int dr^N exp[-U(r^N)/k_N T] \tag{3.18}$$

If the above function is defined as a new form as in the following:

$$N(r^N)\equiv \frac{exp[-U(r^N)/k_N T]}{Z} \tag{3.19}$$

It gives the probability density of the system being in a configuration around r^N. In this case, it can be clearly said that N>0. If random points can be produced in the configuration space according to this probability distribution ($N(r^N)$), the number of points produced in the unit volume around r^N is It will be $n_i = LN(r^N)$. Here L is the total number of points produced. In this case:

$$\langle A \rangle \approx \frac{1}{L} \sum_{i=1}^{L} n_i A(r^N) \tag{3.20}$$

While the Monte Carlo method is applied in practice, the system initially uses the Boltzman factor $\exp[-U(r^N)/k_N T]$ as a start state (o) r^N configuration is prepared. The initial configuration may correspond to a uniform crystal lattice. Then, the system is randomly displaced by Δ relative to its initial position. This new r^N configuration is symbolized as n. This trial configuration is known as Boltzman factor $\exp[-U(r^N)/k_N T]$. It is then decided whether this trial configuration can be accepted or not.

The basic condition in the assumption is that, on average, the probability of the system being in n configurations is N(n). In both Molecular Dynamics and the Monte Carlo Method, a key indicator of whether a trial configuration will be accepted is the monitoring of energy at each step. In both Molecular Dynamics and the Monte Carlo Method, a key indicator of whether a trial configuration will be accepted is the monitoring of energy at each step.

Quantities such as physical spraying efficiency and chemical erosion efficiency are calculated numerically by using the Monte Carlo technique in plasma surface interaction. Then, analytical expressions are fitted to the numerical data obtained for practical applications. Physical spray efficiency based on experiment and Monte Carlo numerical data:

$$Y^{phy}(E_0) = QS_n(\varepsilon)\left[1 - \left(\frac{E_{th}}{E_0}\right)^{\frac{2}{3}}\right]\left(1 - \frac{E_{th}}{E_0}\right)^2 (\cos\alpha)^{-f} \exp(f[1 - (\cos\alpha)^{-1}]\cos\alpha_{opt}) \tag{3.21}$$

When it comes to plasma surface contact, the Monte Carlo method is used to do numerical calculations on physical sputtering yield and chemical erosion yield. The

results of this step are then used in practical applications, where analytical formulas are applied to the numerical data collected. The following is a summary of the results of experiments and Monte Carlo simulations about the yield of physical sputtering:

It is presented together with. Both Q and the threshold energy are considered to be foot parameters here. The energy of the particle that made the first contact is denoted by E0. Here Q and threshold energy are fit parameters. Eo is the energy of the incident particle in eV and $\varepsilon = E_0/E_{th}$. Thomas-Fermi energy is given as:

$$E_{TF} = 30.74 \frac{M_1+M_2}{M_2} Z_1 Z_2 (Z_1^{2/3} + Z_2^{2/3})^{1/2} \tag{3.22}$$

Here, M1, M2, Z1 and Z2 are the masses and atomic numbers of the corresponding ion and target atom, respectively. The nuclear stopping cross section is:

$$S_n(\varepsilon) = \frac{0.5 ln(1+1.2288\varepsilon)}{\varepsilon+0.1728\varepsilon^{0.5}+0.008\varepsilon^{0.1504}} \tag{3.23}$$

Chemical erosion efficiency based on experiment and Monte Carlo numerical data

$$Y^{Chem} = Y^{term}(1 + \frac{250}{M_1} Y^{dam}) + Y^{surface} \tag{3.24}$$

Yterm is the thermal erosion efficiency resulting from damage caused by incoming ions (Ydam) deterioration thermal erosion efficiency. The incoming beam to the target surface deterioration efficiency is given as:

$$Y^{dam}(E_0) = QS_n[1 - (\frac{E_{dam}}{E_0})^{2/3}](1-(\frac{E_{dam}}{E_0})^2 \tag{3.25}$$

3.2.5 Weibull Reliability Prediction Method

Failure probability is often described as the mean frequency with which the stated failure event would be anticipated to occur in a particular period of operation, generally one year. This frequency is the predicted number of times that the failure event would take place over the provided time period. When determining the likelihood of a failure, it is essential to take into account the pace at which all conceivable mechanisms will continue to degrade in the foreseeable future.

Interactions between processes (such as corrosion and fatigue, for example) will cause the rate of deterioration to accelerate over the course of time. It is reasonable to suppose that a constant average rate of occurrence will be experienced by factors that cannot be readily foreseen, such as overload, overuse, or unintentional damage. R, which stands for reliability, is directly connected to the chance of a component failing, and it indicates the probability that a component will not fail as follows:

$$1 - P_f = R \tag{3.26}$$

A thorough evaluation of the structural reliability of a component or system requires taking into consideration all potential sources of uncertainty that might contribute to the component's or system's failure. This unquestionably necessitates taking into consideration all of the basic quantities that are being introduced into the situation, in addition to the uncertainties that result from a lack of information and the use of idealized models. These are known as "basic variables," and there are many more. Common engineering quantities that are represented by them include component diameter, wall thickness, density of the material and contents, yield strength, maximum operating pressure, maximum operating temperature, and corrosion rate, among others. The following is a concise summary of the structural reliability analysis procedure:

1. Determine all of the key ways in which the function failed to perform for each failure occurrence.
2. Conceive of a failure criteria for each failure occurrence, as well as a failure function.
3. Determine, the causes of the unpredictability that are contributing to the outcome of the event.
4. Evaluate the failure probability or reliability of the structural system by first, calculating the likelihood of failure or reliability for each failure event, and then combining the results of these calculations wherever it is required.
5. Take into account, the degree to which the reliability outcomes are affected by the input, such as the fundamental variables and parameters.

6. Determine, if the level of dependability that has been reviewed is adequate by comparing it to a benchmark.

The first-order reliability method, also known as FORM, is the approach that is used the most often, and it is capable of dealing with any continuous distribution. However, the manner in which it deals with truncated distributions may cause the reliability analysis to include significant mistakes. When truncated random variables are present, there is a pressing need to make the accuracy better. One of the techniques provided by FORM is used to pick a Weibull prediction computation with three parameters. In the field of structural reliability calculations, Weibull distributions are often used for the analysis of material failure distribution data. Because of their form and relatively straightforward nature, Weibull method distributions are well-suited for modeling skewed positive failure data. Three-parameter Weibull Distribution equation is given as follows [105]:

$$R(t) = e^{-(\frac{t-\gamma}{\alpha})^{\beta}} \tag{3.27}$$

t is the irradiation period, β is the shape parameter (slope), α is the scale parameter (characteristic life), and γ is the location parameter. The dependability distribution graph origin displacement is usually assumed as =0 in computations. Failure probability is:

$$F(t) = 1 - R(t) \tag{3.28}$$

$$1 - F(t) = e^{-(\frac{t}{\alpha})^{\beta}} \tag{3.29}$$

where γ=0 and with 0 < F(t) < 1.

$$ln\left(ln\frac{1}{1-F(t)}\right) = \beta lnt - \beta ln\alpha \tag{3.30}$$

In order get an equation in the form of y = mx + n, let

$$y(t) = ln\left(ln\frac{1}{1-F(t)}\right), m=\beta \text{ and } n=-\beta ln\alpha \tag{3.31}$$

Bernard Approximation for Median Ranks can be used to obtain an estimate of the unreliability for each failure. Bernard Approximation of Median Rank is given as follows:

$$F(t) = MedianRank = \frac{Rank-0.3}{N+0.4} \tag{3.32}$$

where rank is the order number in data set table and N is the maximum number of orders in the table set.

3.2.6 Optical Roughness Method

In ImageJ software optical roughness is calculated based on the surface roughness statistics based on a topographical images. Surface roughness may be thought of as the property of a surface that prevents it from being smooth, and it is thus connected to the human sense of the surface texture (haptic perception). From a mathematical point of view, it is connected to the spatial variability structure of surfaces, and by definition, it is a multiscale property. Additionally, it is a multiscale property. Depending on the fields that are taken into consideration, several interpretations and meanings of it may be found. Roughness, which may also refer to surface roughness, is a component of surface finish, which is also known as surface texture. It may be measured in terms of the degrees to which an actual surface departs from its ideal shape in terms of the direction of the normal vector. If these variations are significant, the surface may be described as rough, and if they are negligible, the surface can be described as smooth. In the field of surface metrology, roughness is often understood to be the component of a measured surface that has both a high frequency and a short wavelength. However, in order to guarantee that a surface is suitable for a certain purpose, it is sometimes important to have knowledge of both the amplitude and the frequency of the surface in question. In ImageJ software the input is an image or stack's pixel values denotes the distance, z, to a surface. The calculated roughness values are [106]:

- Ra: Arithmetical mean deviation: arithmetic average of profile height deviations from the mean line on the image.

$$R_a = \frac{1}{l_r}\int_0^{l_r} |z(x)|dx \tag{3.33}$$

- Rq: Root mean square deviation: root mean square average of profile height deviations from the mean line on the image.

$$R_q = \sqrt{\frac{1}{l_r}\int_0^{l_r} z(x)^2 dx} \tag{3.34}$$

- Rku: Kurtosis of the assessed profile: measure of the asymmetry of the profile about the mean line on the image.

$$Rku = \frac{1}{R_q^4}\left[\frac{1}{l_r}\int_0^{l_r} Z^4(x)dx\right] \tag{3.35}$$

- Rsk: Skewness of the assessed profile: measure of asymmetry of the profile about the mean line on the image.

$$Rsk = \frac{1}{R_q^3}\left[\frac{1}{l_r}\int_0^{l_r} Z^3(x)dx\right] \tag{3.36}$$

- Rv: Lowest valley (given by the min measurements): value over assessment length on the image pixel.

$$Rv_i = |min\ z(x)|;\ R_v = \frac{\sum_{i=1}^{n} R_{vi}}{n} \tag{3.37}$$

- Rp: Highest peak (given by the max measurements): value over assessment length on the image pixel.

$$Rp_i = |max\ z(x)|;\ R_p = \frac{\sum_{i=1}^{n} R_{pi}}{n} \tag{3.38}$$

- Rt: The total height of the profile: summing the average Rp and Rz value based on the image pixel values.

$$Rt = R_{zi} = Rp_i + Rv_i \tag{3.39}$$

3.3.1 Metallographic Observations

In order to investigate the surface morphology of metals and alloys, an optical microscope is typically utilized. They are referred to as microscopes. Reflective mirrors are used to shape the light beams before they are collected from the source of illumination. is then dropped onto the surface of the prepared sample. A variety of light reflection angles were observed from the surface of the sample. Images are formed when the beams travel through the objective and the eyepiece of the microscope. Only results with a connection to a healthy internal structure can be obtained from sample surfaces that have been perfectly polished. It is really challenging to acquire photos. Due to the fact that the entire surface of the sample is flat and the reflection from the surface Because the light beams are reflected at the same angle, a single-phase color is produced in the image that is formed [107].

On the sample surfaces, this is not the case at all. Several specifics and specifics of the etched surface, in accordance with their places according to reflections, become distinct and image. The examination of rocks and minerals, as well as the detection of flaws on the surfaces of metals and the localization of crystal grain boundaries in metal alloys, are all common applications for metallographic microscopes. Vertical illumination is utilized by this type of microscope, in which the light source is housed within the microscope tube [108]. In this study Nikon LV100ND is used as metal microscopy to analyse the physical structure of the anode and cathode pellet surfaces of Al. The Metal Microscope magnifies 50x, 100x, 200x, and 500x. Pre- and post-experiment mid surface samples were analyzed.

3.3.2 Scanning Probe Microscopy (Atomic Force Microscope)

The scanning probe microscopy (SPM) technique known as atomic force microscopy (AFM) has a resolution that has been proved to be on the order of fractions of a nano meter. This is almost a thousand times greater than the optical diffraction limit. Using a mechanical probe, the information is collected by "feeling" or "touching" the surface of the object. Accurate scanning is made possible by piezoelectric elements, which are able to carry out minute but accurate and precise movements in response to an electronic signal. The atomic force microscope does not actually make use of

any nuclear force, despite its name [114]. AFM has three capabilities; force measurement, topographic imaging and manipulation. Force measurement is based on the force measurements between the probe and the sample object as a function of their mutual instance. In imaging, reaction of the probe to the force that samples on the object form a three dimensional topographical image at a high resolution. Manipulation capability of the AFM is based on the forces between the needle and the object for changing the characteristics of the sample object by measuring of the mechanical stiffness or adhesion strength, conductivity or surface potential [109]. After the metallic observations, the experimental anode and cathode pellets are observed under the Ambios Q-Scope 250 model AFM. In this AFM, topographic surface measurements such as RMS and Sa are performed. were done at each time after the experiment. After the experiment is examined, AFM (Atomic Force microscope), a high-resolution scanning probe microscope, measures the materials' roughness. Each Al pellet was cleaned, polished, and photographed. The technique measured NCS-16 cantilever at room temperature and ambient conditions. Image processing was 1 Hz. Non-contact AFM analysis captures topography pictures. AFM digital pictures of examined locations. Figure 6 graphs Al anode and cathode plate AFM surface roughness data. AFM calculates ASME B46.1 surface roughness and average peak.

The ASME B46.1 standard defines Sa (Mean surface roughness) as the arithmetic mean of the profile height deviations from the mean line along the assessment length. Sa is the average of surface peaks and valleys observations. Surface roughness (RMS) is the root mean square of profile height deviations from the mean line across the assessment length. ASME B46.1 includes it [39, 40]. Sa and RMS calculate surface roughness differently. Sa is the surface roughness average of tiny peaks and valleys. A surface with tiny peaks and valleys has a Root Mean Square. Al's dependability is determined by RMS and Sa values. Table 3.1 shows AFM measured surface RMS and Sa values for Al anode and cathode samples bombarded with He plasma at different times.

3.3.3 Scanning Electron Microscopy (SEM) and ImageJ Software Analysis

A form of electron microscope known as a scanning electron microscope, or SEM for short, creates images of a sample by moving a focused beam of electrons across its surface as the sample is being scanned. Through their interactions with the atoms in the sample, the electrons produce a variety of signals, each of which is encoded with information regarding the surface topography and chemical make-up of the sample. To create an image, the position of the electron beam is merged with the intensity of the detected signal after it has been scanned using a raster scan pattern. A secondary electron detector, also known as an Everhart-Thornley detector, is used in the most common mode of a scanning electron microscope (SEM). This detector detects secondary electrons released by atoms that have been stimulated by the electron beam. The topography of the specimen is one of the factors that determines the maximum number of secondary electrons that may be detected and, as a result, the maximum signal strength. Some SEMs are capable of achieving resolutions that are superior to one nanometer. In a normal scanning electron microscope (SEM), specimens can be examined in a high vacuum; in a variable pressure or environmental SEM, specimens can be observed in a low vacuum or wet conditions; and with specialized equipment, specimens can be observed at a wide range of cryogenic or higher temperatures [110].

In the study, a Field Emission Scanned Electron Microscope HITACHI SU5000 Scanned Field Emission Scanned Array Microscope model brand is used. It displayed Al pellet surface details with different magnification scales. SEM measurements are performed at room temperature (25 °C). For anode and cathode, gray-scale value images are produced for different magnification scales under SEM. Then these images are analyzed with the ImageJ software. ImageJ software is an open source Java programming language based image processing software at the National Institutes of Health and the laboratory for Optical and Computational Instrumentation. It is open source type “Public Domain” class licence as a software. This software can compute the area and pixel value statistics of the given user criteria. It measures distances and angles, generate histograms, line profile plots. This software can use standard image processing functions as in contrast manipulation,

sharpening, smoothing, edge detection, median filtering and so on. In the study ImageJ used for analyzing the optical roughness features of the SEM images of Al anode and cathode pellet surfaces. These images are used to calculate the following optical roughness parameters, respectively:

- Ra: Arithmetical mean deviation
- Rq: Root mean square deviation
- Rku: Kurtosis of the assessed profile
- Rsk: Skewness of the assessed profile
- Rv: Lowest valley (given by the min measurements)
- Rp: Highest peak (given by the max measurements)
- Rt: The total height of the profile

The above parameters are calculated for each SEM image for the anode and cathode of the pellet for different He plasma process times. The above optical roughness parameters were calculated using the open-source application ImageJ [111].

It is a widely used research application in scientific image processing studies. Also, a surface mesh plot is performed for the surface images under SEM to see the peaks and valleys of the image.

3.3 Experimental Methods

A model of plasma-wall interaction experiment was designed. Plasma wall-surface interaction can be observed using this setup. Surface deformations and material dependability are measured. Figure 3.1 shows the study's experimental design.In the setup, 3x3 cm Al pellets are prepared. As an initial process of the experiment, Al pellet surfaces are polished and surface is cleaned. It is a long process and 6 process inputs with anode and cathode with the same material pureness is prepared. 6 processes are based on the He plasma for different time processes. Before the experiment, all of the anode and cathode surfaces are analyzed under the metal microscope and taken the images. Then vacuum environment is prepared to create

He plasma in a boiler environment to model the reactor as simple sense. In this setup, a vacuum pump purged the plasma boiler tube's air. After He entered the tube, a high DC voltage between the Al cathode and anode ionized the gas to create plasma. Plasma effect on Al anode/cathode plates. These plates were tested. The study abandoned the Al boiler and built a quartz boiler (tube) due to insulation concerns and arcing. The Langmuir probe is not used because the experiment focuses on physical surface effects on the Al anode and cathode surfaces. The boiler receives the same amount of vacuum and hydrogen gas for regulation. The tube's plasma density could not be measured.

Figure 3.1 shows a high DC potential producing a plasma beam. Ionizing He requires a 10 kV DC voltage source between the cathode and anode of an evacuated glass hollow tube. He ions and electrons hit aluminum anode and cathode plates. Figure 3.1 shows the plasma-producing distance between the anode and cathode plates is 5 cm. A quartz tube is repeatedly vacuumed to a 10^{-3} Torr vacuum with the mechanical vacuum pump and filled with He gas from the gas tank to make He plasma which is shown in Figure 3.2. The testing setting was 25 °C and 30%–50% relative humidity. It was a glass tube. Experimental environmental conditions were stable. Repeat this five to six times until the tube is airless and filled with hydrogen gas from the input end from the gas tanks. A tiny pipe is added to the quartz tube's departure end after stabilizing hydrogen gas. The water-filled container receives this quartz tube conduit. This requires stable He gas in the quartz tube and 100 ml/min He gas at the input end under atmospheric pressure. He gas flowed 100 ml/min at 99.99% purity. Experimental setups realizations and their lidar view during the experimental work can be seen in Table 4.1. In the experimental setup Iphone 12 pro lidar sensor was used at room temperature 25 °C. It operates at the 8XXnm wavelength, and uses Photon Counting Detector and Vertical Cavity Surface Emitting Lasers. It creates a photon cloud and depth graphical view of the experimental setup plasma view. It used for the purpose of showing how electron flows between the anode and cathode pellets are observed during the process with different times.

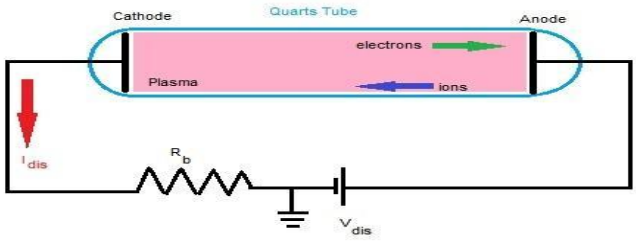

Figure 3.1 Experimental Setup Schema

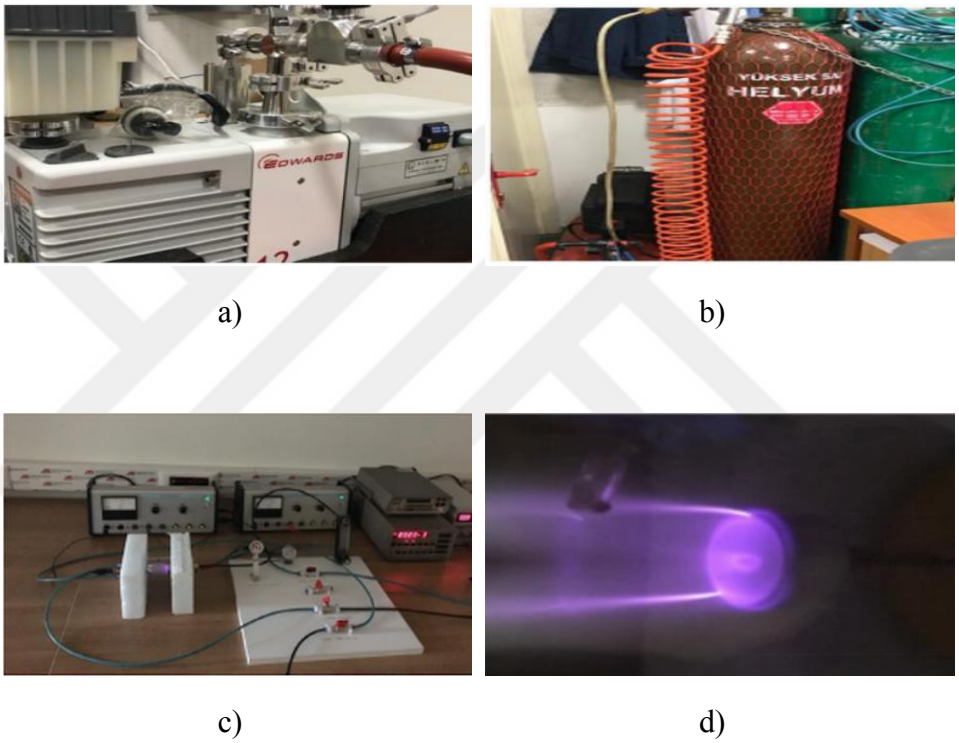

a) b)

c) d)

Figure 3.2 a) Mechanical Vacuum Pump, **b)**Gas Tanks connections, **c)**Experimental setup and its connections, **d)**Generated Helium Plasma,

The experiment used six aluminum particle samples. At the cathode and anode, two plates were irradiated for 60, 120, 180, 240, 300, and 360 minutes. Plasma affects anode and cathode surfaces.

3.3.4 Energy Dispersive X-ray Analysis with SEM

The SEM-EDS analysis is a non-destructive analytical approach (to the sample), however in contrast to the XRF analysis, which may be performed in-situ without the removal of the sample, the SEM-EDS analysis does need the removal of the sample. Irradiating the sample material with electrons causes the substance to emit x-rays that are distinctive to the elements that are present in the sample [112].

When analyzing a sample with a SEM, a number of distinct signals each provide their own unique piece of information. Backscattered electrons, for instance, provide images with contrast that contain information about the changes in the atomic number, whereas secondary electrons produce topographic information about the object they are examining. However, X-rays can also be employed as a signal to provide chemical information when a scanning electron microscope (SEM) is combined with an elemental analysis data collector (EDX).

In order to comprehend the process by which these X-rays are produced, one must first keep in mind that each atom contains a one-of-a-kind number of electrons that are located in a certain range of energy levels. Under typical circumstances, these places are associated with certain shells, each of which possesses a distinct set of energies. The EDX analysis is carried out by directing an electron beam at the innermost layer of an atom. This causes an electron to be ejected from the atomic layer, leaving behind a positively charged electron hole. When one electron is removed from its orbit, it can attract another electron from a neighboring outer shell to move in and take its place. This difference in energy can be released in the form of an X-ray as the electron travels from the outer shell of the atom, which has a higher energy level, to the inner shell, which has a lower energy level. This X-ray has an energy that is peculiar to the transition that this element is going through. A silicon drift detector is used to capture the X-rays that are released throughout the procedure. This detector then measures the signal and uses software to analyze the results of the measurement. Visualizing the chemical information can be accomplished in a number of different ways, including elemental mapping and line scanning. In essence,

these methods are all equivalent. X-rays can be utilized in this manner to determine the identity of each component that is present in a sample [113].

During the examination under the SEM microscope, the surface element characterization of the Al anode and cathode pellet is performed. This is important to understand the which output elements are occurred after the He plasma process. EDS analysis device used on Al pellet anode and cathode surfaces was HITACHI SU5000 Scanned Field Emission Scanned Array Microscope.

CHAPTER 4

RESULTS & DISCUSSION

This is the first study to estimate TOKAMAK reactor wall material dependability and lifespan. It will also contribute to material interaction research on physical erosion and spraying processes for plasma-resistant wall materials.In this chapter all of the theoretical modelling results, optic and spectroscopic measurements are given as in the following subsections. The results presented in detailed form are given in the following subsections.

4.1 Theoretical Work Results

In theoretical section of the work, a molecular-dynamic Monte Carlo simulation model was used in this investigation to determine the rates of physical erosion, chemical erosion, and sputtering that occur when neutrons and He ions come into contact with the materials Be, Al, C, and W that are utilized to meet plasma in the Tokamak reactor. In this context, the open-source software ASE Monte Carlo simulation package was used to investigate the interaction of neutrons (H+) and He+ with Be, Al, C, and W. The results of this investigation were found to be consistent with the predictions made by the package. Physical sputtering yields, chemical sputtering yields, back scattering yields, total sputtering yields, and radiation-enhanced sublimation (RES) were all computed as a result of the investigation of the potential materials for the reactor wall. We estimated the total sputtering yield of H, He, and D ions off the surfaces of Be, C, W, and Al materials because these are the materials that are employed as plasma countering materials in the Tokamak reactor. The equations that were utilized may be found in the Method-Theoretical Work section. The sputter yield was computed as a function of the kinetic energy of H, He, and D ions, and the results are presented in Figure 4.1, figure 4.2 and figure 4.3, respectively. In following graphs, the calculated values of atom sputtering yield, ion energy, physical sputtering efficiency, chemical erosion yield, backscattering yield, radiation enhanced sublimation (RES) yield. Calculated results are performed based

on the Monte Carlo simulation using equations that are implemented in Lammps code explained in Chapter 3 Monte Carlo method section.

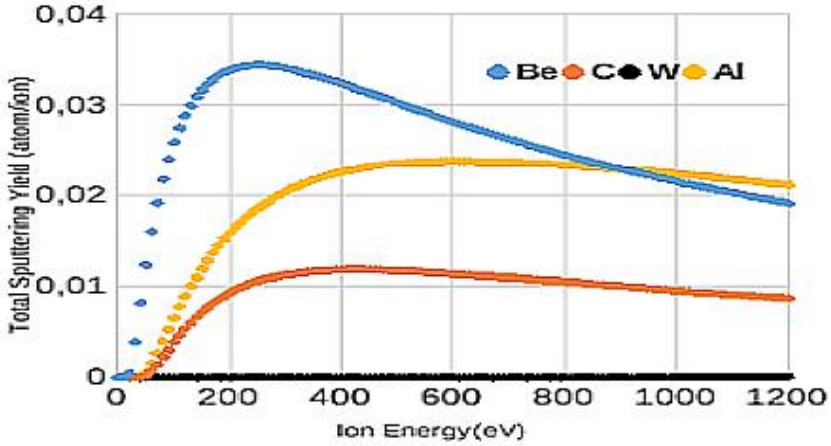

Figure 4.1 Atom sputtering yield of H from Be, C (Graphite), W and Al surfaces

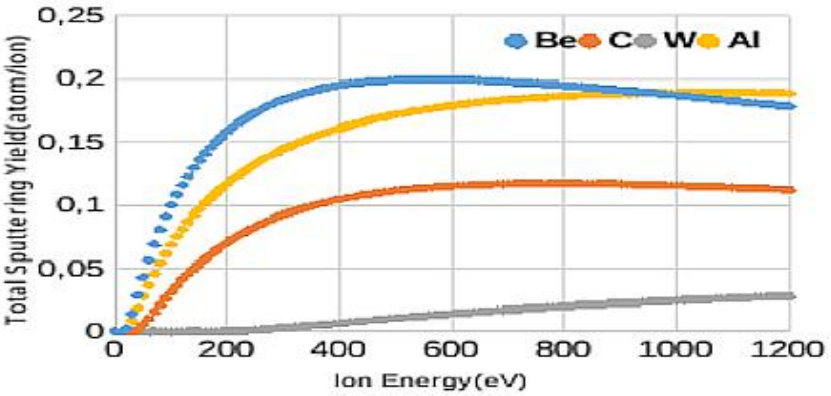

Figure 4.2 Atom sputtering yield from He's Be, C (Graphite), W and Al surfaces

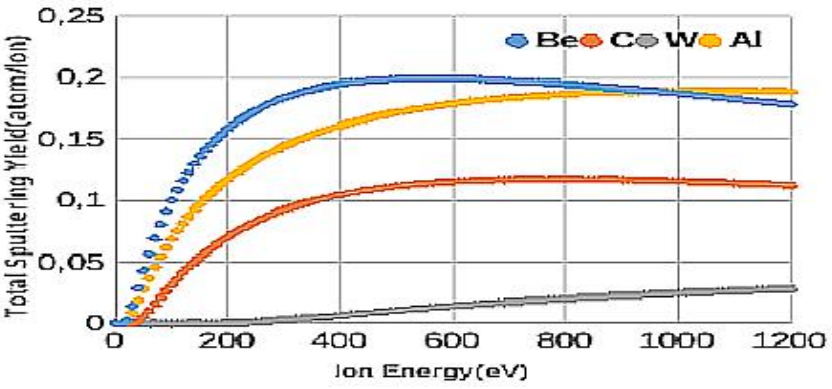

Figure 4.3 Atom sputtering yield from D's Be, C, W and Al surfaces

From the plotted graphs of the theoretical calculation results between Figure 4.1, Figure 4.2, and Figure 4.3, the minimum sputtering yield of atoms affected by H, He, and D can be determined as W. This is also the case in the experimental investigations of performed in Europe experimental fusion Tokamak reactors (JET, STELLARATOR), where W is chosen as the primary wall material for the ITER demonstration reactor. Since the ITER design is currently comprised of W plates that are installed in the reactor wall as a mono block, it has already been tested on hot plasma, with W proving to be the most resistant material. As shown in Figure 4.1, Figure 4.2, and Figure 4.3, as the plasma temperature rises, the sputtering effects, which are calculated as the total sputtering yield, produce W as the predominant material. Be is a candidate material for excellent thermal loading and minimizing the radiation losses of the sputtered H, He, or D plasma atoms. Nevertheless, based on the graphs of the theoretical works on sputtering yield, it is the third material with the maximum sputtering yield in Figure 4.1, Figure 4.2, and Figure 4.3. The final materials Al is the soft metal crystal in Figure 4.1, Figure 4.2, and Figure 4.3 with the maximum sputtering yield and the smallest atomic number. It is affected by plasma ions of H, He, and D. Al is not the only element utilized in nuclear fusion reactors. It is combined with various alloys. Compared to Be and W, it has the lowest melting point.

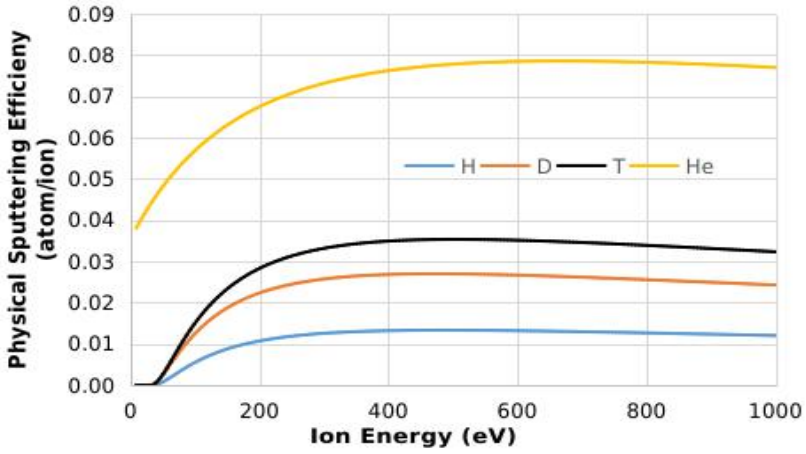

Figure 4.4 Variation of physical sputtering efficiency depending on the energy of H, D, T and He ions

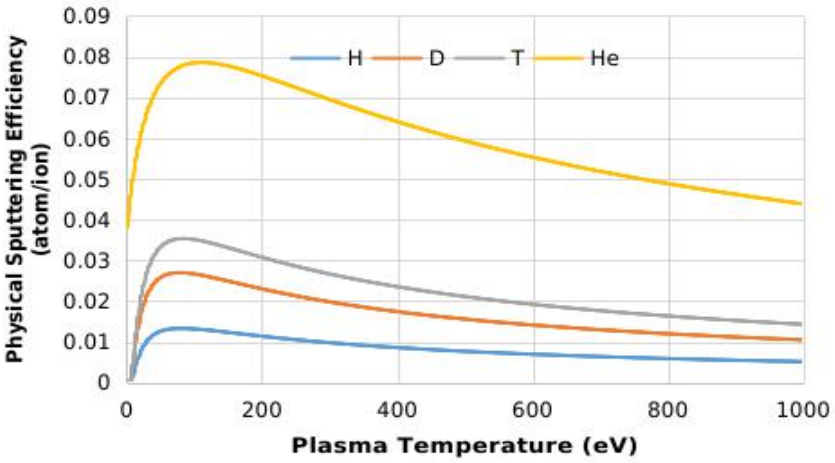

Figure 4.5 Variation of physical sputtering efficiency depending on the plasma temperature

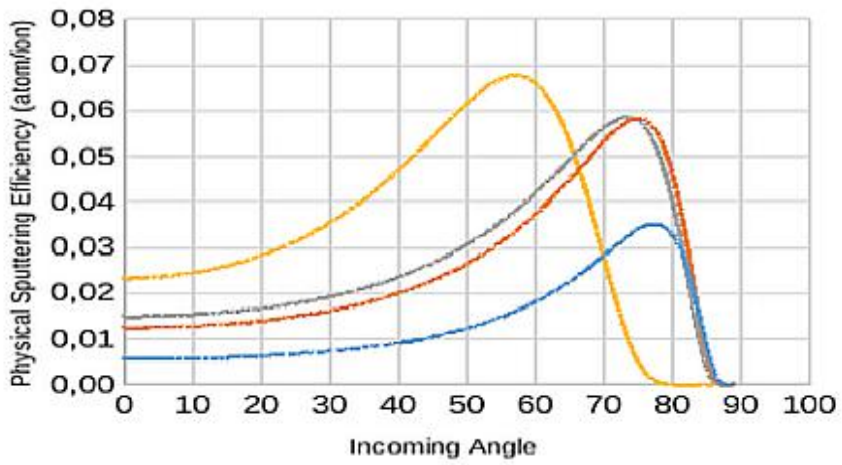

Figure 4.6 Variation of physical sputtering yield with plasma temperature

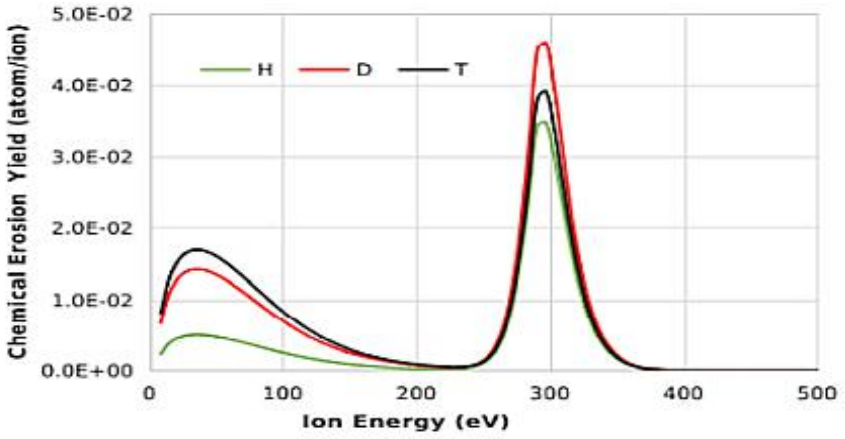

Figure 4.7 Variation of physical sputtering yield with the angle of incidence of ions

For graphite bombarded with H, D, T, and He ions, the physical sputtering yield values calculated using the sputtering yield calculation using Molecular Dynamics, Lammps, and Monte Carlo processes described in the Method section as a function of kinetic energy, incidence angle, and plasma temperature are depicted in figures 4.5, 4.6, and 4.7, respectively.

The variation in chemical erosion yield as a function of ion energy is depicted in Figure 4.8. In the majority of studies published on graphite, the chemical erosion yield is calculated only for the low-energy region. Therefore, no surge was observed around 300 eV. At this energy, this peak indicates that the chemical erosion of the target material is at its apex. At an energy level of 300 eV, the chemical attrition caused by deuteron was observed to be the greatest. As evidenced by the graphs, the physical sputtering yield increases as the bombardment ion mass increases in all four instances. This is to be anticipated for somatic stuttering. On the other hand, the maximal physical sputtering yield was observed at the same location for all three hydrogen isotopes, while it was observed at a lower angle for the He ion. Based on the diagrams, it was determined that the target material was subjected to intense physical sputtering up to a certain energy value, after which the physical sputtering became stable. According to the angle of incidence, the physical sputtering yield is greatest when the ions strike the target surface at an angle between 50 and 80 degrees.

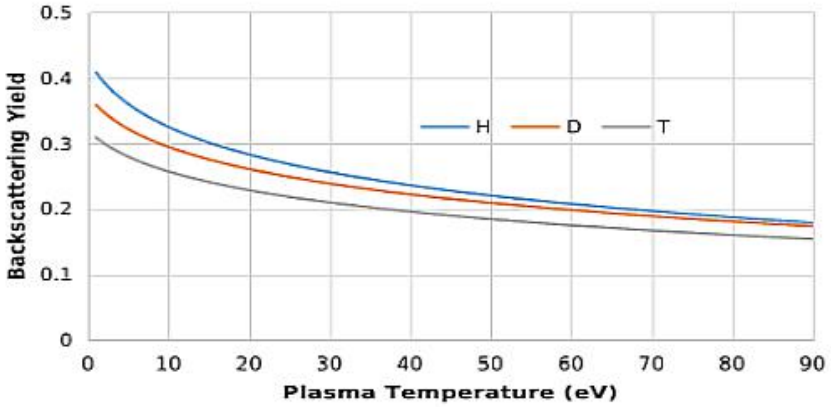

Figure 4.8 Variation of back scattering yield with temperature of H, D and T ion plasma

The PSI open source code based on the Kinetic Monte Carlo simulation approach was also used to calculate the yields from chemical erosion, back scattering, RES (Radiation Enhanced Sublimation), and thermal evaporation in this work. The Yamamura method was used to determine the amount of chemical erosion, back scattering yield, RES yield, and temperature increase in the target material caused by a beam of 1013 ions impinging on the graphite surface. Figure 4.9 The yield from back scattering varies with ion energy, and this variation is described. Since ESP (electron stopping power) is capable of back scattering low-energy ions, it stands to reason that the back scattering yield is highest at low plasma temperatures and diminishes with increasing temperature.

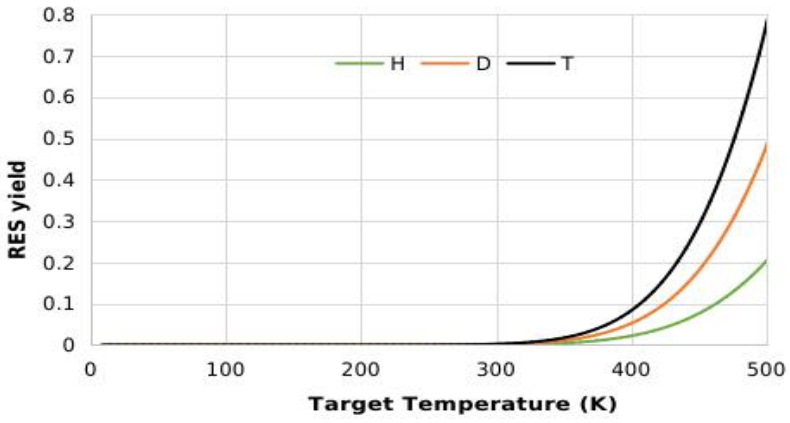

Figure 4.9 Variation of RES yield with temperature of graphite target

RES yield varies as a function of graphite target temperature, as depicted in Figure 4.9. When graphite is heated to high temperatures, a phenomenon called radiation-enhanced sublimation (RES) occurs as a result of an increase in the ratio of the number of graphite (C) atoms released to the number of ions in the plasma beam.

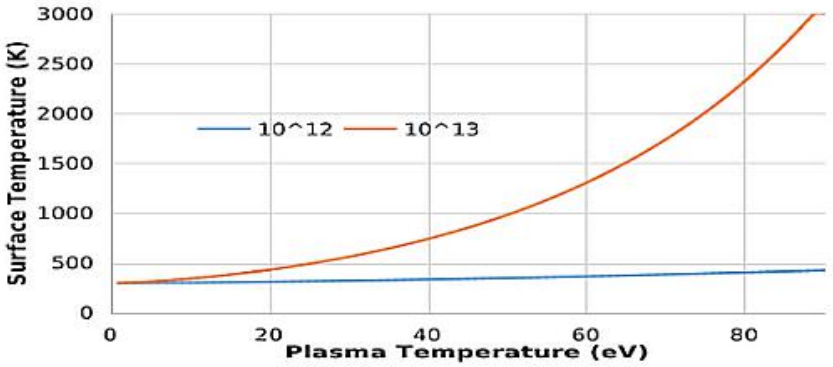

Figure 4.10 Variation of back scattering yield with temperature of H, D and T ion plasma

The backscattering variation with temperature in the graphite target is demonstrated as a function of the ions' energy in Figure 4.10. As depicted in the diagram, the augmentation in the energy of the plasma beam results in a non-linear escalation in the temperature of the target material. Furthermore, it is evident that the augmentation of ions plays a crucial role in elevating the temperature of the target substance. In instances involving 10^12 ions, the temperature rise experienced by the target surface falls within the range of 300–500 K. Conversely, when dealing with 10^13 ions, the temperature escalation reaches up to 3000 K.

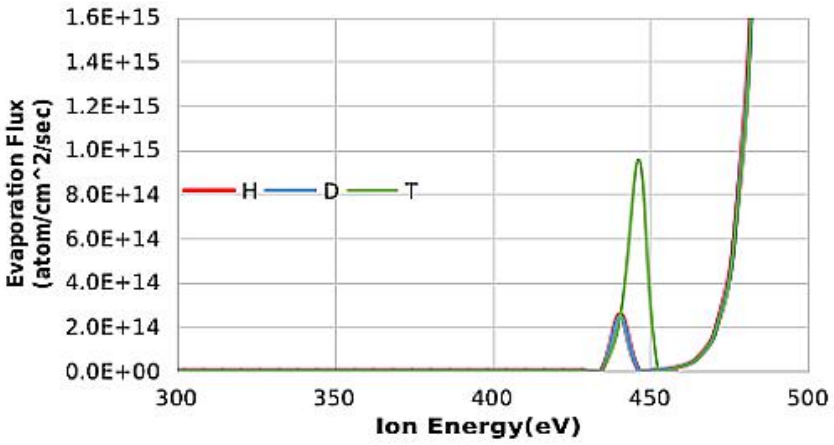

Figure 4.11 Variation of the evaporation flux in the target due to the change in ion energy

The evaporation flux is depicted in Figure 4.11 as a function of the increase in ion energy. As seen in the graph, while the evaporation flux for all ions up to 430 eV is quite low, the flux increases again after a significant peak after this energy. The number of atoms expelled from the target surface is the evaporation flux. As shown in the figure 4.11, no atoms were removed from the surface until the threshold temperature of 430 eV was reached, after which atoms began to be removed from the surface. The abrupt rupture of more than 1014 atoms from the surface, especially after this energy value, indicates that rapid erosion begins in the material after this energy.

4.2 Experimental Setup and LIDAR Images

In figure 4.12 experimental setup images show the Al pellets of Anode cathode surfaces before the He plasma process and during the experiment activity. In a sections of the figure figure 4.13, figure 4.14, figure 4.15, figure 4.16 and figure 4.17 show the He plasma processed specimens of Al anode and Al cathode surface pellets after the experiment. In b sections of the figure 4.13, figure 4.14, figure 4.15, figure 4.16 and figure 4.17, LIDAR images of the He plasma process experiments for different process times; 60, 120, 180, 240 and 300 minutes. LIDAR device measurement is described in the Chapter 3 method experimental setup section.

a) b)

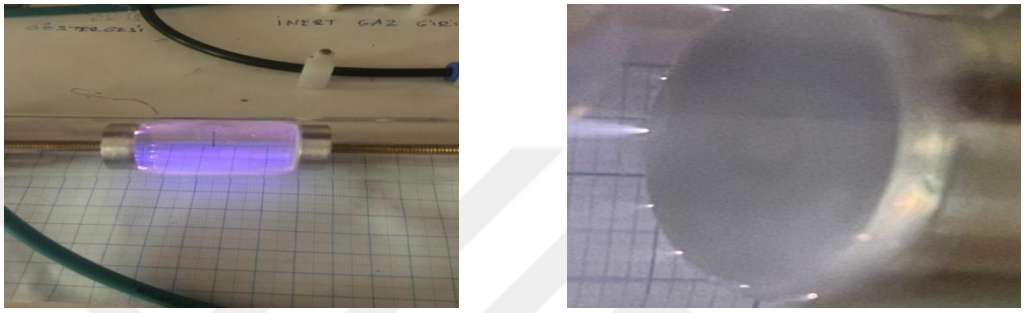

c) d)

Figure 4.12 a)4 cm spaced Al anode and Al cathode pellets in experimental setup **b)**Experimental setup and He plasma state view **c)**He plasma processed on Al anode and Al cathode pellets **d)**Close view of Al anode and Al cathode pellet surfaces

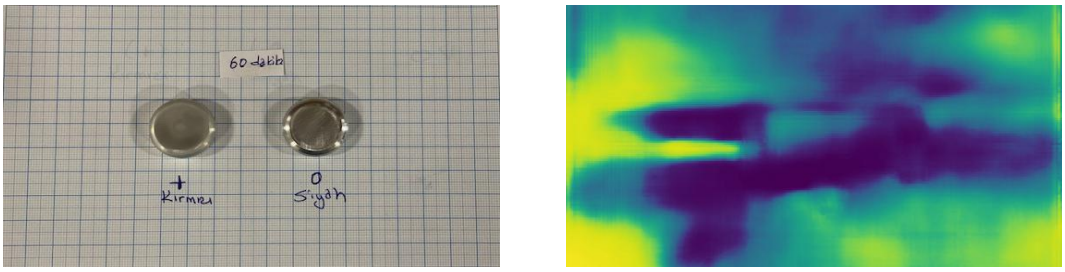

a) b)

Figure 4.13 a) Al anode (+) and Al cathode (-) pellet specimens after 60 min He plasma process **b)**Lidar image of the 60 min He plasma process during the experiment

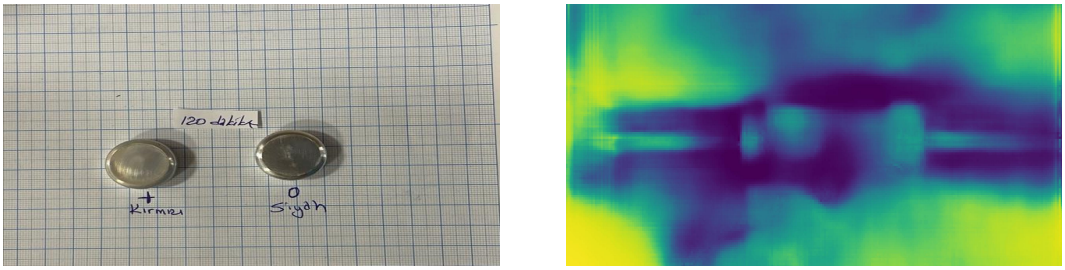

a) b)

Figure 4.14 a) Al anode (+) and Al cathode (-) pellet specimens after 120 min He plasma process
b)Lidar image of the 120 min He plasma process during the experiment

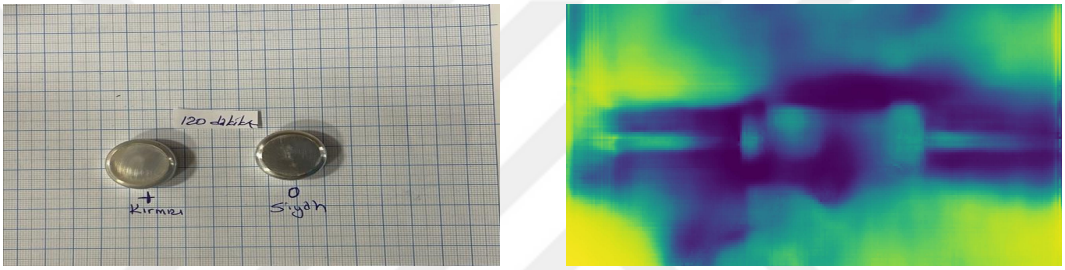

a) b)

Figure 4.15 a) Al anode (+) and Al cathode (-) pellet specimens after 180 min He plasma process
b)Lidar image of the 180 min He plasma process during the experiment

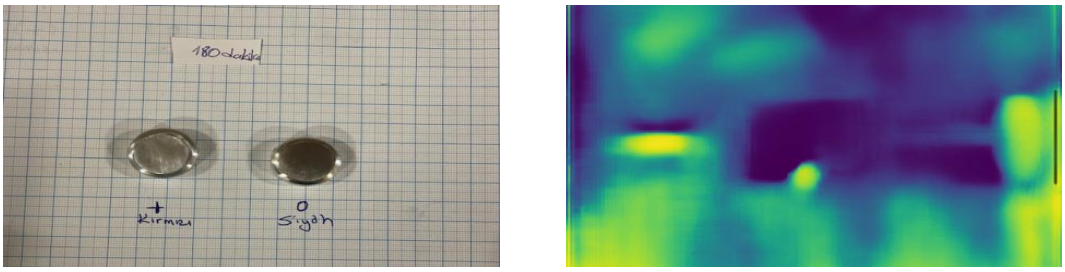

a) b)

Figure 4.16 a) Al anode (+) and Al cathode (-) pellet specimens after 240 min He plasma process
b)Lidar image of the 240 min He plasma process during the experiment

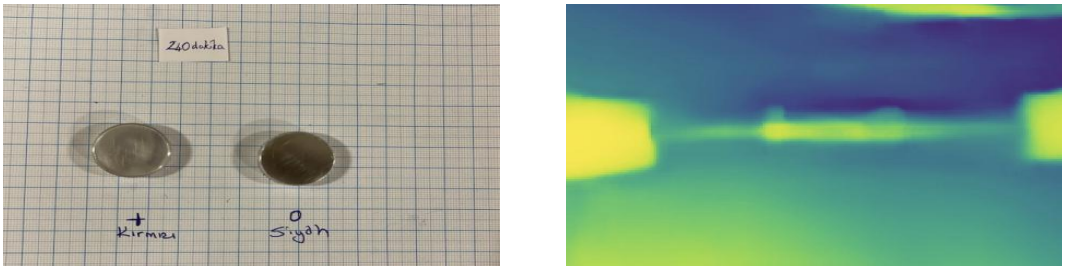

a) b)

Figure 4.17 a) Al anode (+) and Al cathode (-) pellet specimens after 300 min He plasma process **b)**Lidar image of the 300 min He plasma process during the experiment

4.3 Metallographic Observations Results

He plasma processed Al pellets at the anode and cathode for two times at 60, 120, 180 240, 300, and 360 minutes and they are observed under metallographic microscope. Images of the Al anode and cathode surfaces metallographic microscope images and their 3D surface plots graph images with pseudo color depth legends generated under ImageJ software. Experimental setup 1st trial is performed to test if the setup and produce a reliable He plasma with the aluminum pellets. In order to ensure this perspective experimental setup is executed three times on the aluminum pellets in 1 hour, 2 hours and 3 hours 1st trial experimental He plasma processed anode and cathode aluminum pellet. In figures 4.18 to 4.29 aluminum specified selected surface area images under 1 hours of He plasma for 1st trial images are shown with different magnification scales. In figure 4.30, granule formations of Al pellet surface are shown under Metallographic microscope with 500x magnification. Between figure 4.31 to figure 4.38 graphics show aluminum surface observations under 2 hours of He plasma for 1st trials. Aluminum surface observations under 3 hours of He plasma for 1st trial images are shown between figure 4.39 to figure 4.42.

Between figure 4.43 to figure 4.46 unprocessed aluminum pellet surface-control images and their 3d surface image plot graphics is presented as a control data before the experimental study in the 2nd trial. Between figure 4.47 to figure 4.58 graphics show the He plasma processed Al Anode-Al Cathode Surface per 60 minutes as a

start process. Between figure 4.59 to figure 4.68, He plasma processed Al Anode-Al Cathode Surface per 60 minutes images are shown. Between figure 4.69 to figure 4.80 images, He plasma processed Al Anode-Al Cathode Surface per 60 minutes are presented. Between figure 4.81 to figure 4.92, He plasma processed Al Anode-Al Cathode Surface per 240 minutes graphics are shown. In figure 4.93 to figure 4.104 interval, images of He plasma processed Al Anode-Al Cathode Surface per 300 minutes are given. Between figure 4.105 to figure 4.122, graphics of the He plasma processed Al Anode-Al Cathode Surface per 360 minutes are presented. Metallographic microscope and ImageJ software is described in Chapter 3 method section. As in the b sections of figure 4.18 to figure 4.122 interval, images of 3D view is generated to observe the hills and depths on the surface structure of the pellets. In metallographic microscope, black, white and semi grain sections, spots are observed. These sample grains have black and semi-gray spots. Black and gray points are measured face-to-face in fields. These grains on Al pellet surfaces show slopes and holes under the metal microscope.

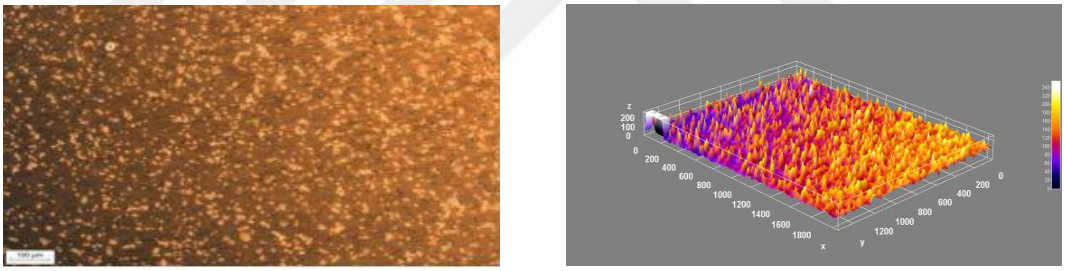

a) b)

Figure 4.18 1 hours of He plasma processed Al pellet selected surface area Metallographic microscope image **a)**50x magnification of the surface **b)**surface 3D graph generated by ImageJ software

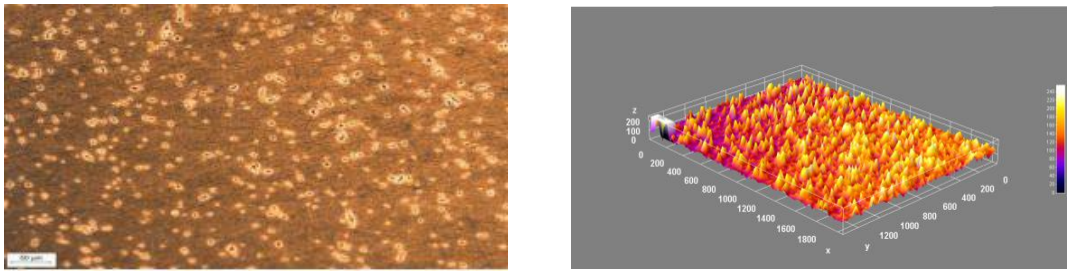

a) b)

Figure 4.19 1 hours of He plasma processed Al pellet selected surface area Metallographic microscope image **a)**100x magnification of the surface **b)**surface 3D graph generated by ImageJ software

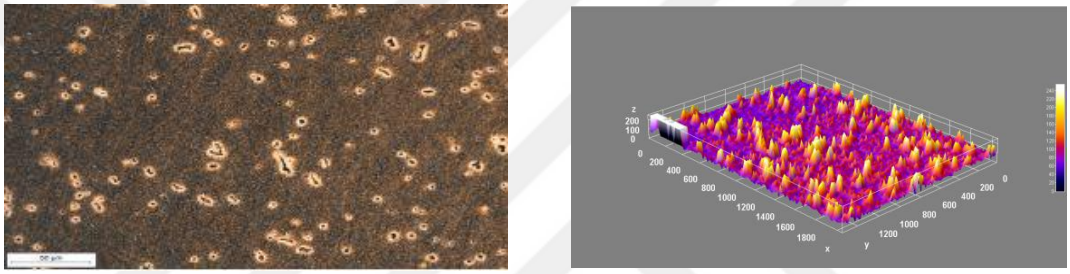

a) b)

Figure 4.20 1 hours of He plasma processed Al pellet selected surface area Metallographic microscope image **a)**200x magnification of the surface **b)**surface 3D graph generated by ImageJ software

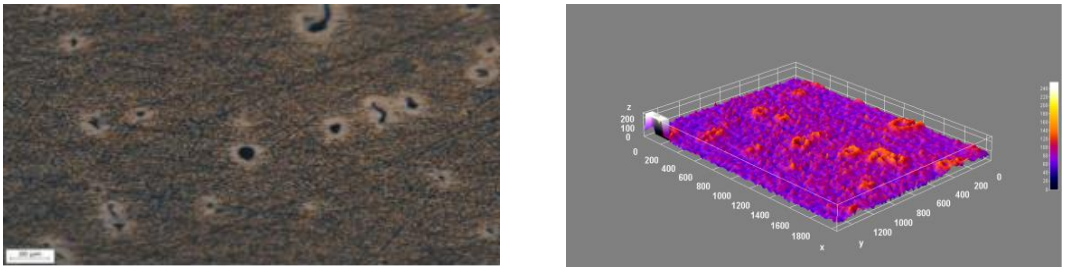

a) b)

Figure 4.21 1 hours of He plasma processed Al pellet selected surface area Metallographic microscope image **a)**500x magnification of the **surface** **b)**surface 3D graph generated by ImageJ software

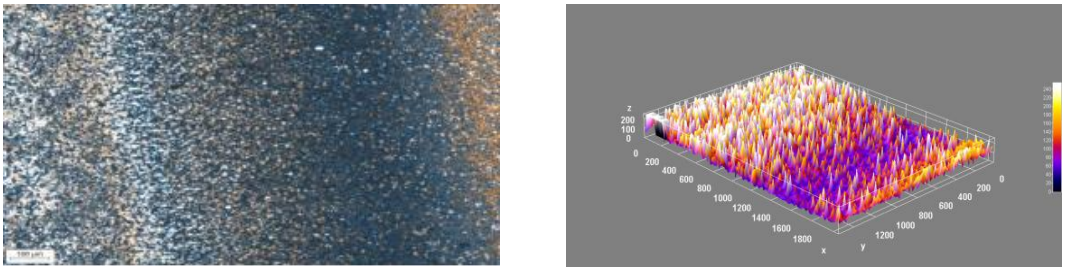

a) b)

Figure 4.22 1 hours of He plasma processed Al pellet selected surface edge area Metallographic microscope image **a)**50x magnification of the surface **b)**surface 3D graph generated by ImageJ software

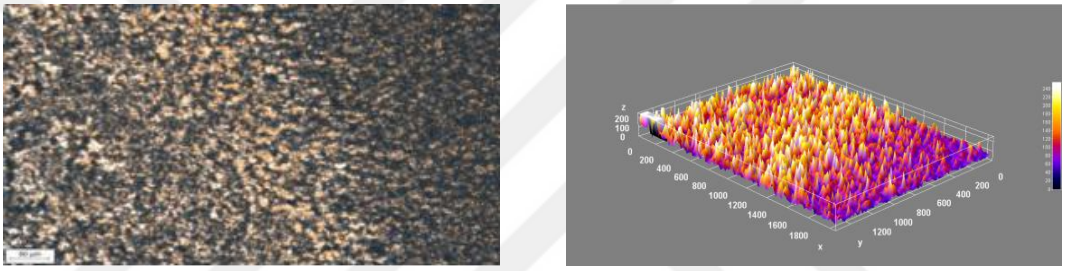

a) b)

Figure 4.23 1 hours of He plasma processed Al pellet selected surface edge area Metallographic microscope image **a)**100x magnification of the surface **b)**surface 3D graph generated by ImageJ software

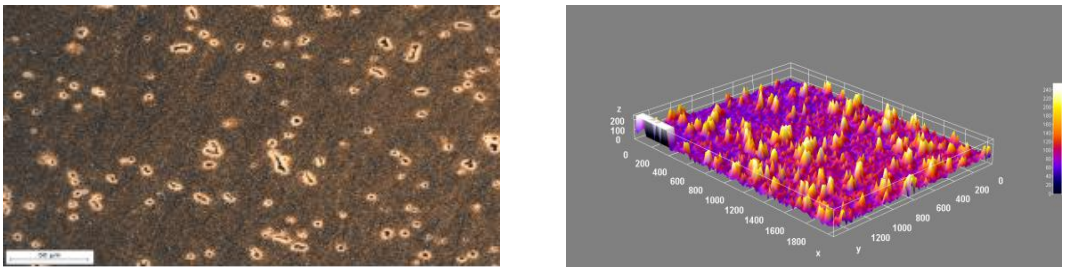

a) b)

Figure 4.24 1 hours of He plasma processed Al pellet selected surface edge area Metallographic microscope image **a)**200x magnification of the surface **b)**surface 3D graph generated by ImageJ software

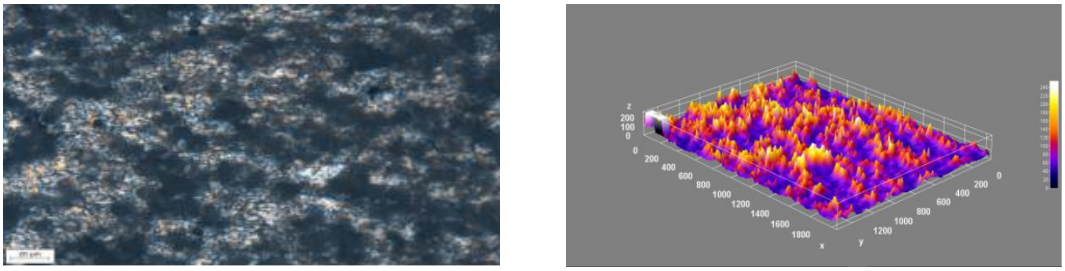

a) b)

Figure 4.25 1 hours of He plasma processed Al pellet selected surface edge area Metallographic microscope image **a)**500x magnification of the surface **b)**surface 3D graph generated by ImageJ software

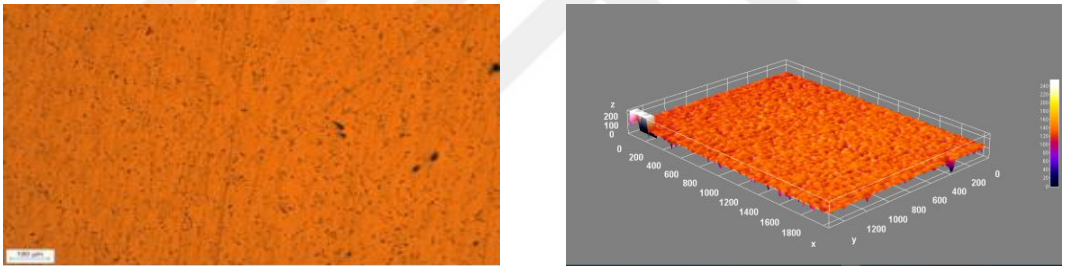

a) b)

Figure 4.26 1 hours of He plasma processed Al pellet selected surface center area Metallographic microscope image **a)**50x magnification of the surface **b)**surface 3D graph generated by ImageJ software

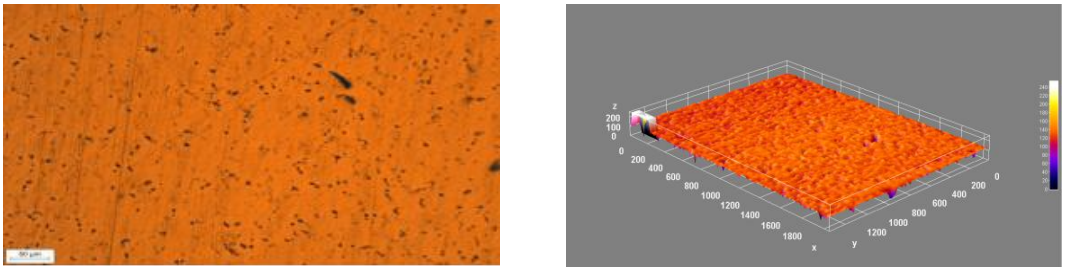

a) b)

Figure 4.27 1 hours of He plasma processed Al pellet selected surface center area Metallographic microscope image **a)**100x magnification of the surface **b)**surface 3D graph generated by ImageJ software

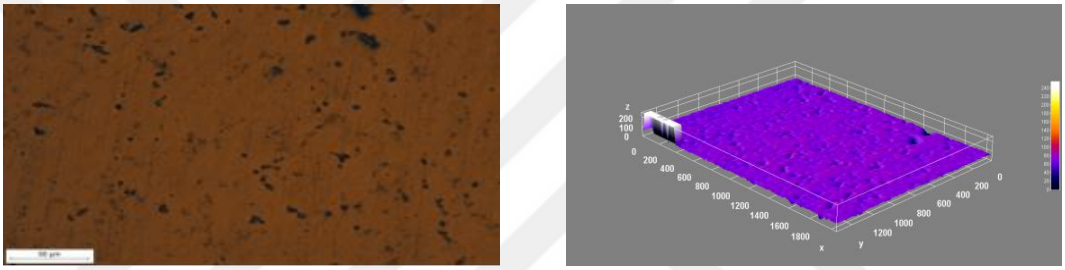

a) b)

Figure 4.28 1 hours of He plasma processed Al pellet selected surface center area Metallographic microscope image **a)**200x magnification of the surface **b)**surface 3D graph generated by ImageJ software

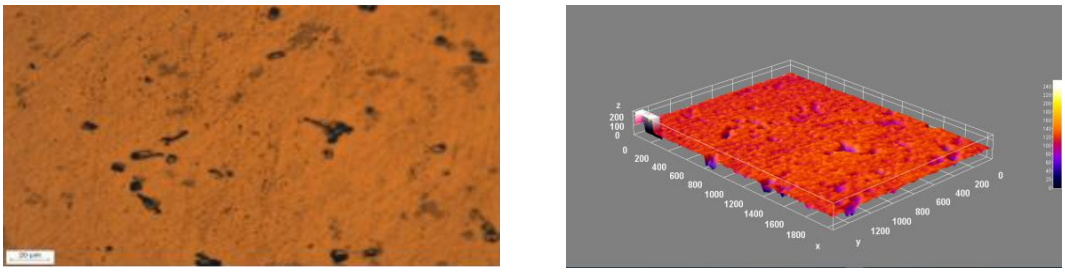

a) b)

Figure 4.29 1 hours of He plasma processed Al pellet selected surface center area Metallographic microscope image **a)**500x magnification of the surface **b)**surface 3D graph generated by ImageJ software

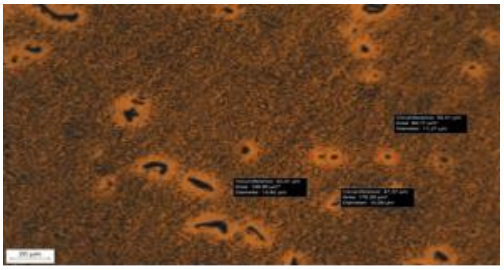

Figure 4.30 Metallographic microscope 500x maginified Al pellet selected surface with granules area image under 1 hours of He plasma process

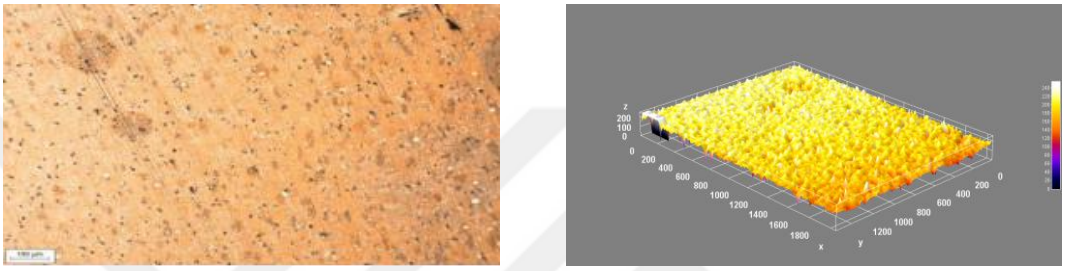

a) b)

Figure 4.31 2 hours of He plasma processed cathode Al pellet selected center surface Metallographic microscope image **a)**50x magnification of the surface **b)**surface 3D graph generated by ImageJ software

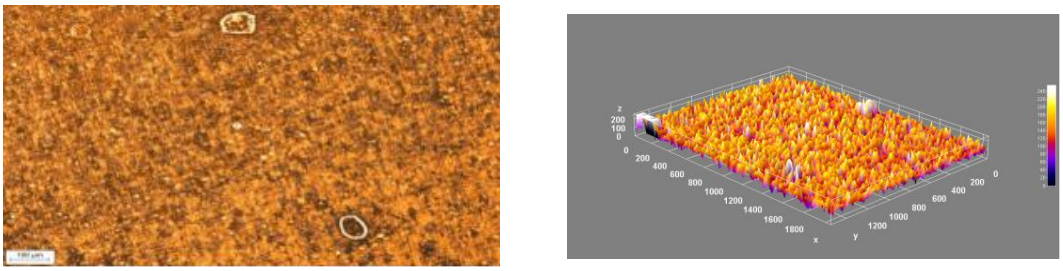

a) b)

Figure 4.32 2 hours of He plasma processed anode Al pellet selected center surface Metallographic microscope image **a)**50x magnification of the surface **b)**surface 3D graph generated by ImageJ software

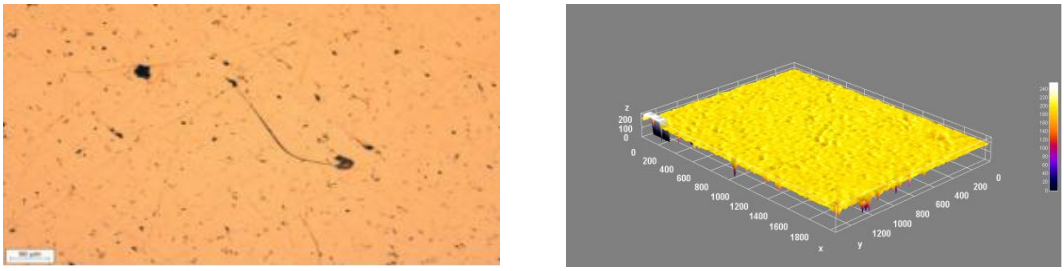

a) b)

Figure 4.33 2 hours of He plasma processed cathode Al pellet selected middle surface area Metallographic microscope image **a)**100x magnification of the surface **b)**surface 3D graph generated by ImageJ software

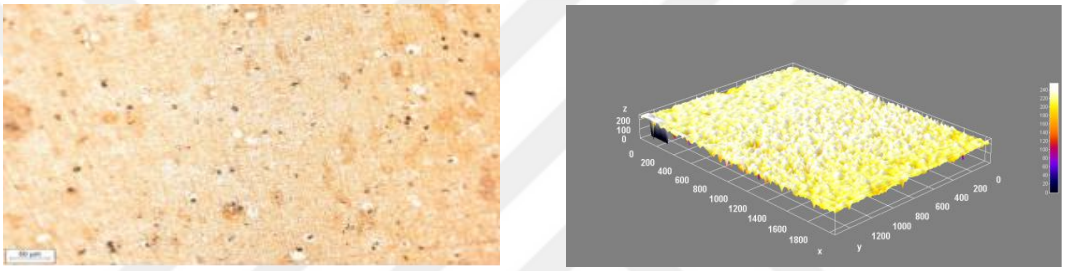

a) b)

Figure 4.34 2 hours of He plasma processed anode Al pellet selected middle surface area Metallographic microscope image **a)**100x magnification of the surface **b)**surface 3D graph generated by ImageJ software

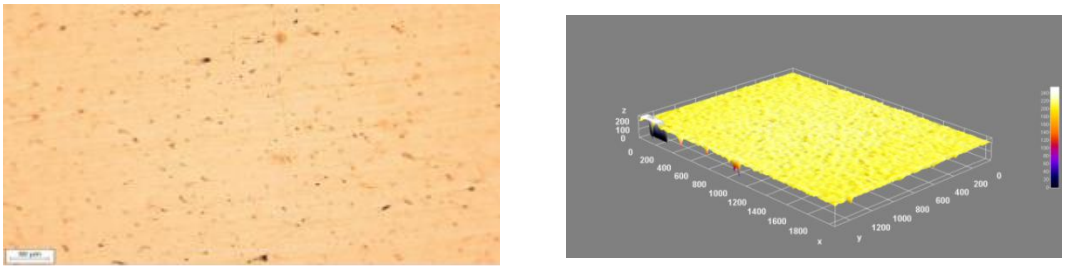

a) b)

Figure 4.35 2 hours of He plasma processed cathode Al pellet selected edge surface area Metallographic microscope image **a)**100x magnification of the surface **b)**surface 3D graph generated by ImageJ software

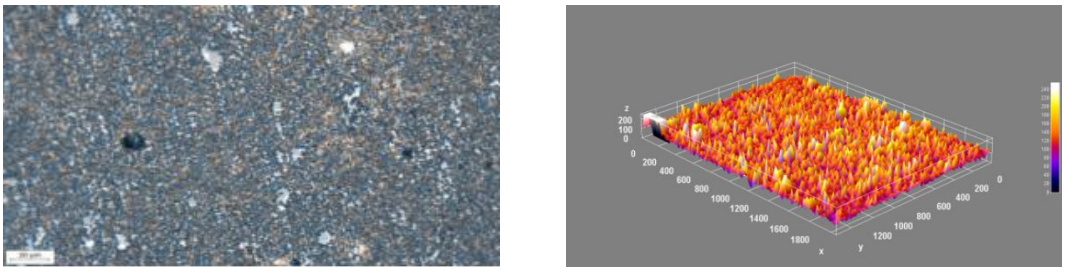

a) b)

Figure 4.36 2 hours of He plasma processed anode Al pellet selected edge surface area Metallographic microscope image **a)**500x magnification of the surface **b)**surface 3D graph generated by ImageJ software

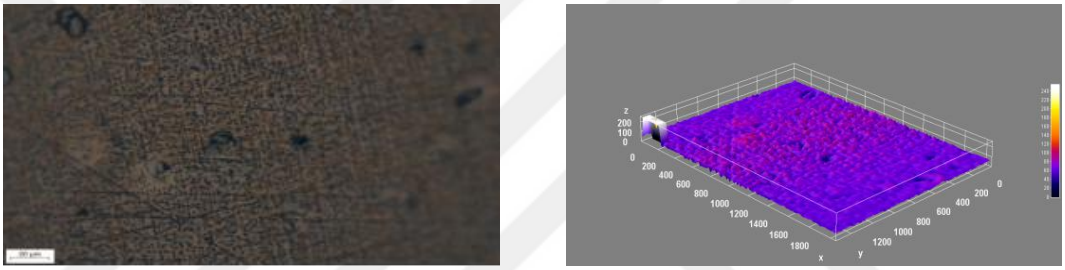

a) b)

Figure 4.37 2 hours of He plasma processed anode Al pellet selected middle surface area Metallographic microscope image **a)**500x magnification of the surface **b)**surface 3D graph generated by ImageJ software

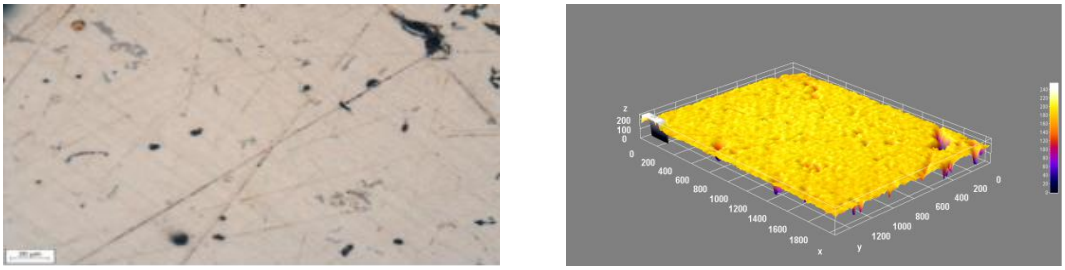

a) b)

Figure 4.38 2 hours of He plasma processed cathode Al pellet selected middle surface area Metallographic microscope image **a)**500x magnification of the surface **b)**surface 3D graph generated by ImageJ software

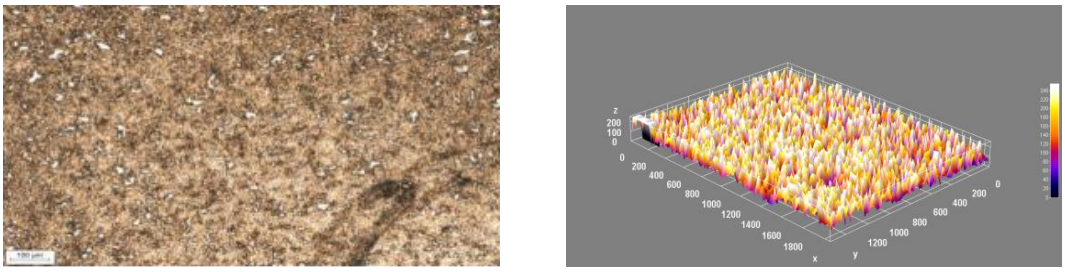

a) b)

Figure 4.39 3 hours of He plasma processed anode Al pellet selected middle surface area Metallographic microscope image **a)**50x magnification of the surface **b)**surface 3D graph generated by ImageJ software

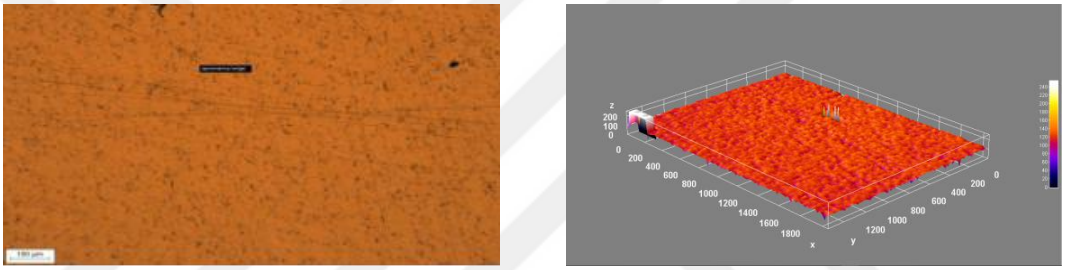

a) b)

Figure 4.40 3 hours of He plasma processed cathode Al pellet selected middle surface area Metallographic microscope image **a)**50x magnification of the surface **b)**surface 3D graph generated by ImageJ software

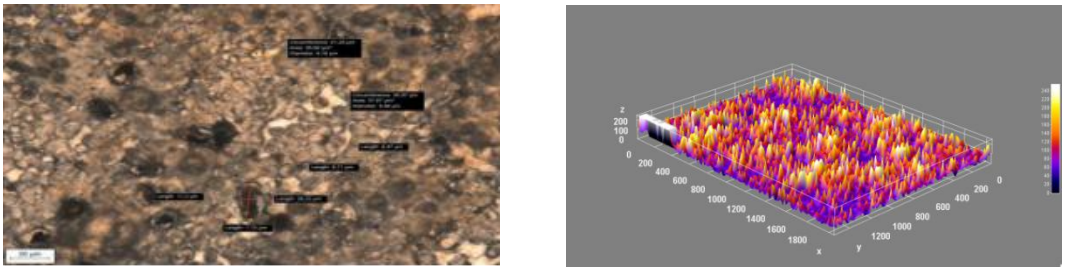

a) b)

Figure 4.41 3 hours of He plasma processed anode Al pellet selected edge surface area Metallographic microscope image **a)**500x magnification of the surface **b**)surface 3D graph generated by ImageJ software

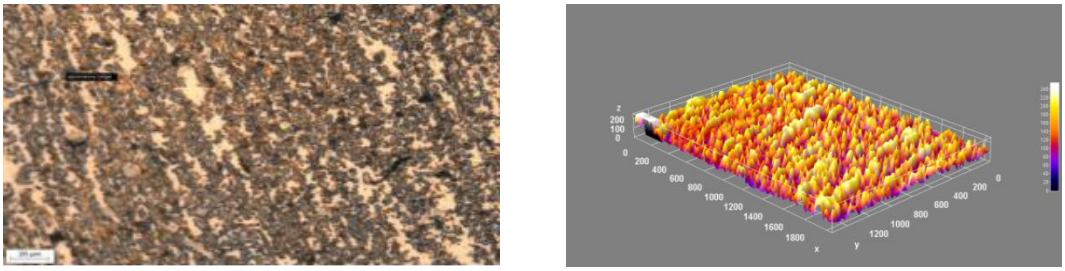

a) b)

Figure 4.42 3 hours of He plasma processed cathode Al pellet selected edge surface area Metallographic microscope image **a)**500x magnification of the surface **b)**surface 3D graph generated by ImageJ software

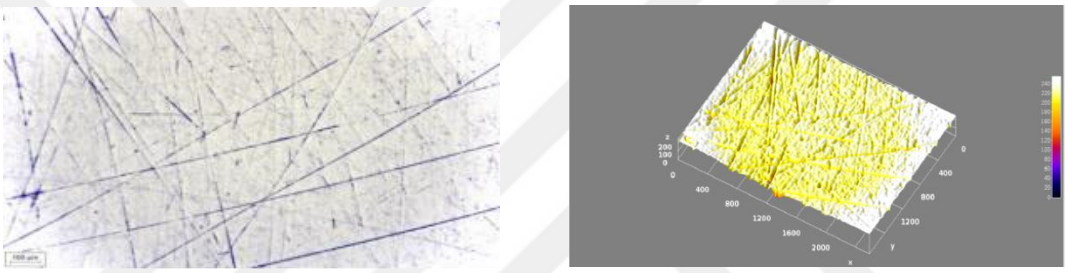

a) b)

Figure 4.43 Unprocessed Al pellet surface under white light selected edge surface area Metallographic microscope image **a)**50x magnification of the surface **b)**surface 3D graph generated by ImageJ software

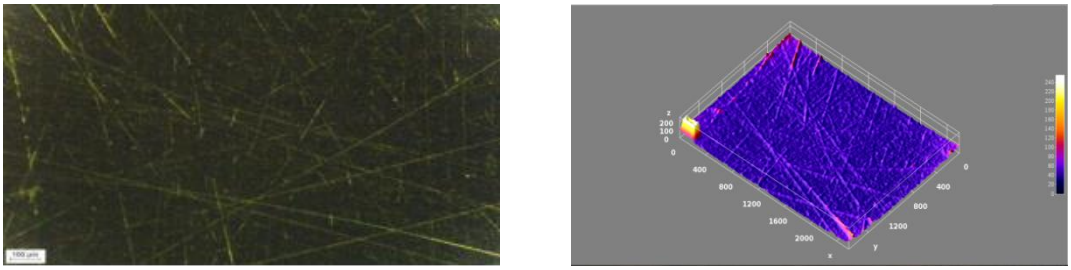

a) b)

Figure 4.44 Unprocessed Al pellet surface under without light selected edge surface area Metallographic microscope **image** **a)**50x magnification of the surface **b)**surface 3D graph generated by ImageJ software

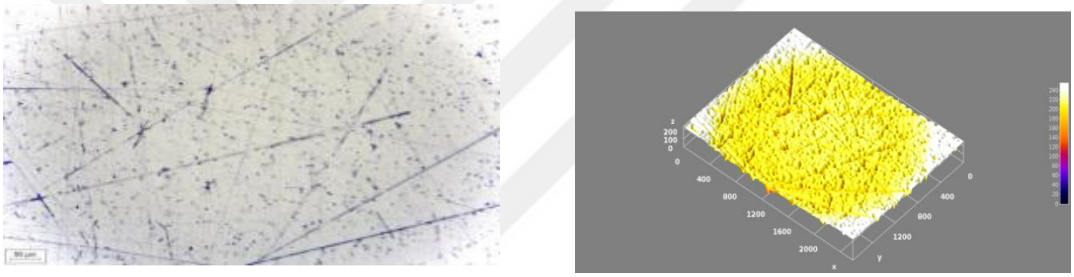

a) b)

Figure 4.45 Unprocessed Al pellet surface under white light selected surface area Metallographic microscope image **a)**100x magnification of the surface **b)**surface 3D graph generated by ImageJ software

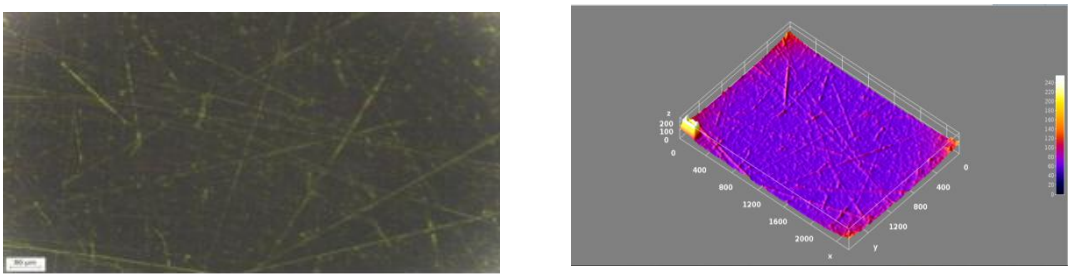

a) b)

Figure 4.46 Unprocessed Al pellet surface under without light selected surface area Metallographic microscope image **a)**100x magnification of the surface **b)**surface 3D graph generated by ImageJ software

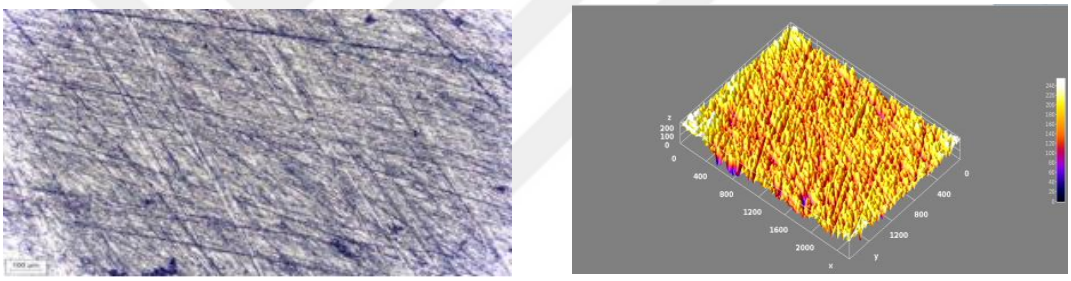

a) b)

Figure 4.47 60 min time He plasma processed aluminum pellet cathode surface under Metallographic microscope's light image **a)**50x magnification of the surface **b)**surface 3D graph generated by ImageJ software

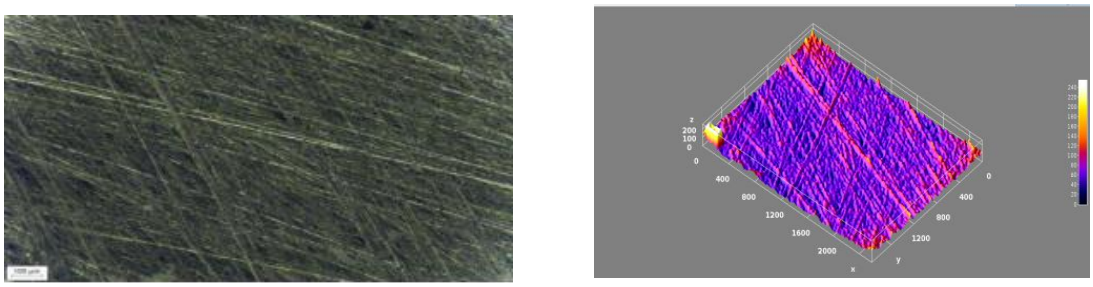

a) b)

Figure 4.48 60 min time He plasma processed aluminum pellet cathode surface without Metallographic microscope's light image **a)**50x magnification of the surface **b)**surface 3D graph generated by ImageJ software

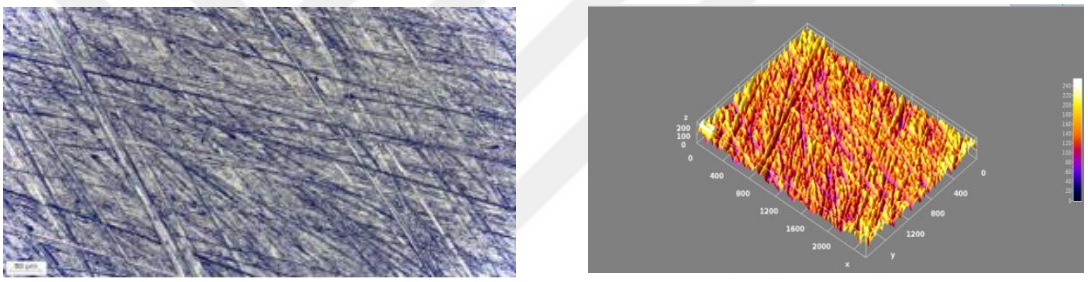

a) b)

Figure 4.49 60 min time He plasma processed aluminum pellet cathode surface under Metallographic microscope's light image **a)**100x magnification of the surface **b)**surface 3D graph generated by ImageJ software

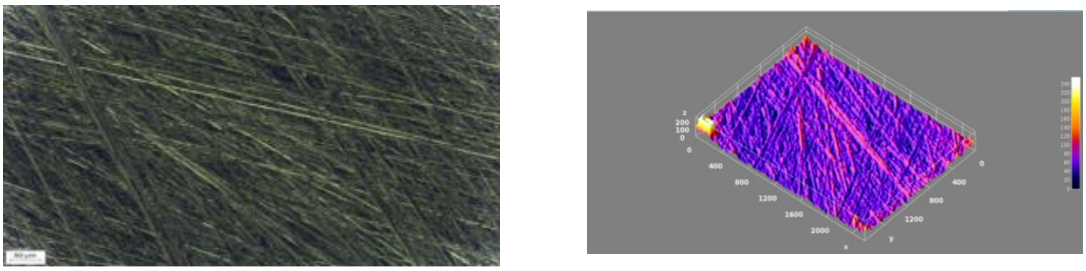

a) b)

Figure 4.50 60 min time He plasma processed aluminum pellet cathode surface without Metallographic microscope's light image **a)**100x magnification of the surface **b**)surface 3D graph generated by ImageJ software

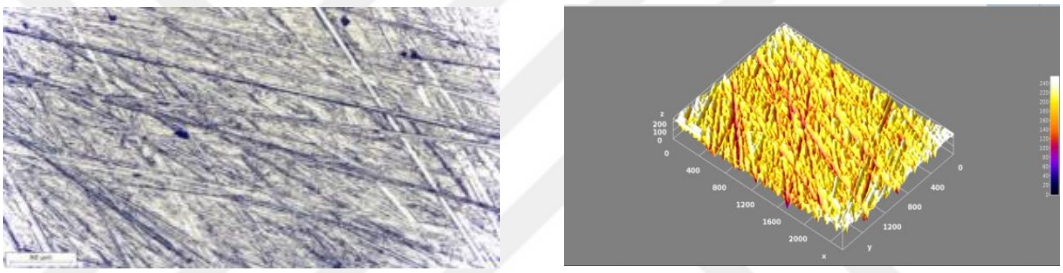

a) b)

Figure 4.51 60 min time He plasma processed aluminum pellet cathode surface under Metallographic microscope's light image **a)**200x magnification of the surface **b)**surface 3D graph generated by ImageJ software

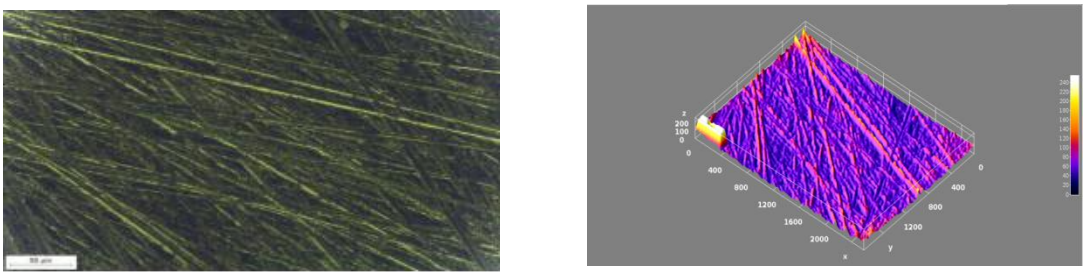

a) b)

Figure 4.52 60 min time He plasma processed aluminum pellet cathode surface without Metallographic microscope's light image **a)**200x magnification of the surface **b)**surface 3D graph generated by ImageJ software

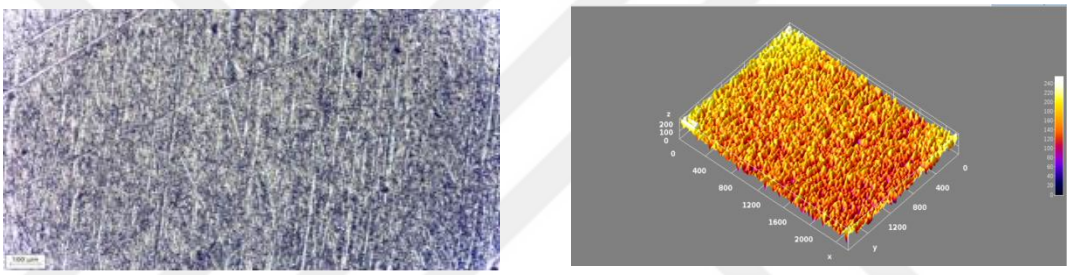

a) b)

Figure 4.53 60 min time He plasma processed aluminum pellet anode surface under Metallographic microscope's light image **a)**50x magnification of the surface **b)**surface 3D graph generated by ImageJ software

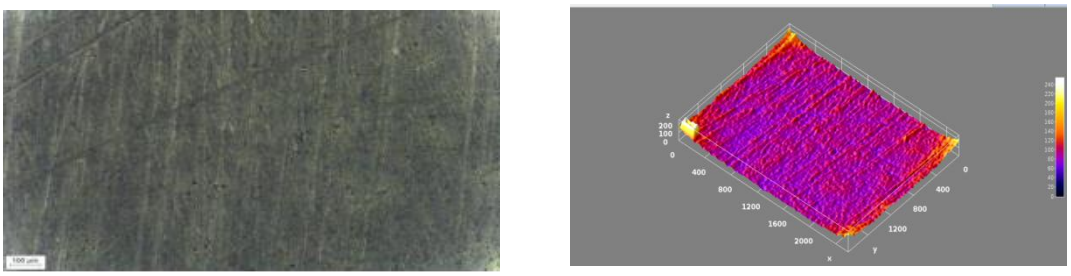

a) b)

Figure 4.54 60 min time He plasma processed aluminum pellet anode surface without Metallographic microscope's light image **a)**50x magnification of the surface **b)**surface 3D graph generated by ImageJ software

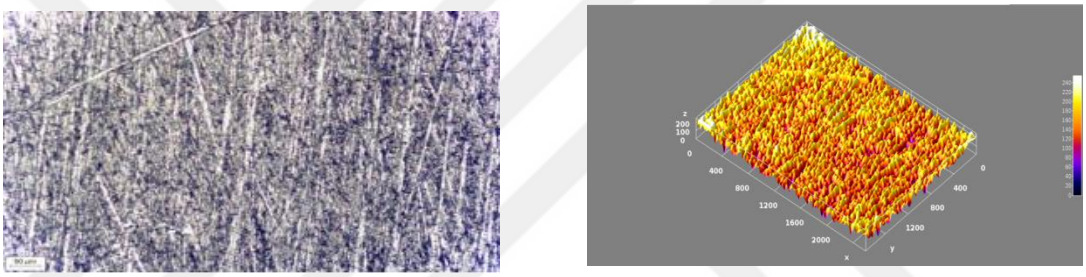

a) b)

Figure 4.55 60 min time He plasma processed aluminum pellet anode surface under Metallographic microscope's light image **a)**100x magnification of the surface **b)**surface 3D graph generated by ImageJ software

a) b)

Figure 4.56 60 min time He plasma processed aluminum pellet anode surface without Metallographic microscope's light image **a)**100x magnification of the surface **b)**surface 3D graph generated by ImageJ software

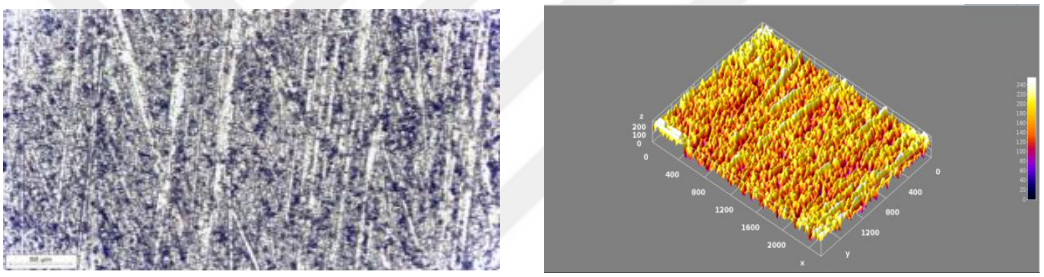

a) b)

Figure 4.57 60 min time He plasma processed aluminum pellet anode surface under light Metallographic microscope's light **image a)**200x magnification of the surface **b)**surface 3D graph generated by ImageJ software

a) b)

Figure 4.58 60 min time He plasma processed aluminum pellet anode surface without Metallographic microscope's light image **a)**200x magnification of the surface **b)**surface 3D graph generated by ImageJ software

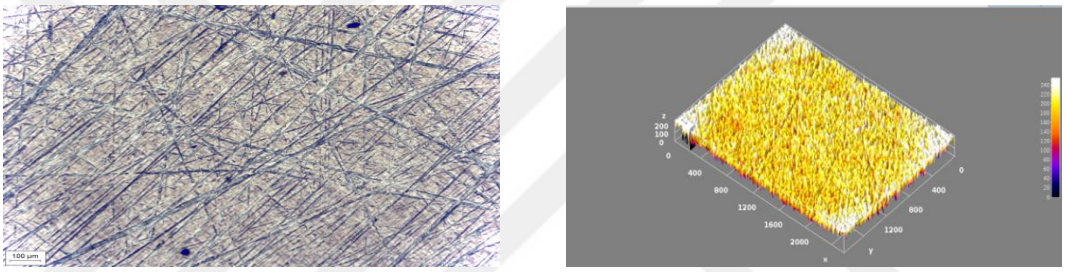

a) b)

Figure 4.59 120 min time He plasma processed aluminum pellet cathode surface under Metallographic microscope's light image **a)**50x magnification of the surface **b)**surface 3D graph generated by ImageJ software

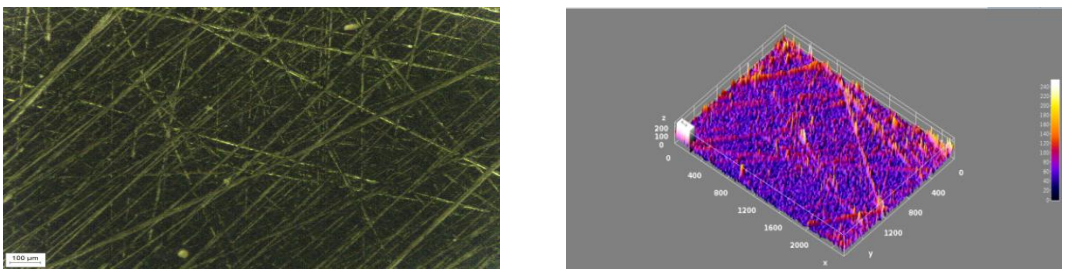

a) b)

Figure 4.60 120 min time He plasma processed aluminum pellet cathode surface without Metallographic microscope's light image **a)**50x magnification of the surface **b)**surface 3D graph generated by ImageJ software

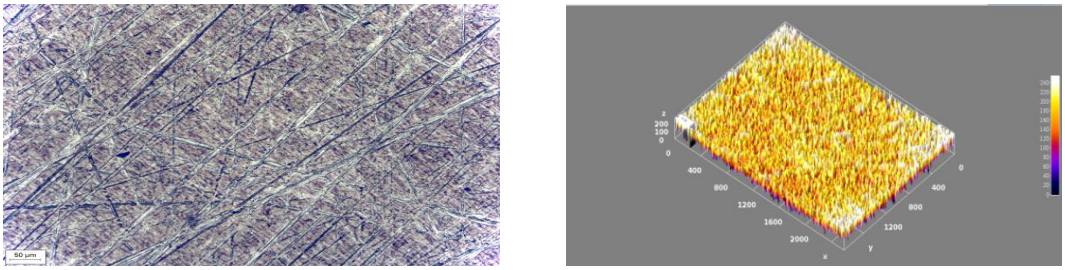

a) b)

Figure 4.61 120 min time He plasma processed aluminum pellet cathode surface under Metallographic microscope's light image **a)**100x magnification of the surface **b)**surface 3D graph generated by ImageJ software

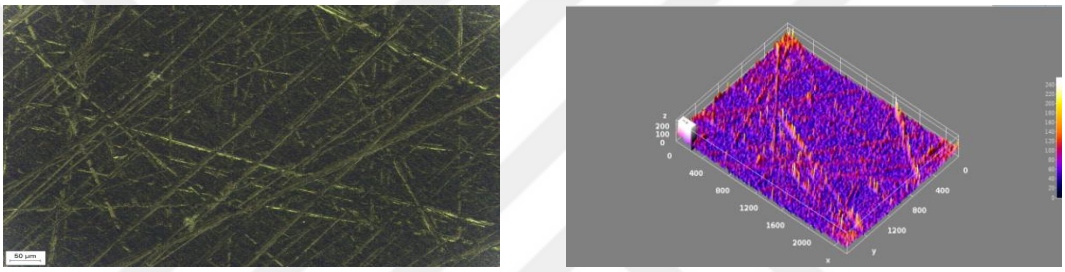

a) b)

Figure 4.62 120 min time He plasma processed aluminum pellet cathode surface without Metallographic microscope's light image **a)**100x magnification of the surface **b)**surface 3D graph generated by ImageJ software

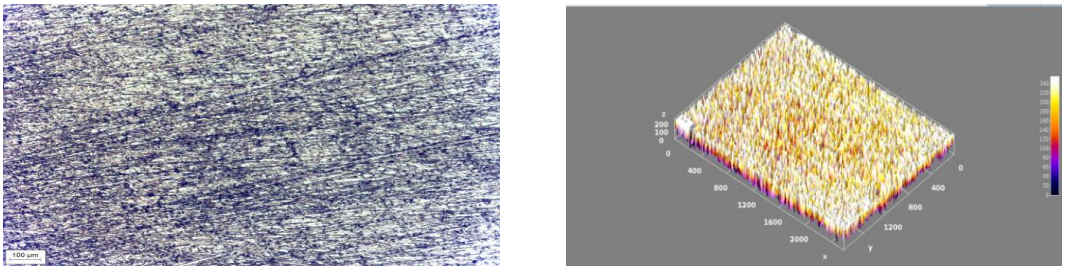

a) b)

Figure 4.63 120 min time He plasma processed aluminum pellet anode surface under Metallographic microscope's light image **a)**50x magnification of the surface **b)**surface 3D graph generated by ImageJ software

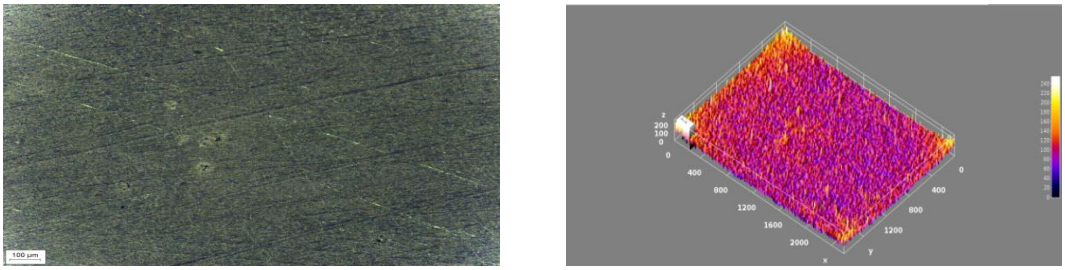

a) b)

Figure 4.64 120 min time He plasma processed aluminum pellet anode surface without Metallographic microscope's light image **a)**50x magnification of the surface **b)**surface 3D graph generated by ImageJ software

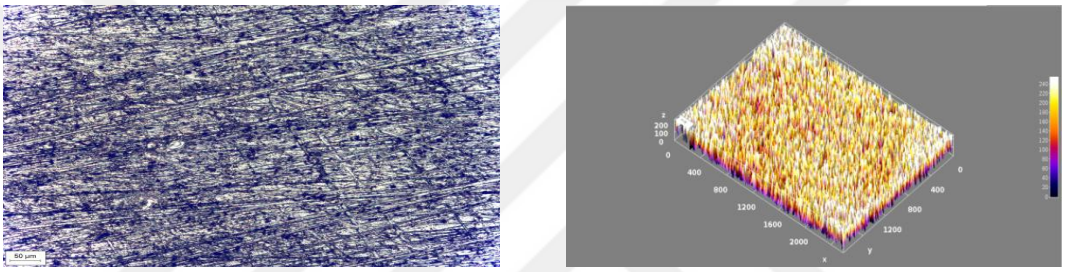

a) b)

Figure 4.65 120 min time He plasma processed aluminum pellet anode surface under Metallographic microscope's light image **a)**100x magnification of the surface **b**)surface 3D graph generated by ImageJ software

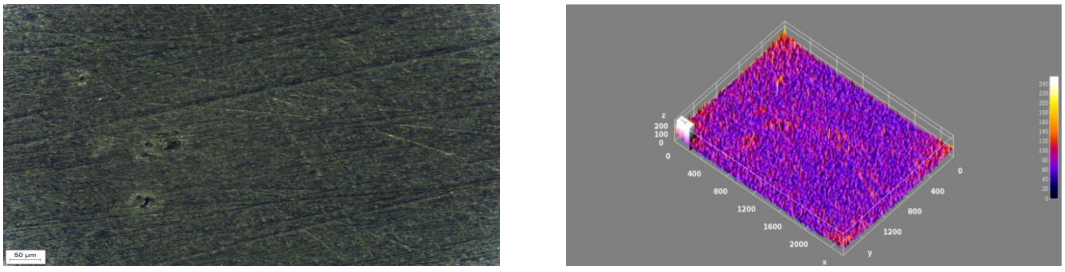

a) b)

Figure 4.66 120 min time He plasma processed aluminum pellet anode surface without Metallographic microscope's light image **a)**100x magnification of the surface **b)**surface 3D graph generated by ImageJ software

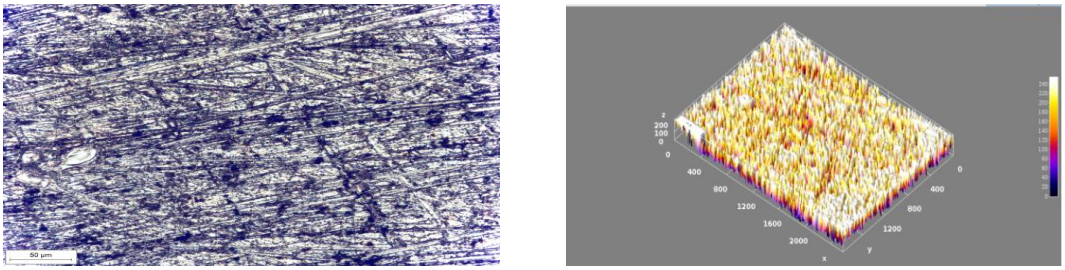

a) b)

Figure 4.67 120 min time He plasma processed aluminum pellet anode surface under Metallographic microscope's light image **a)**200x magnification of the surface **b)**surface 3D graph generated by ImageJ software

a) b)

Figure 4.68 120 min time He plasma processed aluminum pellet anode surface without Metallographic microscope's light image **a)**200x magnification of the surface **b)**surface 3D graph generated by ImageJ software

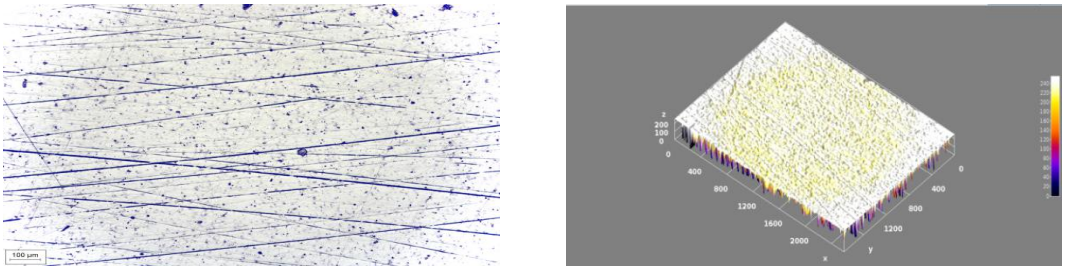

a) b)

Figure 4.69 180 min time He plasma processed aluminum pellet cathode surface under Metallographic microscope's light image **a)**50x magnification of the surface **b)**surface 3D graph generated by ImageJ software

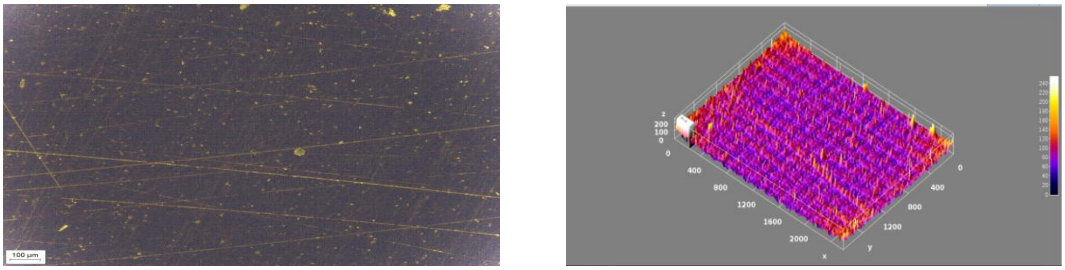

a) b)

Figure 4.70 180 min time He plasma processed aluminum pellet cathode surface without Metallographic microscope's light image **a)**50x magnification of the surface **b)**surface 3D graph generated by ImageJ software

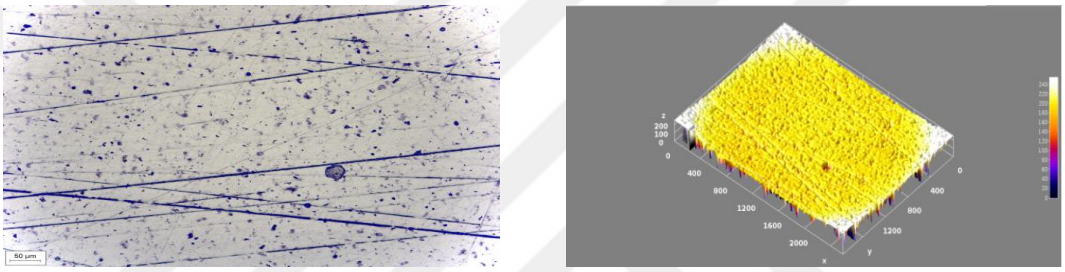

a) b)

Figure 4.71 180 min time He plasma processed aluminum pellet cathode surface under Metallographic microscope's light image **a)**100x magnification of the surface **b)**surface 3D graph generated by ImageJ software

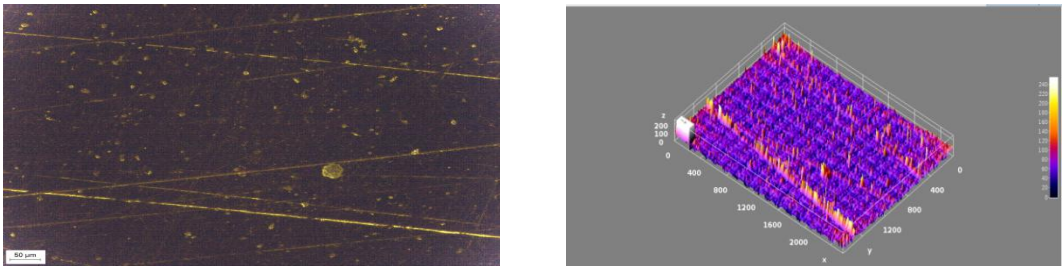

a) b)

Figure 4.72 180 min time He plasma processed aluminum pellet cathode surface without Metallographic microscope's light image **a)**100x magnification of the surface **b**)surface 3D graph generated by ImageJ software

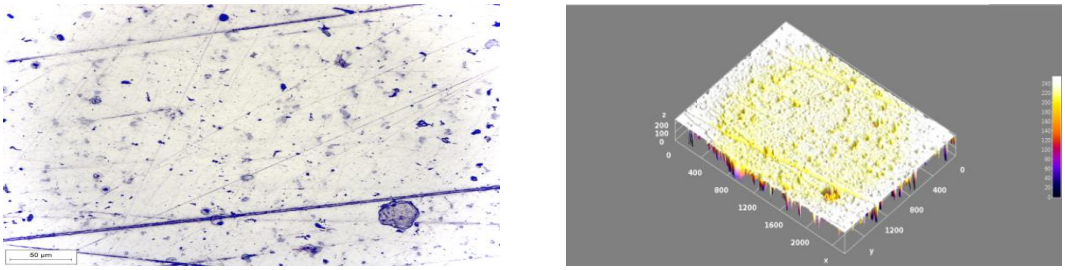

a) b)

Figure 4.73 180 min time He plasma processed aluminum pellet cathode surface under Metallographic microscope's light image **a)**200x magnification of the surface **b)**surface 3D graph generated by ImageJ software

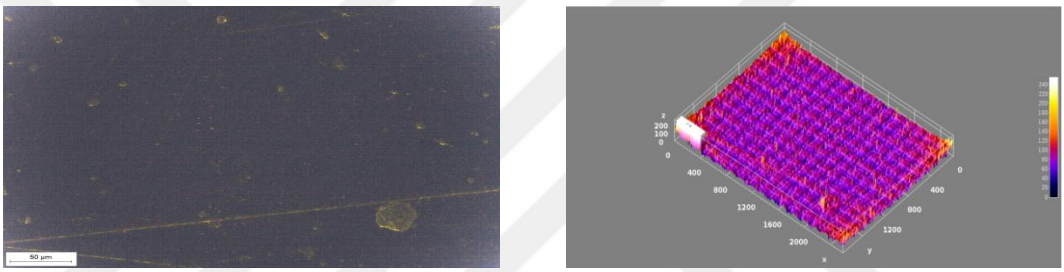

a) b)

Figure 4.74 180 min time He plasma processed aluminum pellet cathode surface without Metallographic microscope's light image **a)**200x magnification of the surface **b)**surface 3D graph generated by ImageJ software

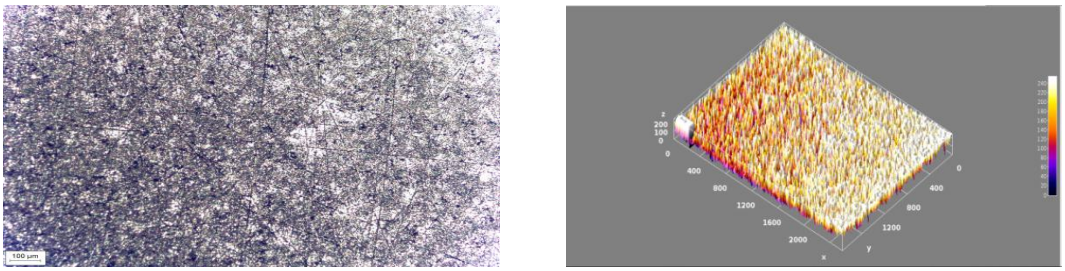

a) b)

Figure 4.75 180 min time He plasma processed aluminum pellet anode surface under Metallographic microscope's light image **a)**50x magnification of the **surface** **b)**surface 3D graph generated by ImageJ software

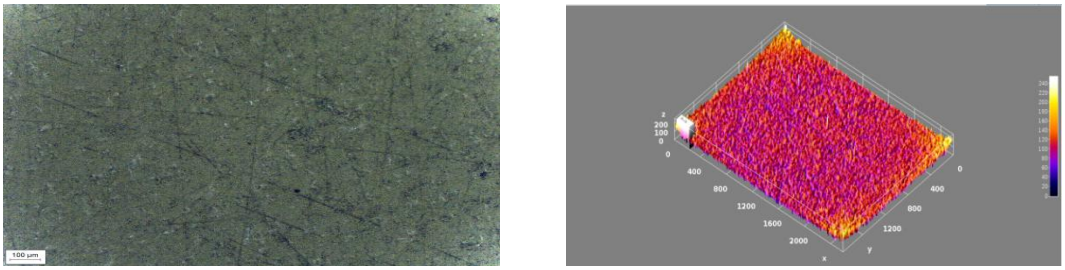

a) b)

Figure 4.76 180 min time He plasma processed aluminum pellet anode surface without Metallographic microscope's light image **a)**50x magnification of the surface **b)**surface 3D graph generated by ImageJ software

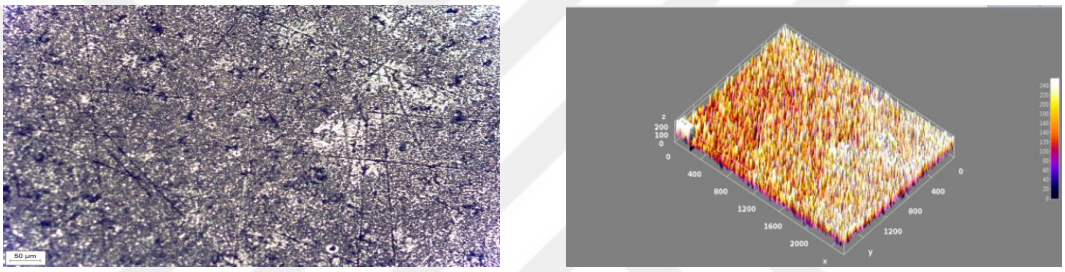

a) b)

Figure 4.77 180 min time He plasma processed aluminum pellet anode surface under Metallographic microscope's light image **a)**100x magnification of the surface **b)**surface 3D graph generated by ImageJ software

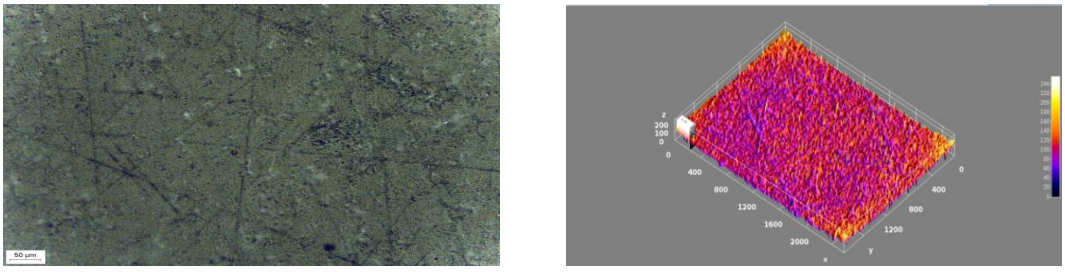

a) b)

Figure 4.78 180 min time He plasma processed aluminum pellet anode surface without Metallographic microscope's light image **a)**100x magnification of the surface **b)**surface 3D graph generated by ImageJ software

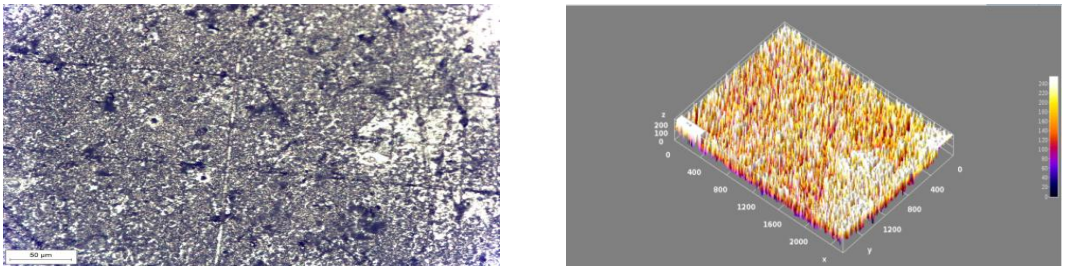

a) b)

Figure 4.79 180 min time He plasma processed aluminum pellet anode surface under Metallographic microscope's light image a)200x magnification of the surface **b)**surface 3D graph generated by ImageJ software

a) b)

Figure 4.80 180 min time He plasma processed aluminum pellet anode surface without Metallographic microscope's light image **a)**200x magnification of the surface **b)**surface 3D graph generated by ImageJ software

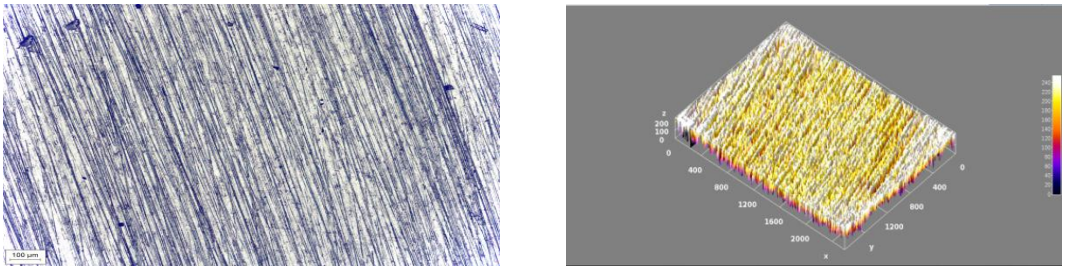

a) b)

Figure 4.81 240 min time He plasma processed aluminum pellet cathode surface under Metallographic microscope's light image **a)**50x magnification of the surface **b)**surface 3D graph generated by ImageJ software

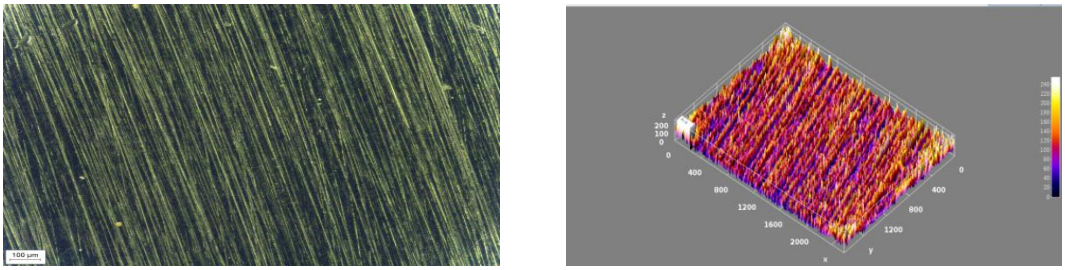

a) b)

Figure 4.82 240 min time He plasma processed aluminum pellet cathode surface without Metallographic microscope's light image **a)**50x magnification of the surface **b)**surface 3D graph generated by ImageJ software

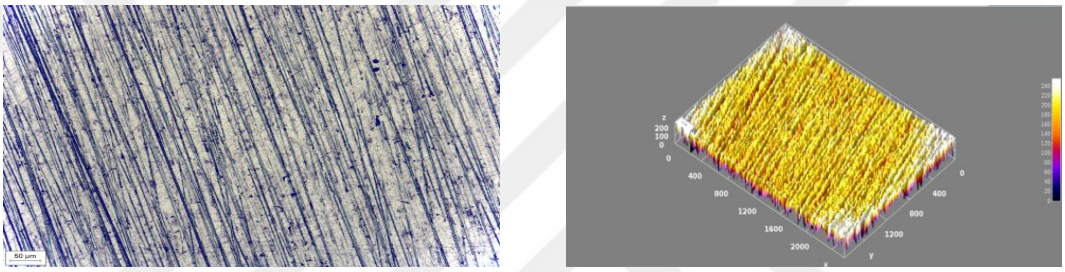

a) b)

Figure 4.83 240 min time He plasma processed aluminum pellet cathode surface under Metallographic microscope's light image **a)**100x magnification of the surface **b)**surface 3D graph generated by ImageJ software

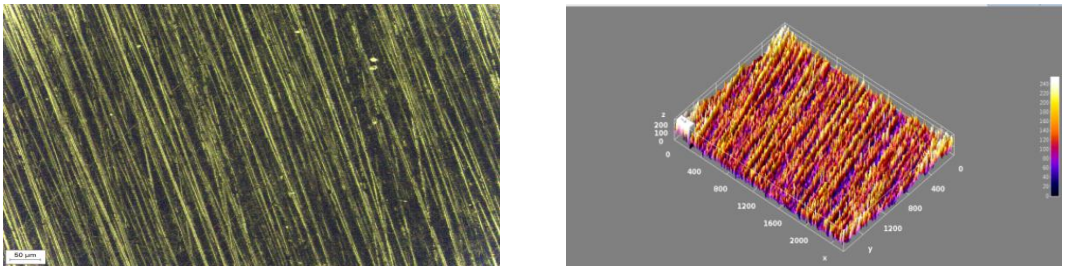

a) b)

Figure 4.84 240 min time He plasma processed aluminum pellet cathode surface without Metallographic microscope's light image **a)**100x magnification of the surface **b)**surface 3D graph generated by ImageJ software

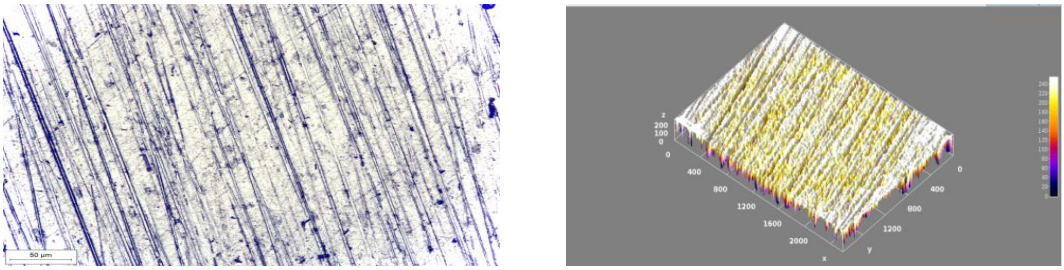

a) b)

Figure 4.85 240 min time He plasma processed aluminum pellet cathode surface under Metallographic microscope's light image **a)**200x magnification of the surface **b)**surface 3D graph generated by ImageJ software

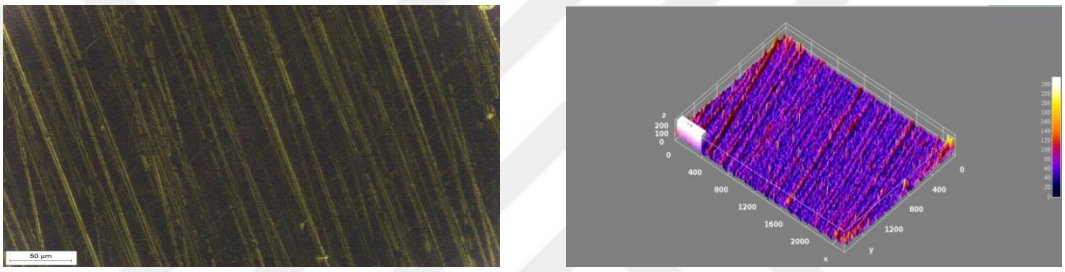

a) b)

Figure 4.86 240 min time He plasma processed aluminum pellet cathode surface without Metallographic microscope's light image **a)**200x magnification of the surface **b)**surface 3D graph generated by ImageJ software

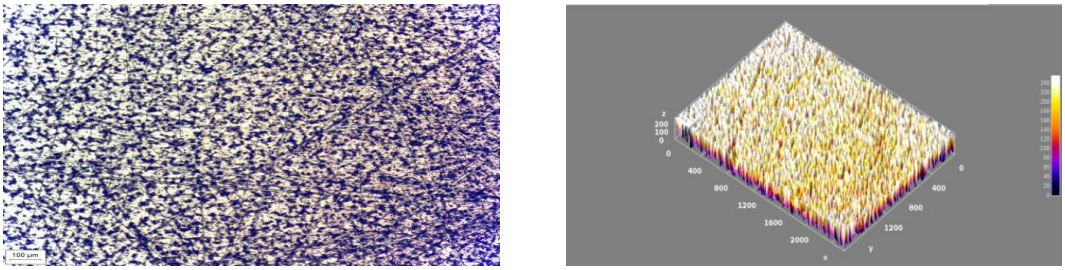

a) b)

Figure 4.87 240 min time He plasma processed aluminum pellet anode surface under Metallographic microscope's light image **a)**50x magnification of the surface **b)**surface 3D graph generated by ImageJ software

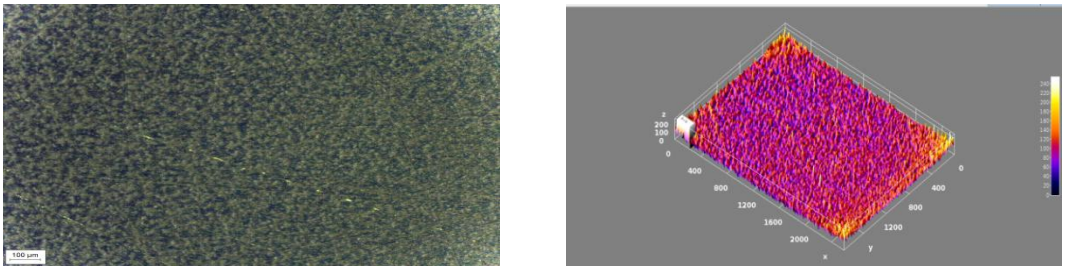

a) b)

Figure 4.88 240 min time He plasma processed aluminum pellet anode surface without Metallographic microscope's light image **a)**50x magnification of the surface **b)**surface 3D graph generated by ImageJ software

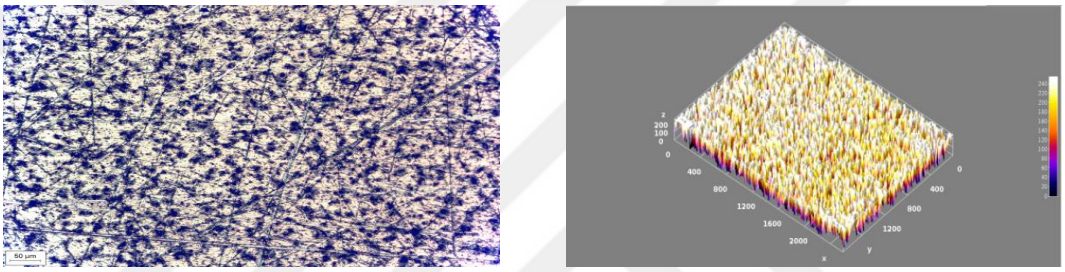

a) b)

Figure 4.89 240 min time He plasma processed aluminum pellet anode surface under Metallographic microscope's light image **a)**100x magnification of the surface **b)**surface 3D graph generated by ImageJ software

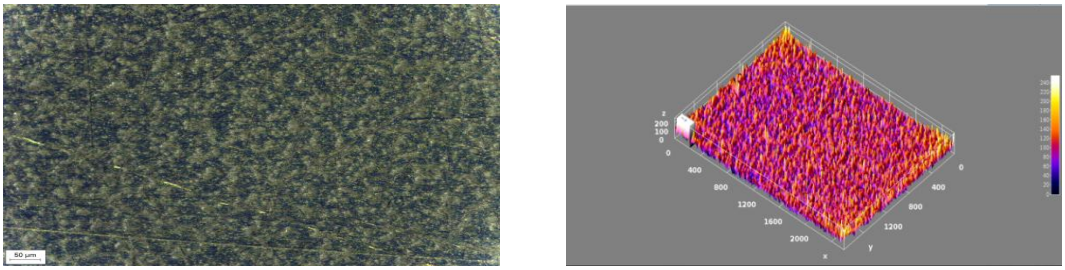

a) b)

Figure 4.90 240 min time He plasma processed aluminum pellet anode surface without Metallographic microscope's light image **a)**100x magnification of the surface **b)**surface 3D graph generated by ImageJ software

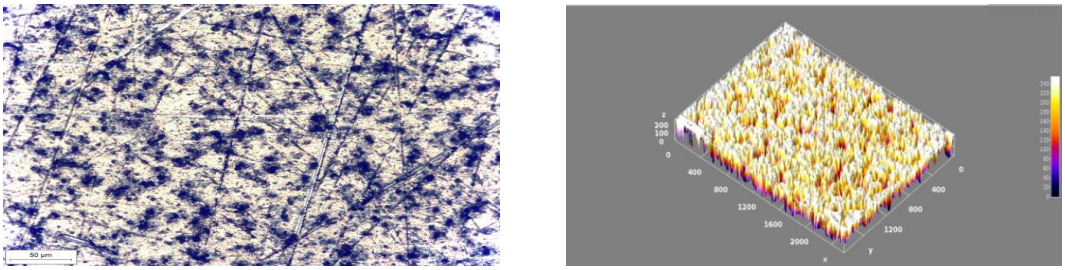

a) b)

Figure 4.91 240 min time He plasma processed aluminum pellet anode surface under Metallographic microscope's light image **a)**200x magnification of the surface **b)**surface 3D graph generated by ImageJ software

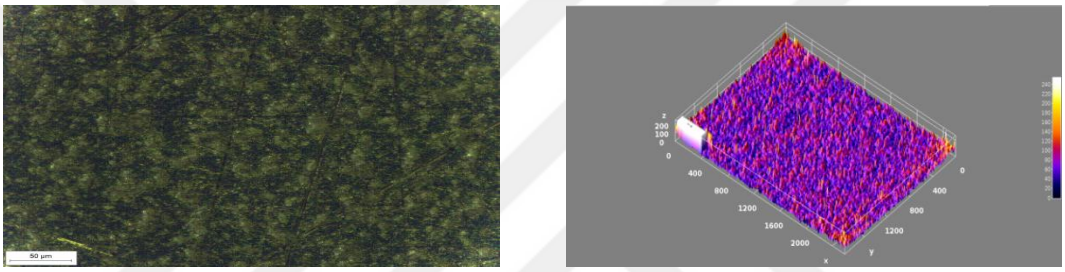

a) b)

Figure 4.92 240 min time He plasma processed aluminum pellet anode surface without Metallographic microscope's light image **a)**200x magnification of the surface **b)**surface 3D graph generated by ImageJ software

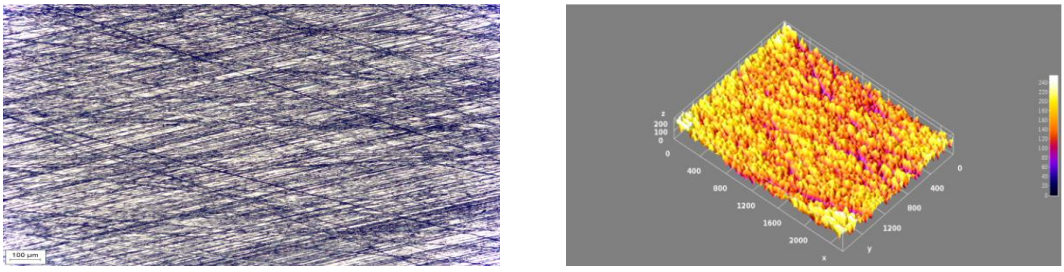

a) b)

Figure 4.93 300 min time He plasma processed aluminum pellet cathode surface under Metallographic microscope's light image **a)**50x magnification of the surface **b)**surface 3D graph generated by ImageJ software

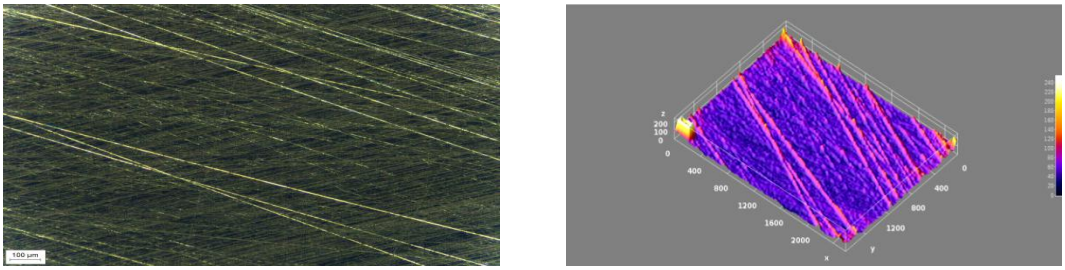

a) b)

Figure 4.94 300 min time He plasma processed aluminum pellet cathode surface without Metallographic microscope's light image **a)**50x magnification of the surface **b)**surface 3D graph generated by ImageJ software

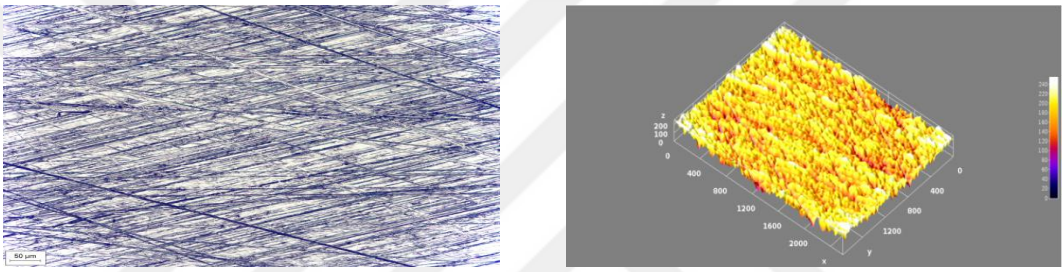

a) b)

Figure 4.95 300 min time He plasma processed aluminum pellet cathode surface under Metallographic microscope's light image **a)**100x magnification of the surface **b)**surface 3D graph generated by ImageJ software

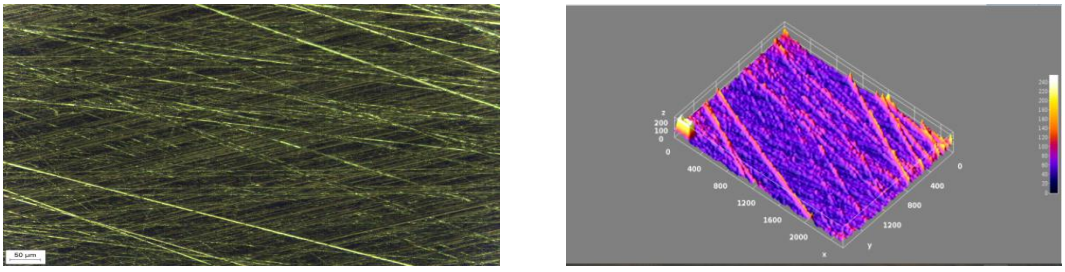

a) b)

Figure 4.96 300 min time He plasma processed aluminum pellet cathode surface without Metallographic microscope's light image **a)**100x magnification of the surface **b)**surface 3D graph generated by ImageJ software

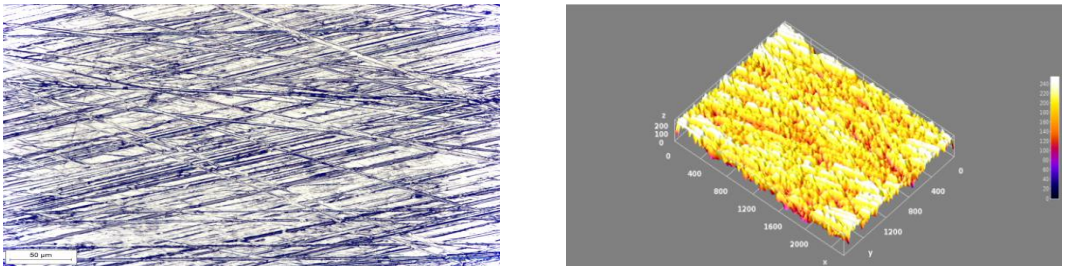

a) b)

Figure 4.97 300 min time He plasma processed aluminum pellet cathode surface under Metallographic microscope's light image **a)**200x magnification of the surface **b)**surface 3D graph generated by ImageJ software

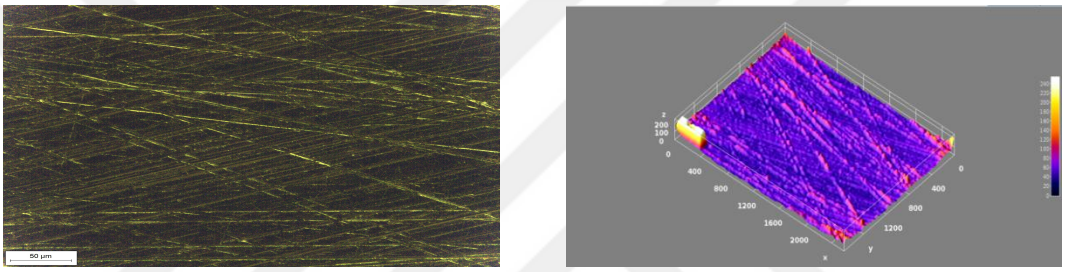

a) b)

Figure 4.98 300 min time He plasma processed aluminum pellet cathode surface without Metallographic microscope's light image **a)**200x magnification of the surface **b)**surface 3D graph generated by ImageJ software

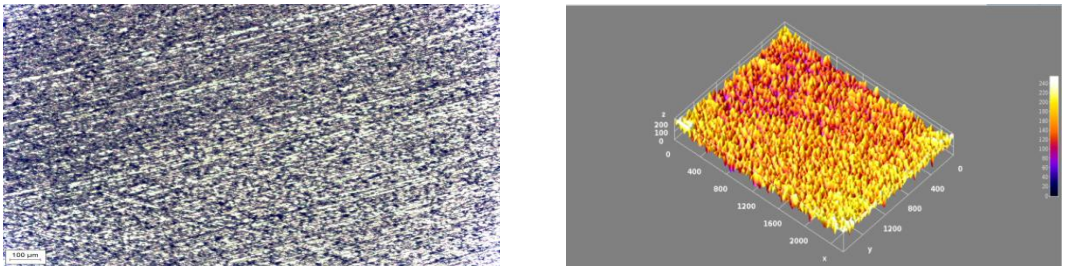

a) b)

Figure 4.99 300 min time He plasma processed aluminum pellet anode surface under Metallographic microscope's light image **a)**50x magnification of the surface **b)**surface 3D graph generated by ImageJ software

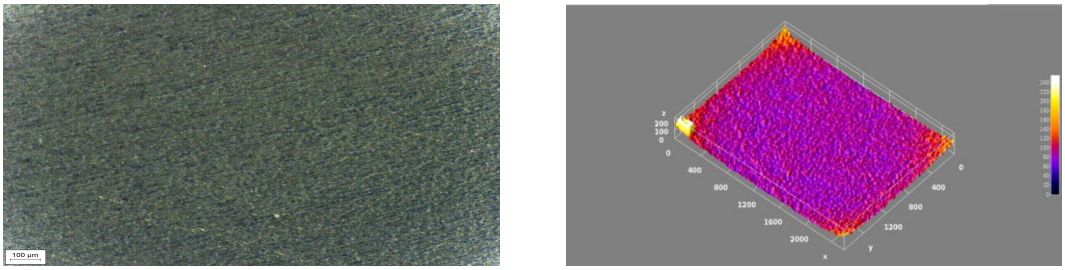

a) b)

Figure 4.100 300 min time He plasma processed aluminum pellet anode surface without Metallographic microscope's light image **a)**50x magnification of the surface **b)**surface 3D graph generated by ImageJ software

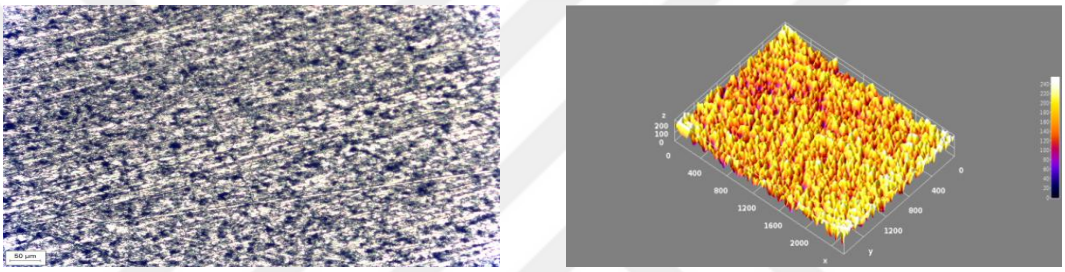

a) b)

Figure 4.101 300 min time He plasma processed aluminum pellet anode surface under Metallographic microscope's light image **a)**100x magnification of the surface **b)**surface 3D graph generated by ImageJ software

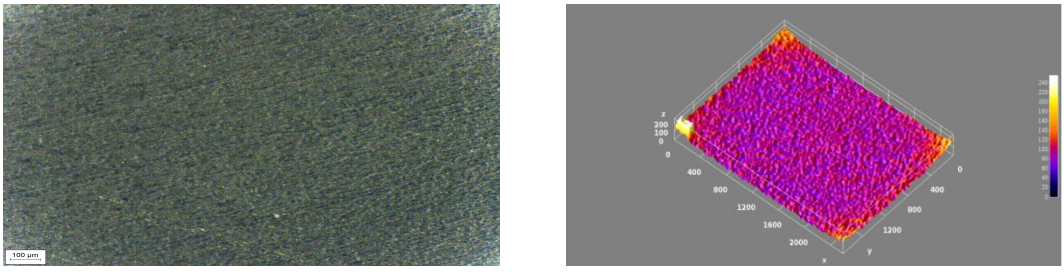

a) b)

Figure 4.102 300 min time He plasma processed aluminum pellet anode surface without Metallographic microscope's light image **a)**100x magnification of the surface **b)**surface 3D graph generated by ImageJ software

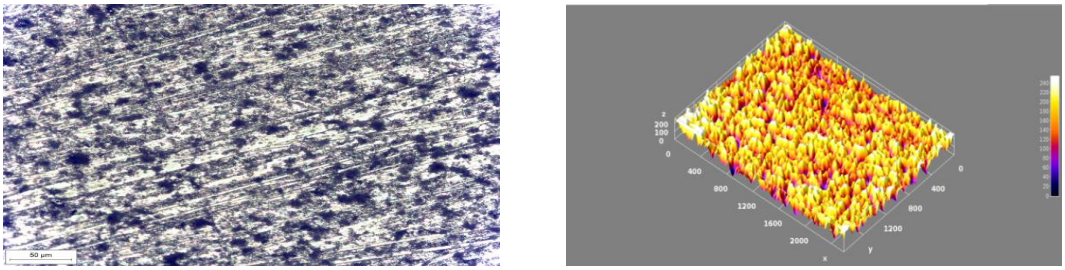

a) b)

Figure 4.103 300 min time He plasma processed aluminum pellet anode surface under Metallographic microscope's light image **a)**200x magnification of the surface **b)**surface 3D graph generated by ImageJ software

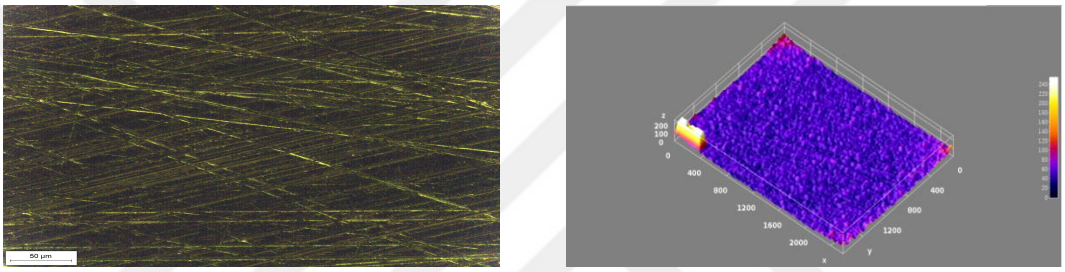

a) b)

Figure 4.104 300 min time He plasma processed aluminum pellet anode surface without Metallographic microscope's light image **a)**200x magnification of the surface **b)**surface 3D graph generated by ImageJ software

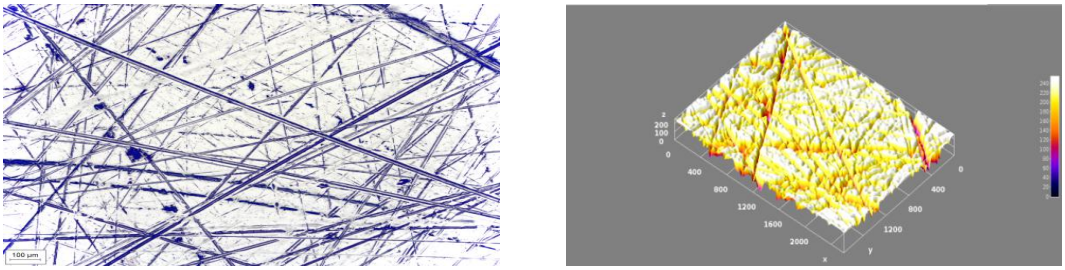

a) b)

Figure 4.105 360 min time He plasma processed aluminum pellet cathode surface under Metallographic microscope's light image **a)**50x magnification of the surface **b)**surface 3D graph generated by ImageJ software

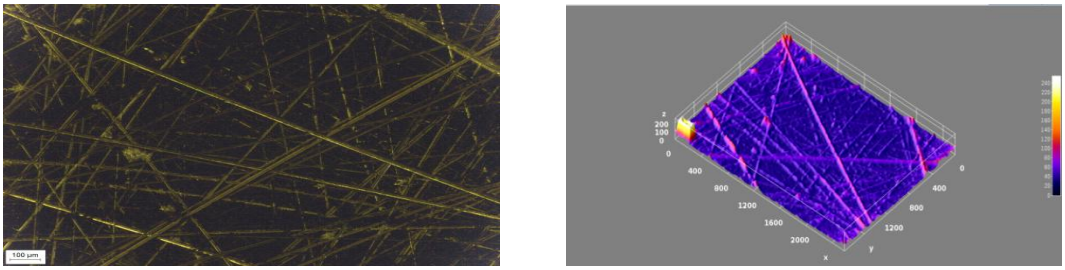

a) b)

Figure 4.106 360 min time He plasma processed aluminum pellet cathode surface without Metallographic microscope's light image **a)**50x magnification of the surface **b)**surface 3D graph generated by ImageJ software

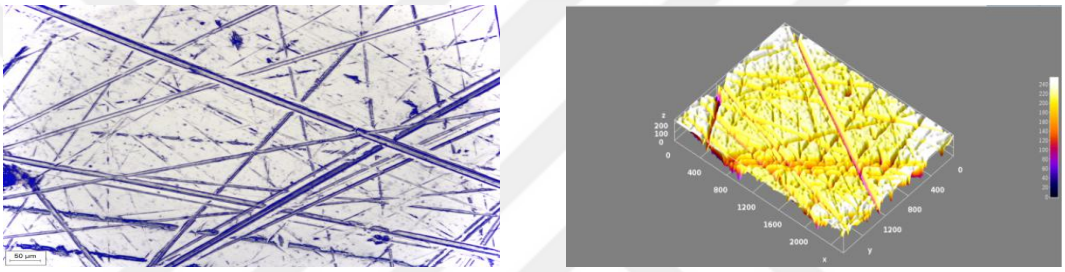

a) b)

Figure 4.107 360 min time He plasma processed aluminum pellet cathode surface under Metallographic microscope's light image **a)**100x magnification of the surface **b**)surface 3D graph generated by ImageJ software

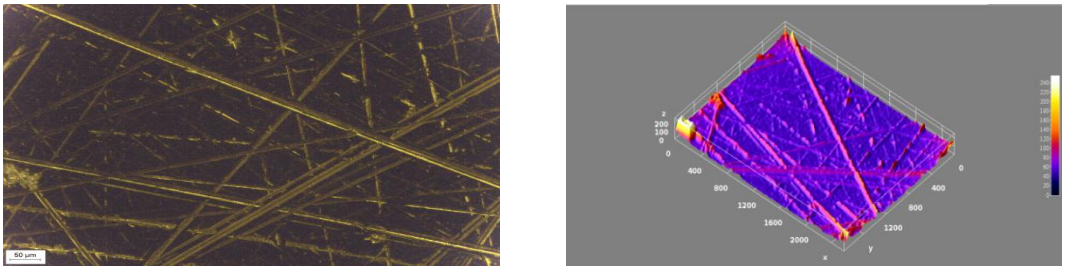

a) b)

Figure 4.108 360 min time He plasma processed aluminum pellet cathode surface without Metallographic microscope's light image **a)**100x magnification of the surface **b)**surface 3D graph generated by ImageJ software

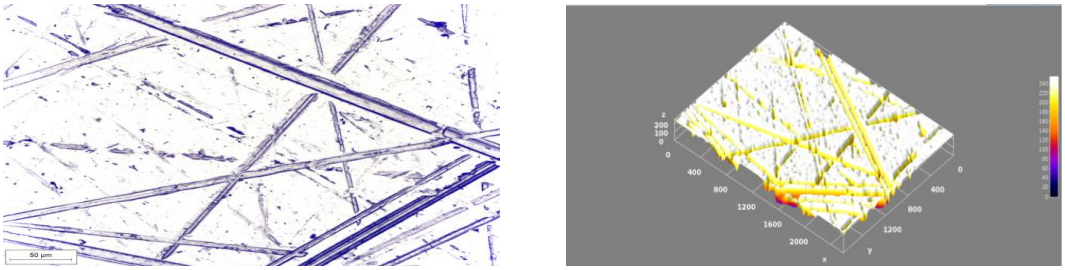

a) b)

Figure 4.109 360 min time He plasma processed aluminum pellet cathode surface under Metallographic microscope's light image **a)**200x magnification of the surface **b)**surface 3D graph generated by ImageJ software

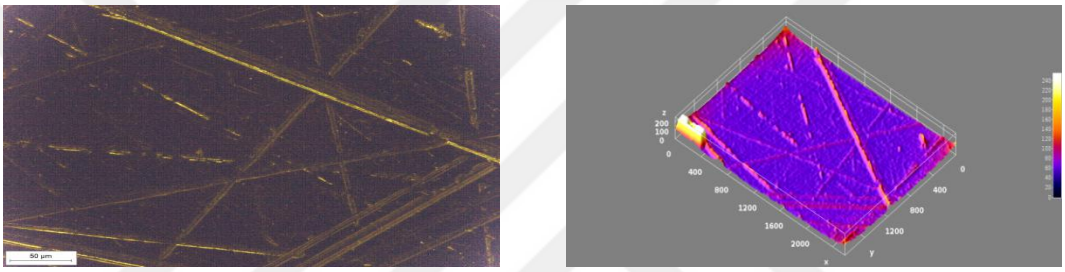

a) b)

Figure 4.110 360 min time He plasma processed aluminum pellet cathode surface without Metallographic microscope's light image **a)**200x magnification of the surface **b)**surface 3D graph generated by ImageJ software

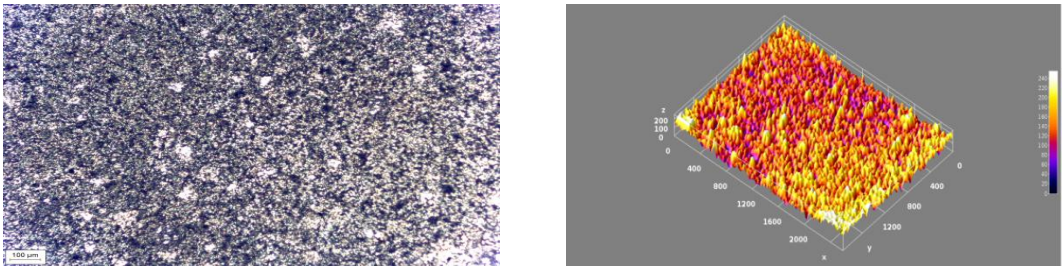

a) b)

Figure 4.111 360 min time He plasma processed aluminum pellet anode surface under Metallographic microscope's light image **a)**50x magnification of the surface **b)**surface 3D graph generated by ImageJ software

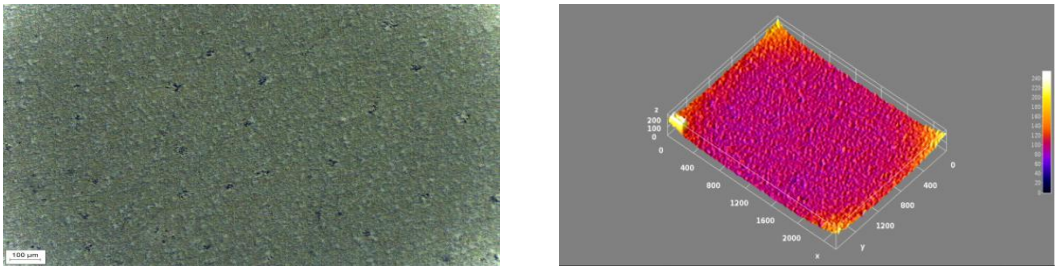

a) b)

Figure 4.112 360 min time He plasma processed aluminum pellet anode surface without Metallographic microscope's light image **a)**50x magnification of the surface **b)**surface 3D graph generated by ImageJ software

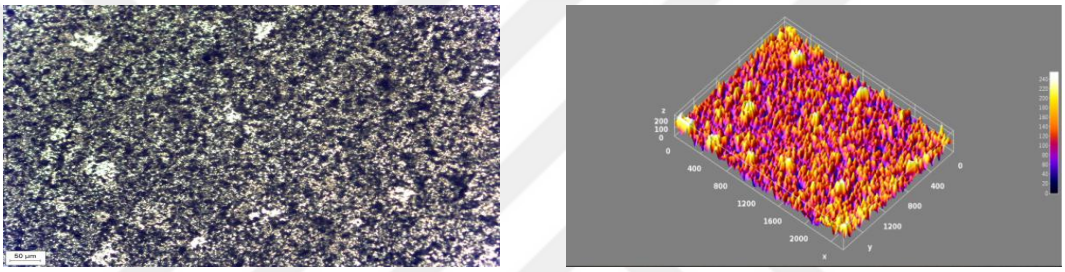

a) b)

Figure 4.113 360 min time He plasma processed aluminum pellet anode surface under Metallographic microscope's light image **a)**100x magnification of the surface **b)**surface 3D graph generated by ImageJ software

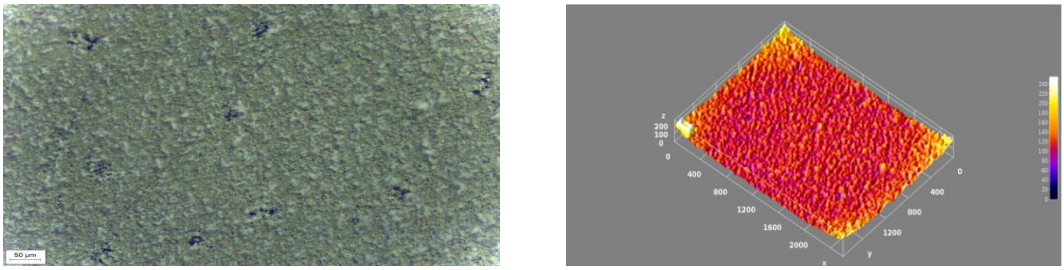

a) b)

Figure 4.114 360 min time He plasma processed aluminum pellet anode surface without Metallographic microscope's light image **a)**100x magnification of the surface **b)**surface 3D graph generated by ImageJ software

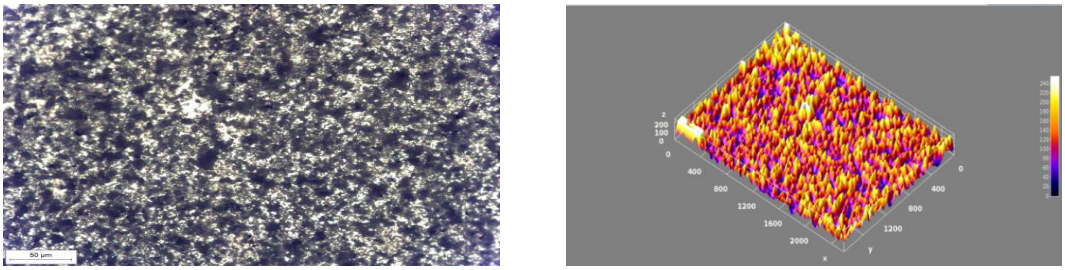

a) b)

Figure 4.115 360 min time He plasma processed aluminum pellet anode surface under Metallographic microscope's light image **a)**200x magnification of the surface **b)**surface 3D graph generated by ImageJ software

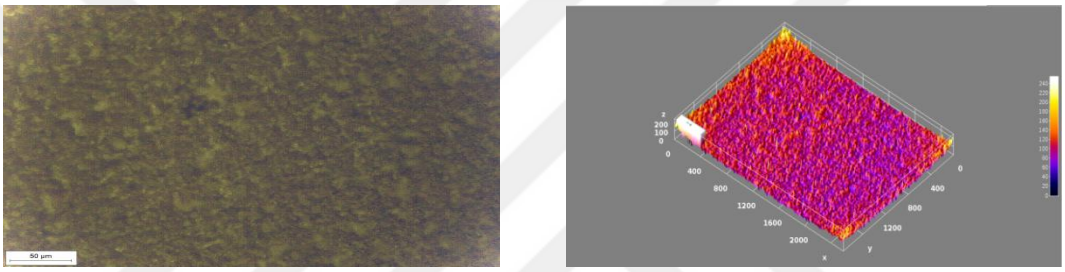

a) b)

Figure 4.116 360 min time He plasma processed aluminum pellet anode surface without Metallographic microscope's light image **a)**200x magnification of the surface **b)**surface 3D graph generated by ImageJ software

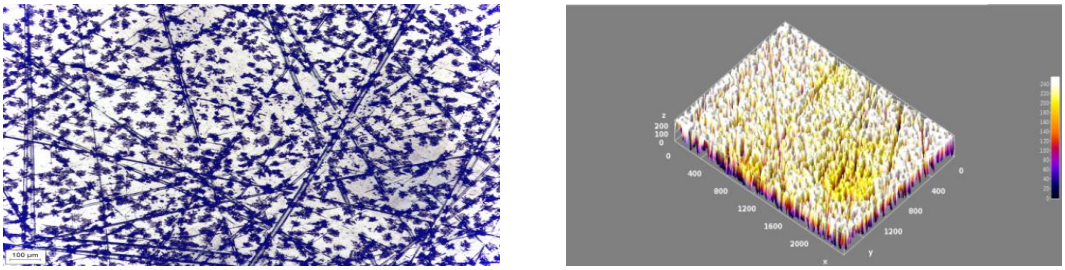

a) b)

Figure 4.117 360 min time He plasma processed arc burned aluminum pellet anode surface under Metallographic microscope's light image a)50x magnification of the surface b)surface 3D graph generated by ImageJ software

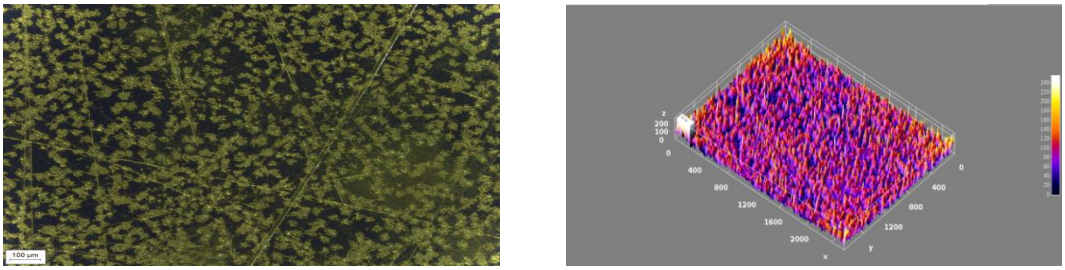

a) b)

Figure 4.118 360 min time He plasma processed arc burned aluminum pellet anode surface without Metallographic microscope's light image **a)**50x magnification of the surface **b)**surface 3D graph generated by ImageJ software

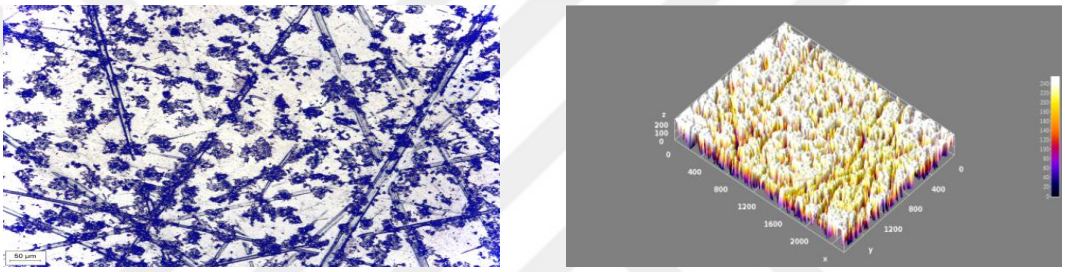

a) b)

Figure 4.119 360 min time He plasma processed arc burned aluminum pellet anode surface under Metallographic microscope's light image **a)**100x magnification of the surface **b)**surface 3D graph generated by ImageJ software

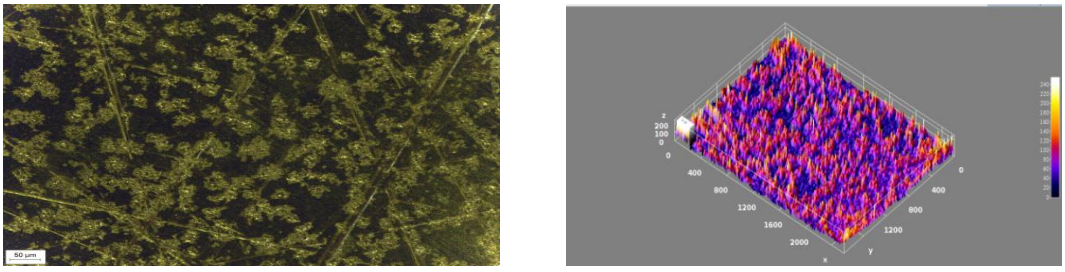

a) b)

Figure 4.120 360 min time He plasma processed arc burned aluminum pellet anode surface without Metallographic microscope's light image **a)**100x magnification of the surface **b)**surface 3D graph generated by ImageJ software

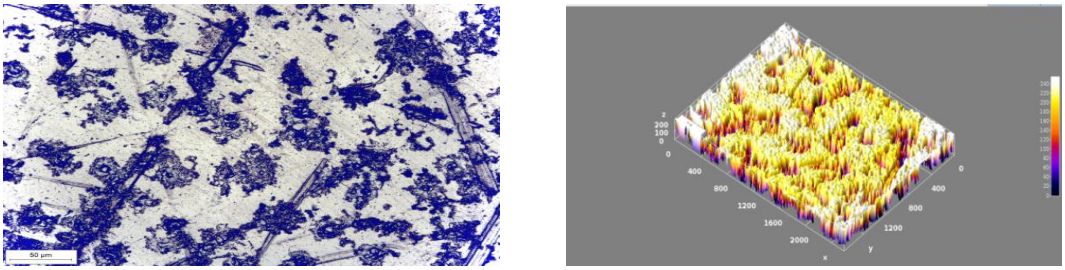

a) b)

Figure 4.121 360 min time He plasma processed arc burned aluminum pellet anode surface under Metallographic microscope's light image **a)**200x magnification of the surface **b)**surface 3D graph generated by ImageJ software

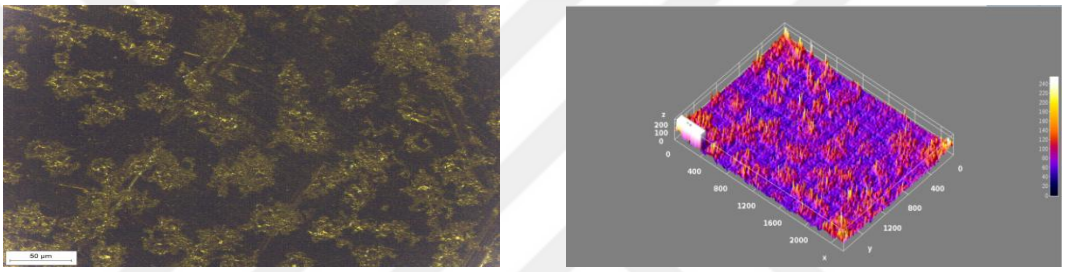

a) b)

Figure 4.122 360 min time He plasma processed arc burned aluminum pellet anode surface without Metallographic microscope's light image **a)**200x magnification of the surface **b)**surface 3D graph generated by ImageJ software

4.4 Scanning Probe Microscopy (Atomic Force Microscope) Measurements

60, 300, and 360-minutes Al anode and cathode surface AFM observations are made as 3D surface plots, RMS and Sa values. In Chapter 3 Scanning Probe Microscopy (Atomic Force Microscope) Observations method is described.

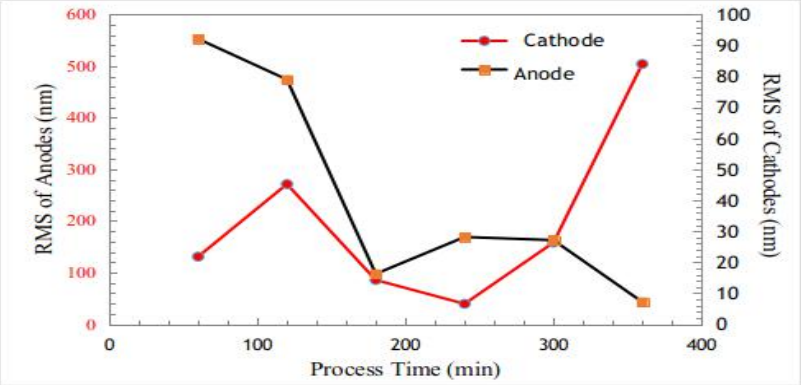

Figure 4.123 RMS values of anode and cathode plates

Figure 4.123 shows Al plate AFM RMS surface roughness values under He plasma at anode and cathode. AFM investigation shows Al pellet surface roughness for varied He plasma process times. AFM pictures of Al pellet surfaces with a 5 m radius cross section are also taken. Figure 4.124 shows 60, 300, and 360-minute AFM profile graphs.

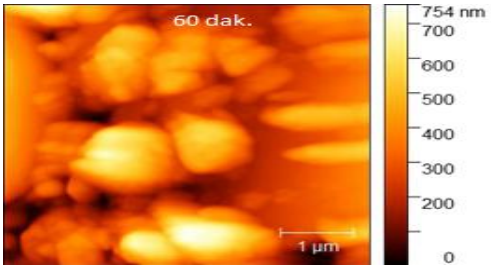

a)AFM image of Al plate with 60 min process time

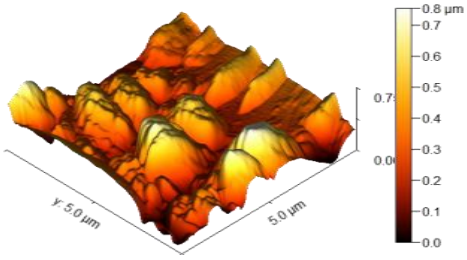

b)3D plot of AFM image of Al plate with 60 min process time

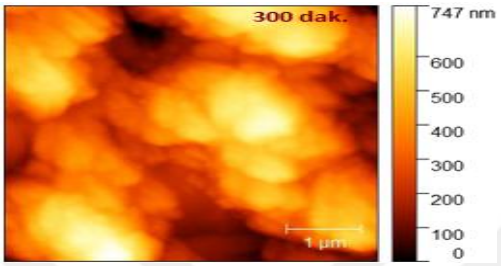

c)AFM image of Al plate with 300 min process time

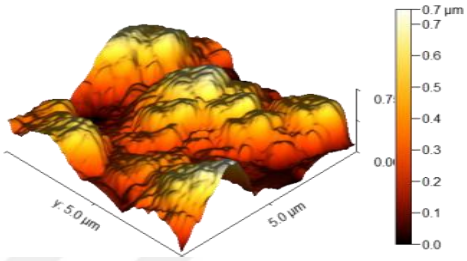

d)3D plot of AFM image of Al plate with 300 min process time

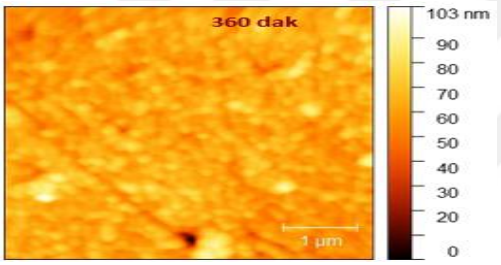

e)AFM image of Al plate with 360 min process time

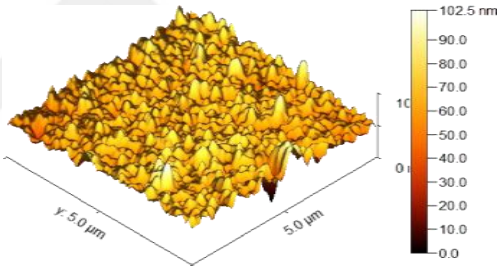

f)3D plot of AFM image of Al plate with 360 min process time

Figure 4.124 a), b), c), d), e), f) show 2D and 3D profiles AFM images of Al plates with 0, 300 and 360 process times

Equations (3.22) and (3.23) determine and α. Equation (3.24) calculates reliability using and assuming as 0. From AFM measurements following table is measured for RMS and Sa values for different process times under the He plasma. Table 4.1 shows RMS and Sa values establish the characteristic equation of Al samples in equation (3.8).

Table 4.1 He Plasma Al plate Roughness Failure Data Set based on AFM measurements

Sample Label	Process Time (min)	RMS (µm)	Sa (µm)
60 min,5µm,Cathode	60	92.1	77.5
120 min, 5µm,Cathode	120	79.0	61.8
180 min,5µm,Cathode	180	16.2	12.9
240 min,5µm,Cathode	240	28.2	22.0
300 min,5µm,Cathode	300	27.1	21.8
360 min,5µm,Cathode	360	7.2	5.3
60 min,5µm,Anode	60	130.9	103.4
120 min,5µm,Anode	120	271.3	223.3
180 min,5µm,Anode	180	85.6	58.6
240 min,5µm,Anode	240	39.4	30.9
300 min,5µm,Anode	300	158.1	132.0
360 min,5µm,Anode	360	504.1	419.8

Figure 4.5 shows the Al anode anode and cathode Weibull material reliability calculation graph based on RMS and Sa values versus process duration in minutes. Weibull Reliability method is described in Chapter 3 Weibull Reliability Method section. The calculated F(t) and y(t) values are given in Tables-2 and 3 for anode and cathode Al plates, respectively. Tables 4.2 and 4.3 demonstrate anode and cathode surface roughness-dependent outcomes.

Table 4.2 F(t) and y(t) values calculated by equations (3.26) and (3.27) for Al plate at anode.

Process time (min)	Sa (m)	RMS (µm)	F(t)	ln(RMS)	ln (Sa)	y(t)
60	103,4	130,9	0,1093	4,8744	4,6386	-2,1556
120	223,3	271,3	0,2656	5,6032	5,4085	-1,1752
180	58,6	85,6	0,4218	4,4496	4,0707	-0,6015
240	30,9	39,4	0,5781	3,6737	3,4307	-0,1472
300	132	158,1	0,7343	5,0632	4,8828	0,2819
360	419,8	504,1	0,8906	6,2227	6,0397	0,7943

Table 4.3 F(t) and y values calculated by equations (3.26) and (3.27) for Al plate at cathode.

Process time (min)	Sa (m)	RMS (µm)	F(t)	ln(RMS)	ln (Sa)	y(t)
60	77,5	92,1	0,1093	4,5228	4,3502	-2,1556
120	61,8	79	0,2656	4,3694	4,1239	-1,1752
180	12,9	16,2	0,4218	2,7850	2,5572	-0,6015
240	22	28,2	0,5781	3,3393	3,0910	-0,1472
300	21,8	27,1	0,7343	3,2995	3,0819	0,2819
360	5,3	7,2	0,8906	1,9740	1,6677	0,7943

Figure 4.125 and figure 4.126 show calculated y(t) values versus ln(t) based on surface roughness and mean surface roughness for Al plate placed at cathode while.

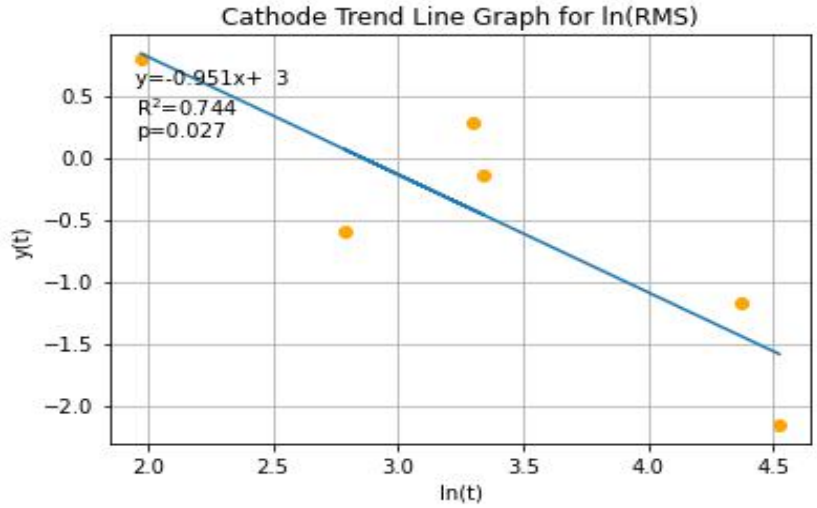

Figure 4.125 Calculated y(t) values as a function of ln(t) by using measured RMS values for cathode plate

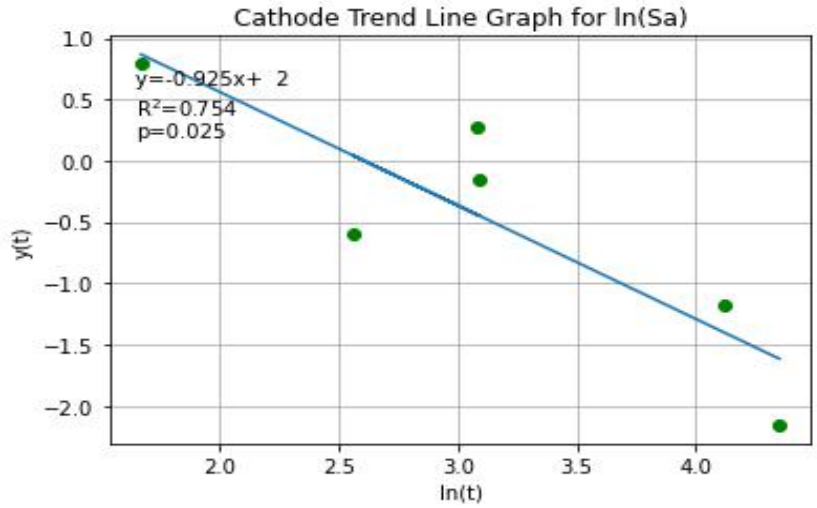

Figure 4.126 Calculated y(t) values as a function of ln(t) by using measured Sa values for cathode plate

Figure 4.127 and figure 4.128 show calculated y(t) versus ln(t) based on roughness and mean surface roughness for Al plate placed at anode.

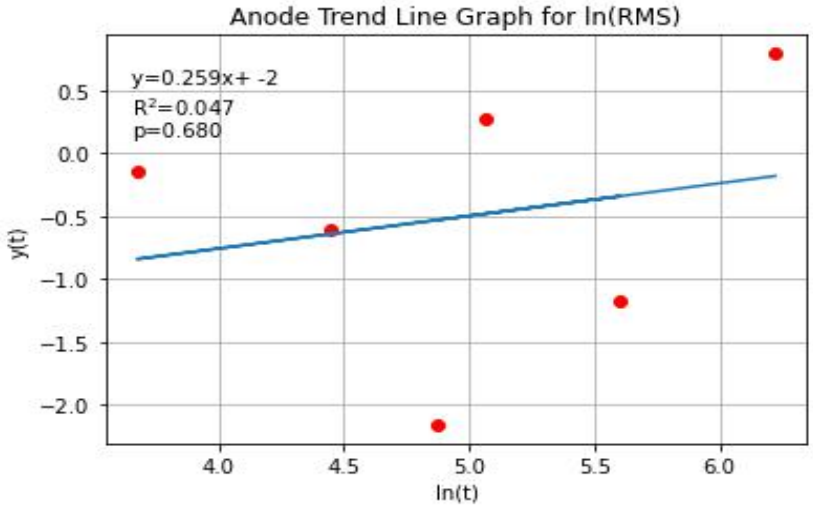

Figure 4.127 Calculated y(t) values as a function of ln(t) by using measured RMS values for anode plate

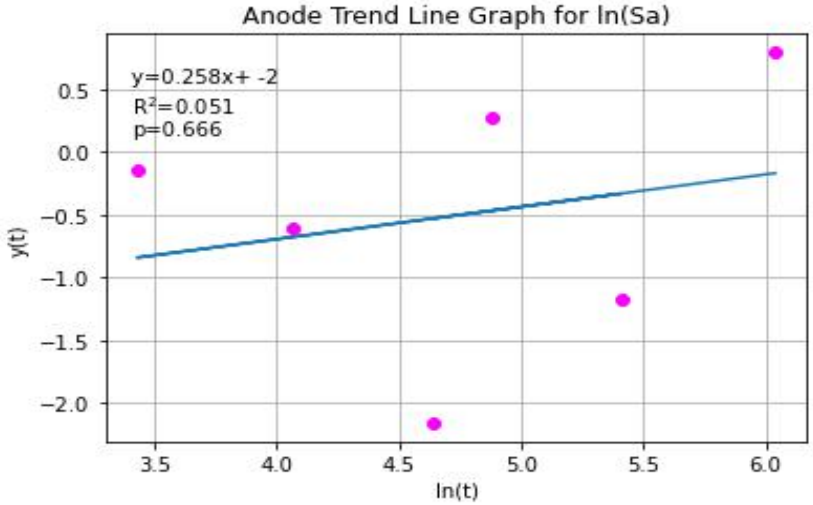

Figure 4.128 Calculated y(t) values as a function of ln(t) by using measured Sa values for anode plate.

The trend line function in graphs (Figures 4.125-4.128), calculates β and α values in equations (3.26) and (3.27). To compute equation (1) dependability, use α and β and assume as 0. Figure 4.129 displays Al surface anode RMS and SA reliability values as a function of process duration in minutes. Over time, He plasma scratches the Al anode surface, reducing reliability. Over time, Al surface reliability degrades, causing anode failure. The rising failure rate suggests ion radiation may cause material defects or death.

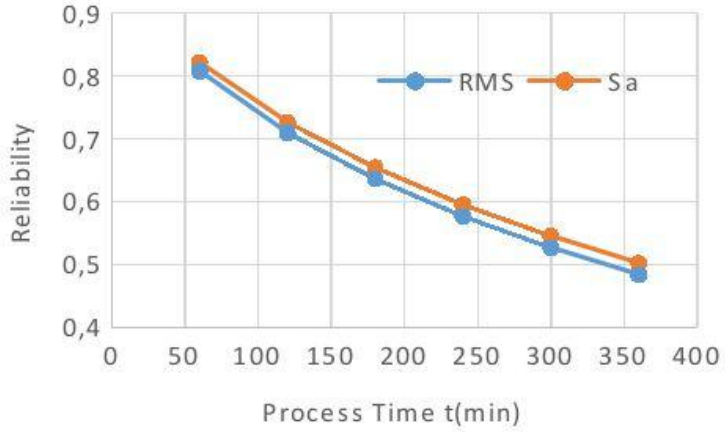

Figure 4.129 Material reliability based on RMS and Sa for Al anode pellet

RMS and Sa at the Al anode pellet reveal that He plasma intensively etching lowers material dependability over time. Figure 4.130 shows RMS and Sa material reliability values for Al cathode pellets versus process duration in minutes.

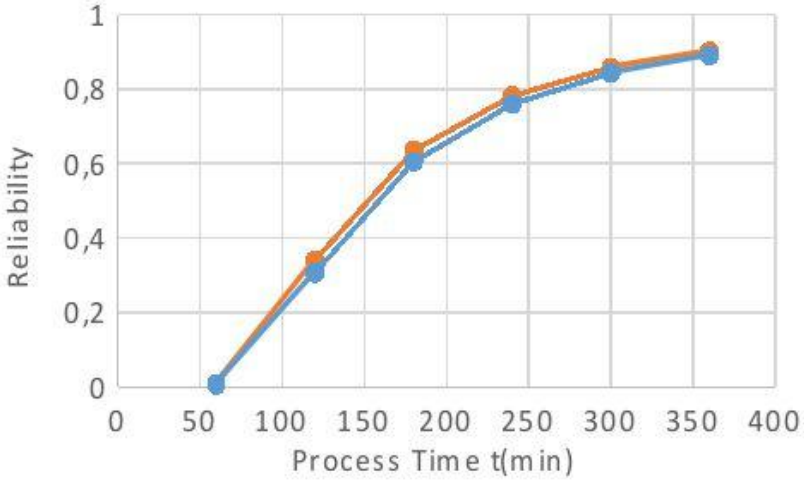

Figure 4.130 Material reliability based on the values of RMS and Sa for Al cathode pellet

As Al accumulates on the anode's surface, it degrades. Due to his insolubility in metals such as Al, he can diffuse a long channel and create vacancy defects by self-trapping at kinetic energies below the metal displacement threshold. He vacancy complexes can confine He atoms until the solidification of hill-type surfaces. When

these reactions occur close to the surface, metal atoms shift, fragment, and nanofibers form. Backscattered He neutrals interact with the Al surface to produce the same result as He ion implantation within metals.

Time degrades Al anode surface dependability, increasing failure rate. Ion penetration may cause surface flaws or material mortality if the failure rate is significant. He plasma thickly etching Al reduces material dependability. In the last graph, Al cathode pellet material dependability grows over time. The plasma sheath at cathodes and anodes affects structure. Electrode erosion, thermionic emission, plasma heat flux to the wall, and other reactions occur at the cathode, spot, and anode attachments. Plasma glow discharge influenced anode-cathode plasma interactions, according to the experiment.

4.5 SEM Observations and EDS Characterization Results

In figures 4.131, 4.132, 4.133, 4.134, 4.135 and 4.136, SEM images of the Al Anode and Al Cathode pellets surfaces with the different periods He plasma processed images are given in different resolutions and magnifications. In SEM, element characterization of the surface materials after the experiment is also performed by using EDS device. Chapter 3 Material and Method section Scanning Electron Microscopy and Energy Dispersive X-ray Analysis in SEM methods are described in detailed.

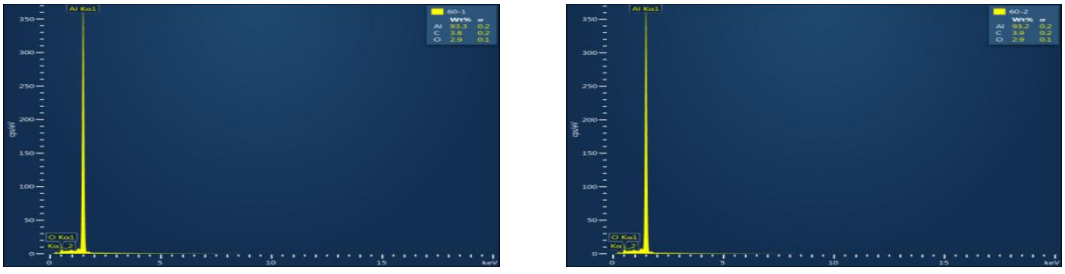

a) b)

Figure 4.131 He plasma processed Al pellet surface EDS Material Analysis Graph in keV **a)**60 Min He plasma processed Al cathode surface material analysis of center cross section **b)**60 Min He plasma processed Al cathode surface material analysis of edge cross section

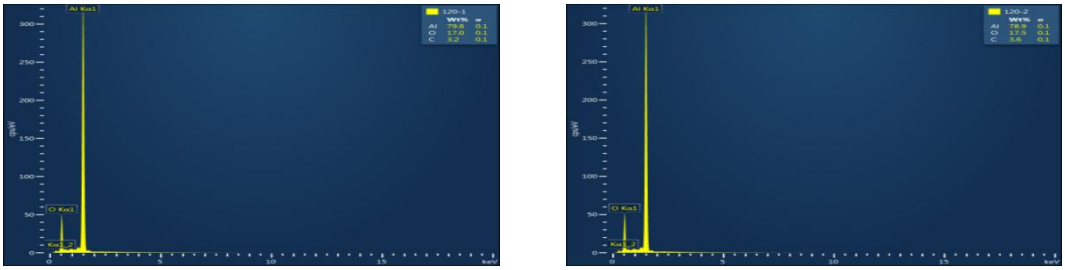

a) b)

Figure 4.132 He plasma processed Al pellet surface EDS Material Analysis Graph in keV **a)**120 Min He plasma processed Al anode surface material analysis of center cross section **b)**120 Min He plasma processed Al anode surface material analysis of edge cross section

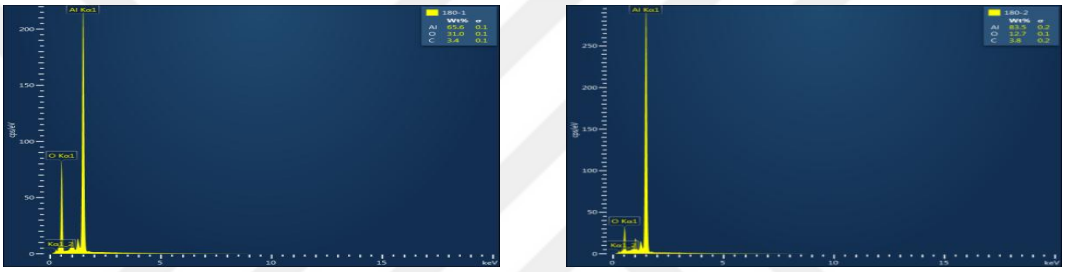

a) b)

Figure 4.133 He plasma processed Al pellet surface EDS Material Analysis Graph in keV **a)**180 Min He plasma processed Al anode surface material analysis of center cross section **b)**180 Min He plasma processed Al anode surface material analysis of edge cross section

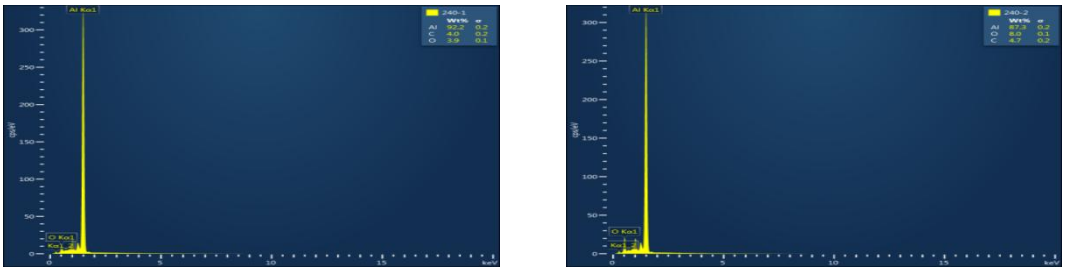

a) b)

Figure 4.134 He plasma processed Al pellet surface EDS Material Analysis Graph in keV **a)**240 Min He plasma processed Al cathode surface material analysis of center cross section **b)**240 Min He plasma processed Al cathode surface material analysis of edge cross section

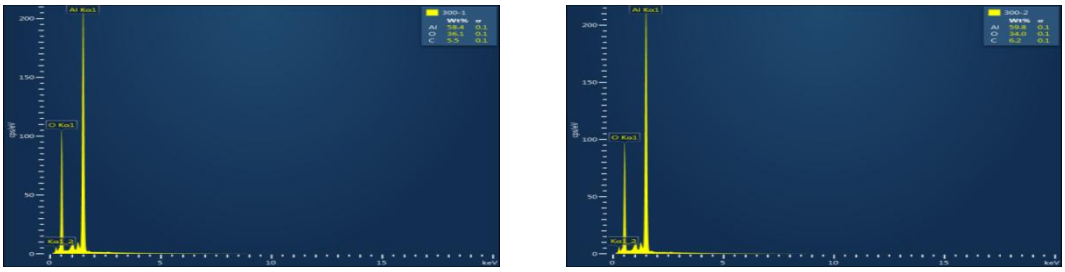

a) b)

Figure 4.135 He plasma processed Al pellet surface EDS Material Analysis Graph in keV **a)**300 Min He plasma processed Al anode surface material analysis of center cross section **b)**300 Min He plasma processed Al anode surface material analysis of edge cross section

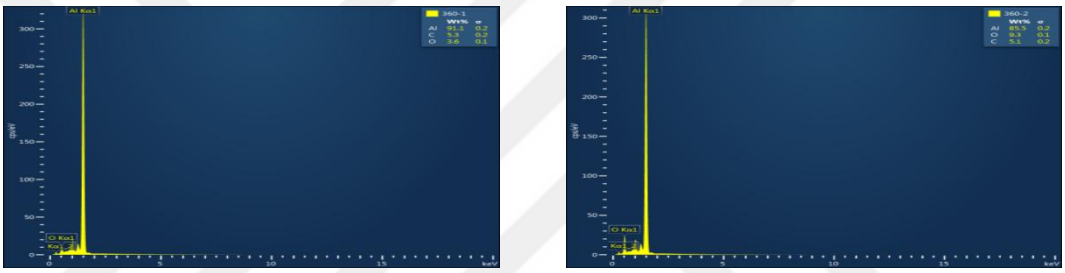

a) b)

Figure 4.136 He plasma processed Al pellet surface EDS Material Analysis Graph in keV **a)**360 Min He plasma processed Al cathode surface material analysis of center cross section **b)**360 Min He plasma processed Al cathode surface material analysis of edge cross section

Between Figure 4.137 to Figure 4.160 shows the example of the SEM images. SEM analysis are performed in Ankara Yıldırım Beyazıt University MERLAB (Central Research Lab). These images show the maximum magnification till 3 micron SEM images for different He process times. Images are taken from the center midpoint and the edges of the anode and cathode of Pellet surfaces. Based on the cost of the SEM, images are taken for 60 min, 240 min, 360 min cathode surface and 120 min, 180 min and 300 min anode surface pellets.

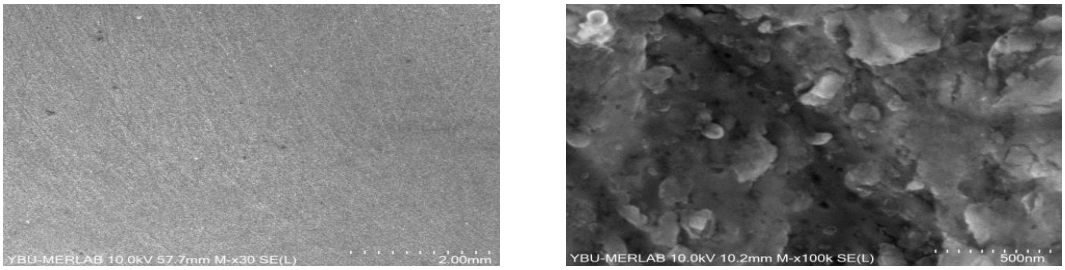

a) b)

Figure 4.137 He plasma processed Al Anode-Al Cathode Surface SEM View **a)**120 Min He plasma processed Al anode 2mm view image **b)**120 Min He plasma processed Al anode 500nm view image

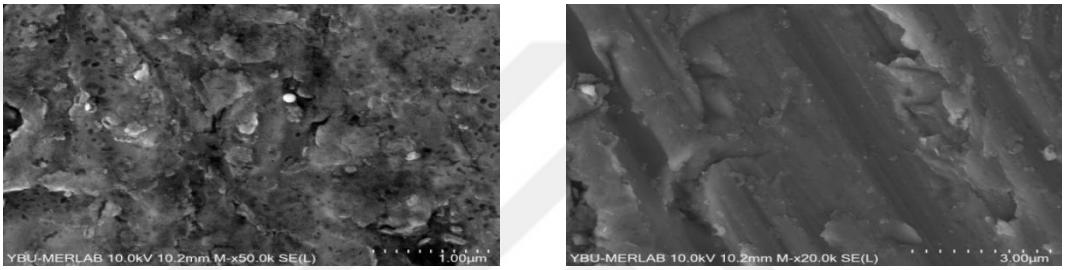

a) b)

Figure 4.138 He plasma processed Al Anode-Al Cathode Surface SEM View **a)**120 Min He plasma processed Al anode 1µm view image **b)**120 Min He plasma processed Al anode 3µm view image

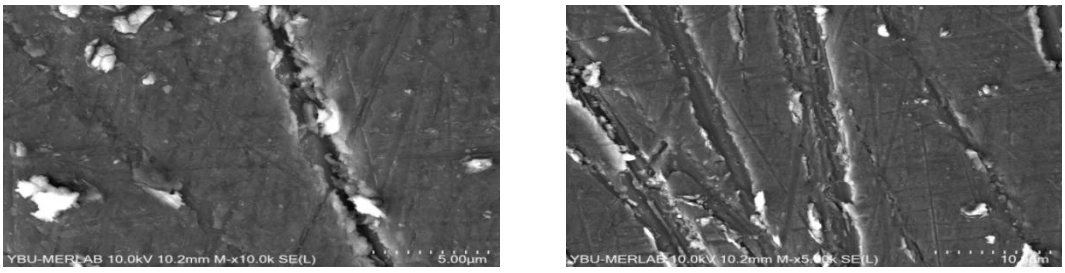

a) b)

Figure 4.139 He plasma processed Al Anode-Al Cathode Surface SEM View **a)**120 Min He plasma processed Al anode 5µm view image **b)**120 Min He plasma processed Al anode 10µm view image

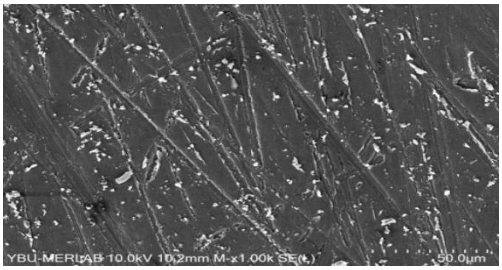

Figure 4.140 He plasma processed Al Anode-Al Cathode Surface SEM View-120 Min He plasma processed Al anode 5µm view image

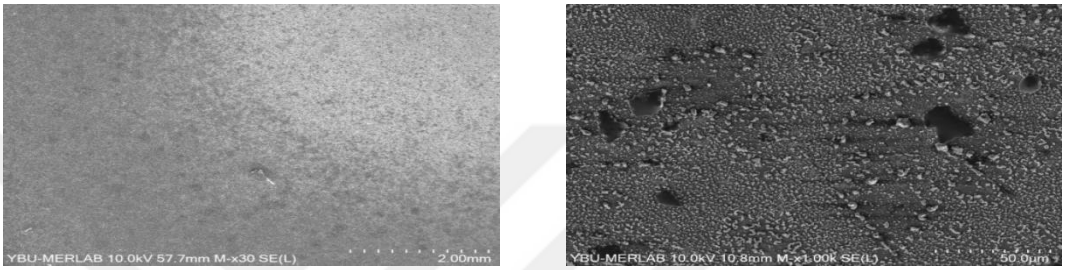

a) b)

Figure 4.141 He plasma processed Al Anode-Al Cathode Surface SEM View **a)**180 Min He plasma processed Al anode 2mm view image **b)**180 Min He plasma processed Al anode 50µm view image

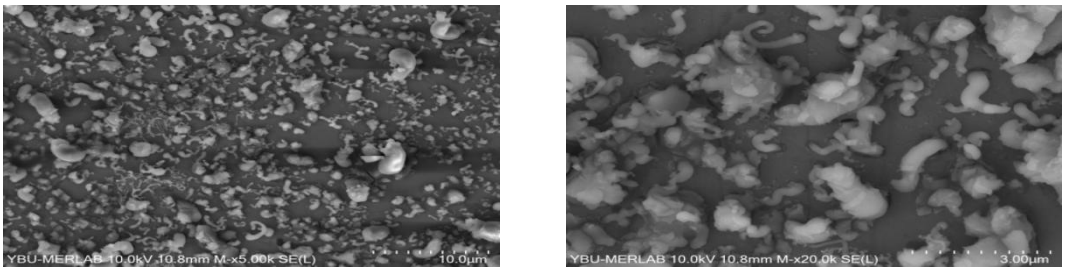

a) b)

Figure 4.142 He plasma processed Al Anode-Al Cathode Surface SEM View **a)**180 Min He plasma processed Al anode 10µm view image **b)**180 Min He plasma processed Al anode 3µm view image

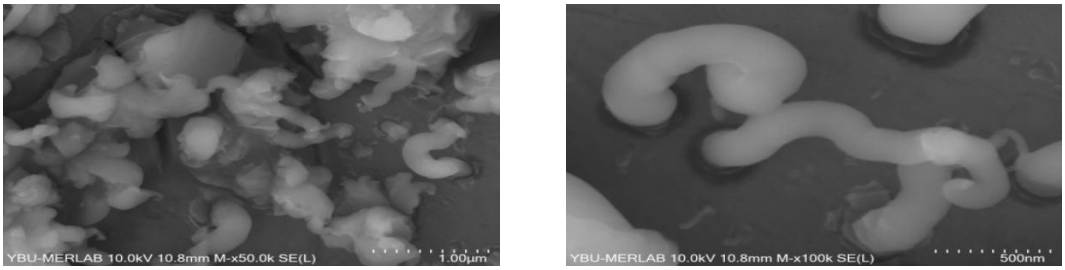

a) b)

Figure 4.143 He plasma processed Al Anode-Al Cathode Surface SEM View **a)**180 Min He plasma processed Al anode 1µm view image **b)**180 Min He plasma processed Al anode 500nm view image

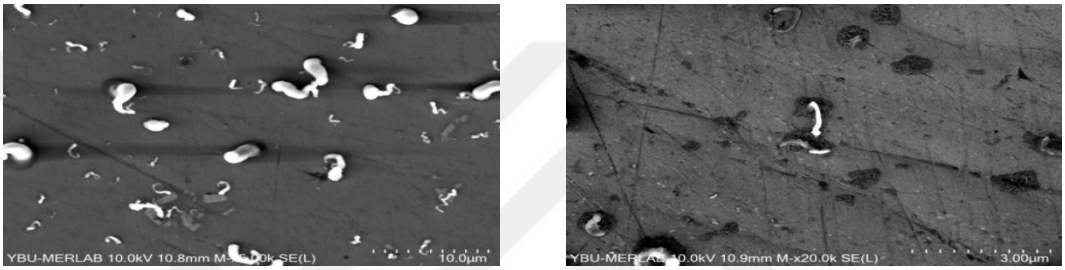

a) b)

Figure 4.144 He plasma processed Al Anode-Al Cathode Surface SEM View a)180 Min He plasma processed Al anode 10µm view image b)180 Min He plasma processed Al anode 3µm view image

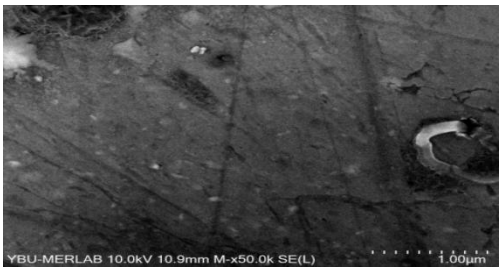

Figure 4.145 He plasma processed Al Anode-Al Cathode Surface SEM View-180 Min He plasma processed Al anode 1µm view image

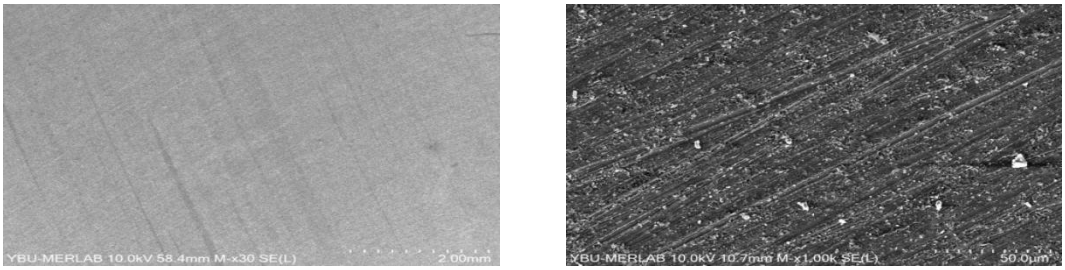

a) b)

Figure 4.146 He plasma processed Al Anode-Al Cathode Surface SEM View **a)**300 Min He plasma processed Al anode 2mm view image **b)**300 Min He plasma processed Al anode 50µm view image

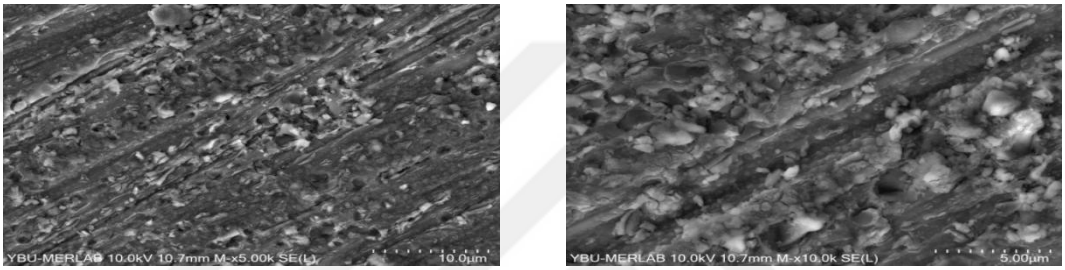

a) b)

Figure 4.147 He plasma processed Al Anode-Al Cathode Surface SEM View **a)**300 Min He plasma processed Al anode 10µm view image **b)**300 Min He plasma processed Al anode 5µm view image

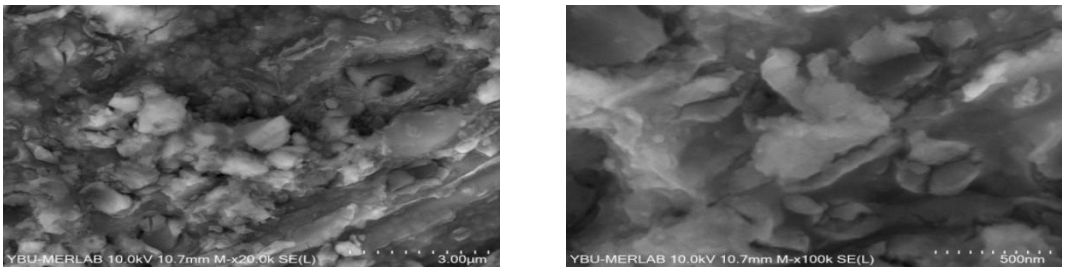

a) b)

Figure 4.148 He plasma processed Al Anode-Al Cathode Surface SEM View **a)**300 Min He plasma processed Al anode 3 µm view image **b)**300 Min He plasma processed Al anode 500nm view image

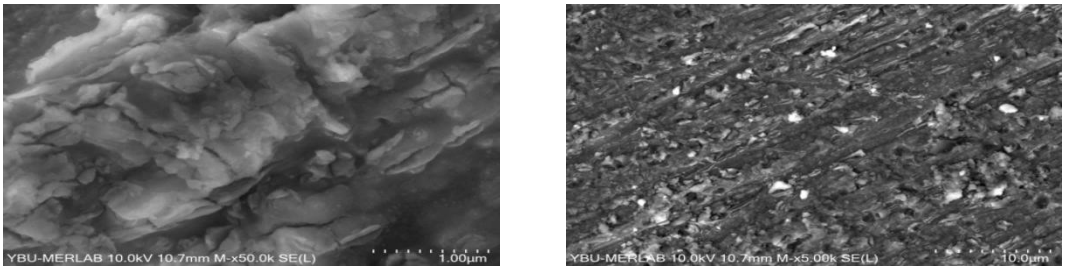

a) b)

Figure 4.149 He plasma processed Al Anode-Al Cathode Surface SEM View **a)**300 Min He plasma processed Al anode 1 μm view image **b)**300 Min He plasma processed Al anode 10 μm view image

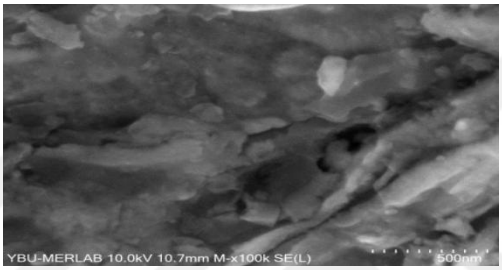

Figure 4.150 He plasma processed Al Anode-Al Cathode Surface SEM View-300 Min He plasma processed Al anode 500nm view image

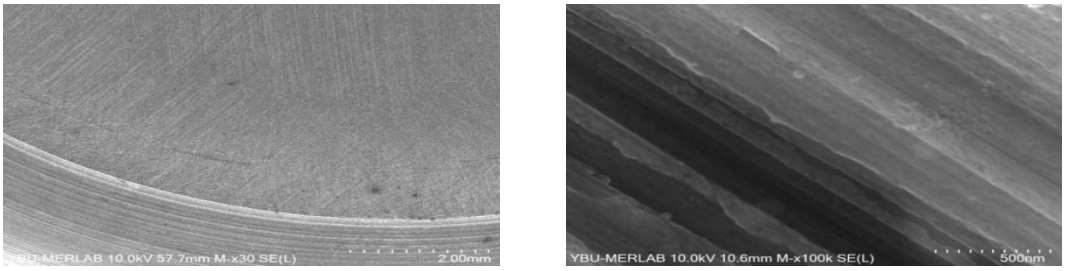

a) b)

Figure 4.151 He plasma processed Al Anode-Al Cathode Surface SEM View **a)**60 Min He plasma processed Al cathode 2mm view image **b)**60 Min He plasma processed Al cathode 500nm view image

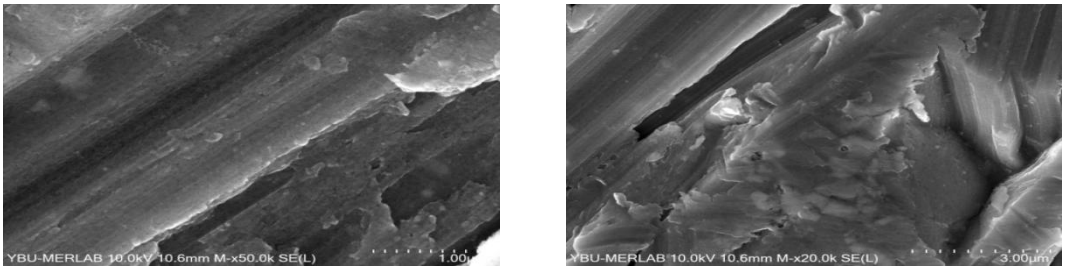

a) b)

Figure 4.152 He plasma processed Al Anode-Al Cathode Surface SEM View **a)**60 Min He plasma processed Al cathode 1µm view image **b)**60 Min He plasma processed Al cathode 3µm view image

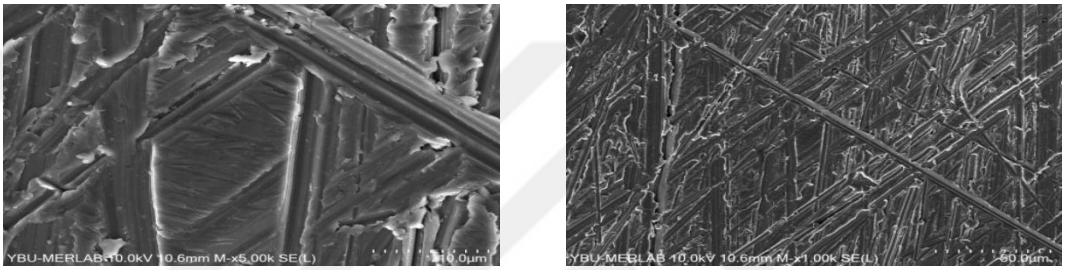

a) b)

Figure 4.153 He plasma processed Al Anode-Al Cathode Surface SEM View **a)**60 Min He plasma processed Al cathode 10µm view image **b)**60 Min He plasma processed Al cathode 50µm view image

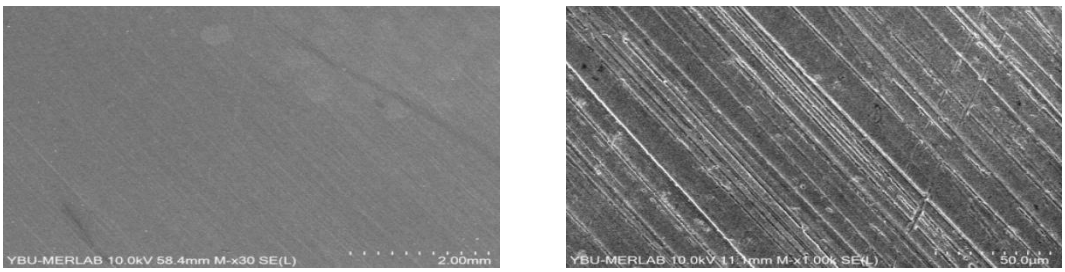

a) b)

Figure 4.154 He plasma processed Al Anode-Al Cathode Surface SEM View **a)**240 Min He plasma processed Al cathode 2mm view image **b)**240 Min He plasma processed Al cathode 50µm view image

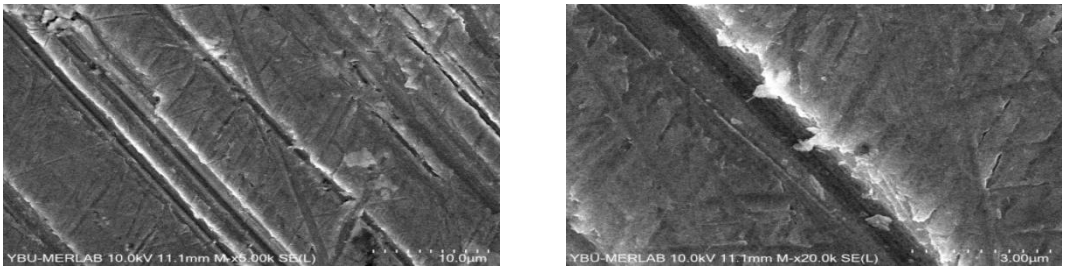

a) b)

Figure 4.155 He plasma processed Al Anode-Al Cathode Surface SEM View a)240 Min He plasma processed Al cathode 10µm view image b)240 Min He plasma processed Al cathode 3µm view image

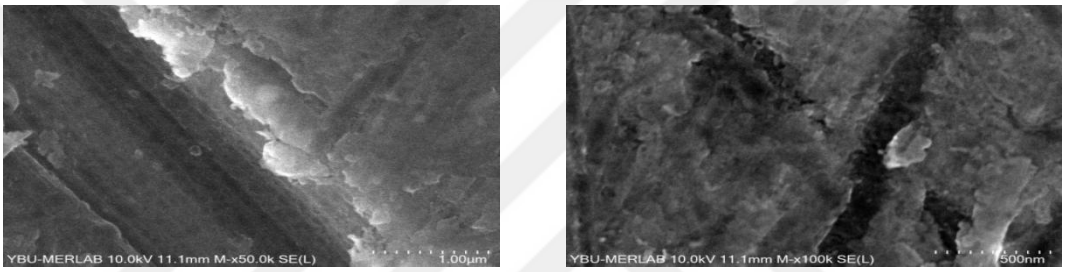

a) b)

Figure 4.156 He plasma processed Al Anode-Al Cathode Surface SEM View **a)**240 Min He plasma processed Al cathode 1µm view image **b)**240 Min He plasma processed Al cathode 500nm view image

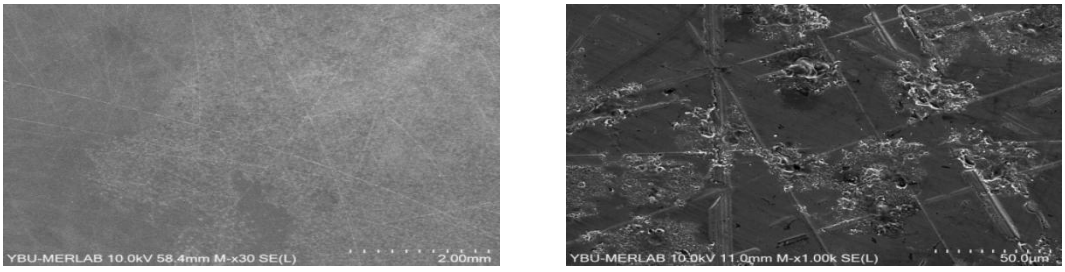

a) b)

Figure 4.157 He plasma processed Al Anode-Al Cathode Surface SEM View **a)**360 Min He plasma processed Al cathode 2mm view image **b)**360 Min He plasma processed Al cathode 50µm view image

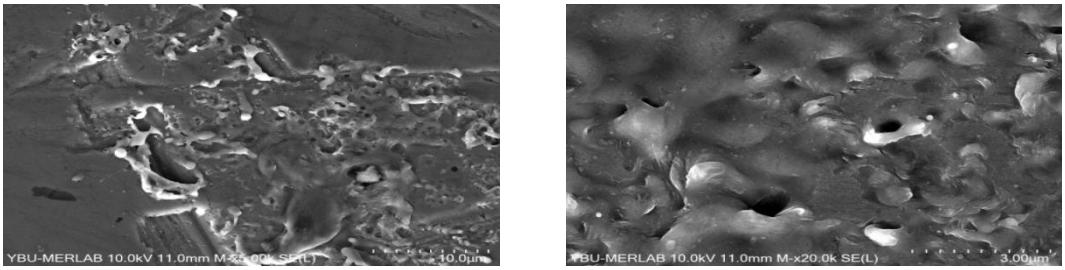

a) b)

Figure 4.158 He plasma processed Al Anode-Al Cathode Surface SEM View **a)**360 Min He plasma processed Al cathode 10µm view image **b)**360 Min He plasma processed Al cathode 3µm view image

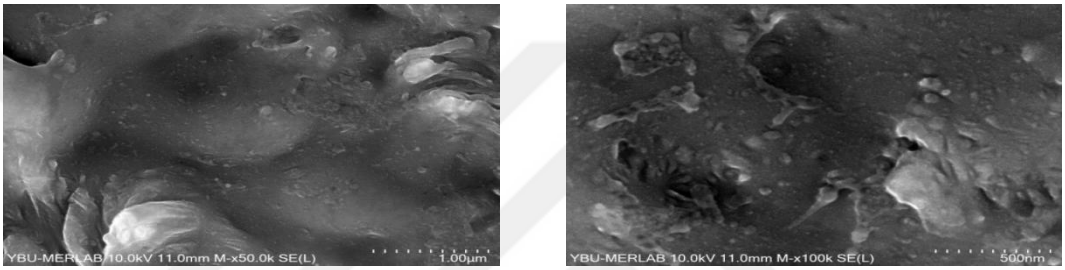

a) b)

Figure 4.159 He plasma processed Al Anode-Al Cathode Surface SEM View **a)**360 Min He plasma processed Al cathode 1µm view image **b)**360 Min He plasma processed Al cathode 500nm view image

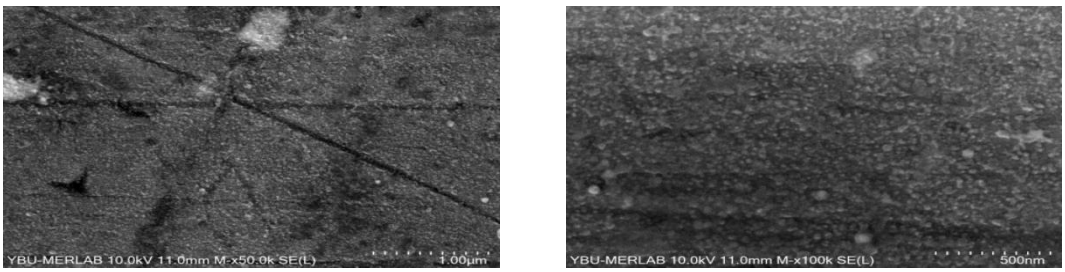

a) b)

Figure 4.160 He plasma processed Al Anode-Al Cathode Surface SEM View a360 Min He plasma processed Al cathode 1µm view image b)360 Min He plasma processed Al cathode 500nm view image

4.6 ImageJ Software Analysis and Their Correlation Results with the AFM Measurements

From the SEM images of the experimental setup Al pellets, optical roughness measurements are performed with the ImageJ software. For this purpose ImageJ produce optical surface roughness parameters are given in Table 4.4. Optical surface roughness measurements analysis in ImageJ software is described in Chapter 3 Material Method Scanning Electron and ImageJ Software Analysis section in detail.

Table 4.4 He Plasma Al plate SEM Image Optical Roughness Failure Data Set

Sample Image Label	Ra	Rq	Rku	Rsk	Rv	Rp	Rt
60 min,2mm,Cathode	146.699	144.636	1.047	1.139	255	65	320
60 min, 500nm,Cathode	94.475	87.323	1.221	1.675	255	15	270
60 min,1µm,Cathode	91.764	84.420	1.313	2.114	255	3	258
60 min,3µm,Cathode	96.324	89.212	1.270	1.905	255	0	255
60 min,10µm,Cathode	95.300	88.055	1.298	2.035	255	0	255
60 min,50µm,Cathode	90.370	80.283	1.433	2.533	255	0	255
240 min,2mm,Cathode	126.826	125.879	1.025	1.080	255	74	329
240 min,50µm,Cathode	119.681	110.727	1.237	1.731	255	0	255
240 min,10µm,Cathode	104.405	96.393	1.266	1.866	255	0	255
240 min,3µm,Cathode	103.252	94.389	1.302	2.003	255	0	255
240min,500mm,Cathode	78.738	71.791	1.296	2.060	255	0	255
360 min,2mm,Cathode	128.992	127.426	1.039	1.119	255	76	331
360 min,50µm,Cathode	76.864	69.235	1.470	2.908	255	0	255

Sample Image Label	Ra	Rq	Rku	Rsk	Rv	Rp	Rt
360 min,10µm,Cathode	97.095	89.890	1.307	2.094	255	0	255
360 min,3µm,Cathode	94.678	87.759	1.278	1.969	255	0	255
360 min,1µm,Cathode	93.285	86.242	1.284	1.977	255	0	255
360 min,500nm,Cathode	79.299	71.734	1.342	2.218	255	0	255
120 min,2mm,Anode	151.888	149.898	1.041	1.117	255	61	316
120 min,500mm,Anode	88.241	81.285	1.263	1.877	255	0	255
120 min,1µm,Anode	85.792	79.167	1.254	1.868	255	0	255
120 min,5µm,Anode	96.291	89.742	1.308	2.148	255	0	255
120 min,10µm,Anode	95.707	88.797	1.314	2.146	255	0	255
120 min,50µm,Anode	93.920	84.694	1.432	2.613	255	0	255
180 min,2mm,Anode	155.080	152.316	1.054	1.152	255	75	330
180 min,50µm,Anode	89.547	79.882	1.361	2.170	255	0	255
180 min,10µm,Anode	92.543	85.033	1.279	1.908	255	12	267
180 min,3µm,Anode	96.664	90.163	1.222	1.700	255	23	278
180 min,1µm,Anode	96.032	89.726	1.211	1.662	255	16	271
180 min,500nm,Anode	94.741	88.636	1.218	1.702	255	33	288
300 min,50µm,Anode	95.030	83.355	1.422	2.423	255	0	255
300 min,10µm,Anode	95.236	88.178	1.259	1.849	255	0	255
300 min,5µm,Anode	96.201	89.345	1.237	1.761	255	0	255

Sample Image Label	Ra	Rq	Rku	Rsk	Rv	Rp	Rt
300 min,3µm,Anode	96.074	89.421	1.227	1.720	255	0	255
300 min,500nm,Anode	95.245	88.992	1.212	1.670	255	5	260
300 min,1µm,Anode	98.728	92.601	1.207	1.655	255	14	269
300 min,10µm,Anode	95.276	88.177	1.275	1.937	255	0	255

Between Figure 4.137 to Figure 4.160 shows, the physical surface plots and grayscale images of SEM on the surface of the Al samples at the anode and cathode at different process time in minutes under the influence of He plasma are displayed. It is possible to notice black dots and patches that are almost gray in these sample fields of grains. On the surfaces of the Al pellets, the surface plots obtained from the SEM exhibited both hills (areas of higher elevation) and holes (areas of lower elevation).

In order to make comparisons using reliability graphs, the material reliability will be determined using optical roughness parameters at both the Al anode pellets and the cathode pellets. These data will demonstrate the current state of the surface properties that are being measured for optical roughness. In figure 4.161 shows the SEM Al surface observation images and their 3D surface of anode and cathode pellets with different process time under He plasma. Therefore, the criteria for material selection will be established for plasma-based energy structures such fusion Tokamak reactors or space thrust systems based on fusion architecture.

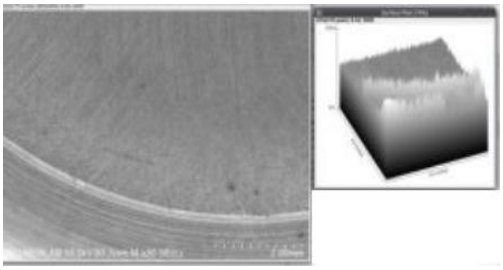

a)60 min, 2mm, Cathode image

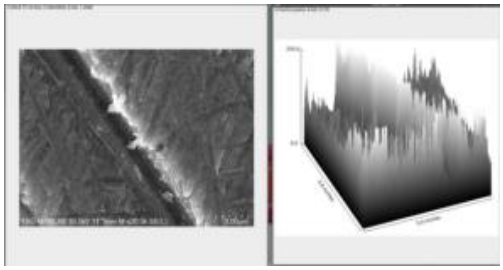

b)240 min,3µm,Cathode image

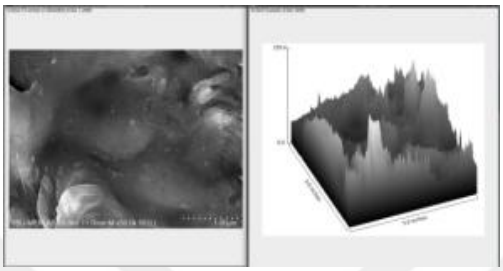

c)360 min,1µm, Cathode image

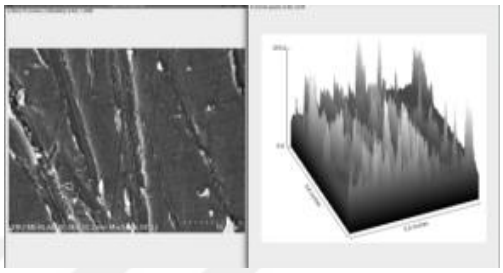

d)120 min,10µm,Anode image

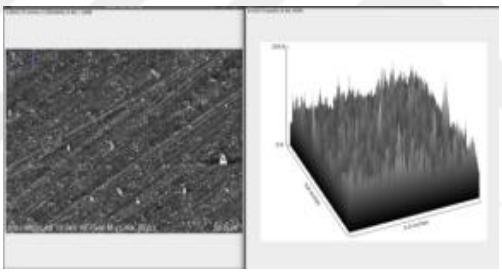

e)300 min,50µm, Anode image

Figure 4.161 a), b), c), d), e) show SEM Al surface observation images and their 3D surface of anode and cathode pellets with different process time under He plasma

The findings shown above are used as a basis for comparing the observations presented in Table 4.1 with the AFM measurements. The research is conducted using an atomic force microscope (AFM), and the measurements are taken very precisely. Additionally, the method is based on the standard-defined terminology Sa and RMS values provided by ASME B46.1. The ASME B46.1 standard states that the terms Sa (surface roughness) and RMS (root mean square) both indicate surface roughness; nevertheless, the calculations for each of these terms are distinct from one another. The average height of a surface's microscopic peaks and valleys is what is used to determine Sa, which is the surface's overall roughness. The root mean square of a

surface that is measured by microscopic peaks and valleys is the value that is used to calculate RMS. The optical roughness parameters were determined in the study that was presented earlier by applying the ImageJ program to the SEM images that were subjected to various plasma processing periods. The following graphs were produced for the common process times given in both techniques by using Table 4.1 and table 4.4 and the study.

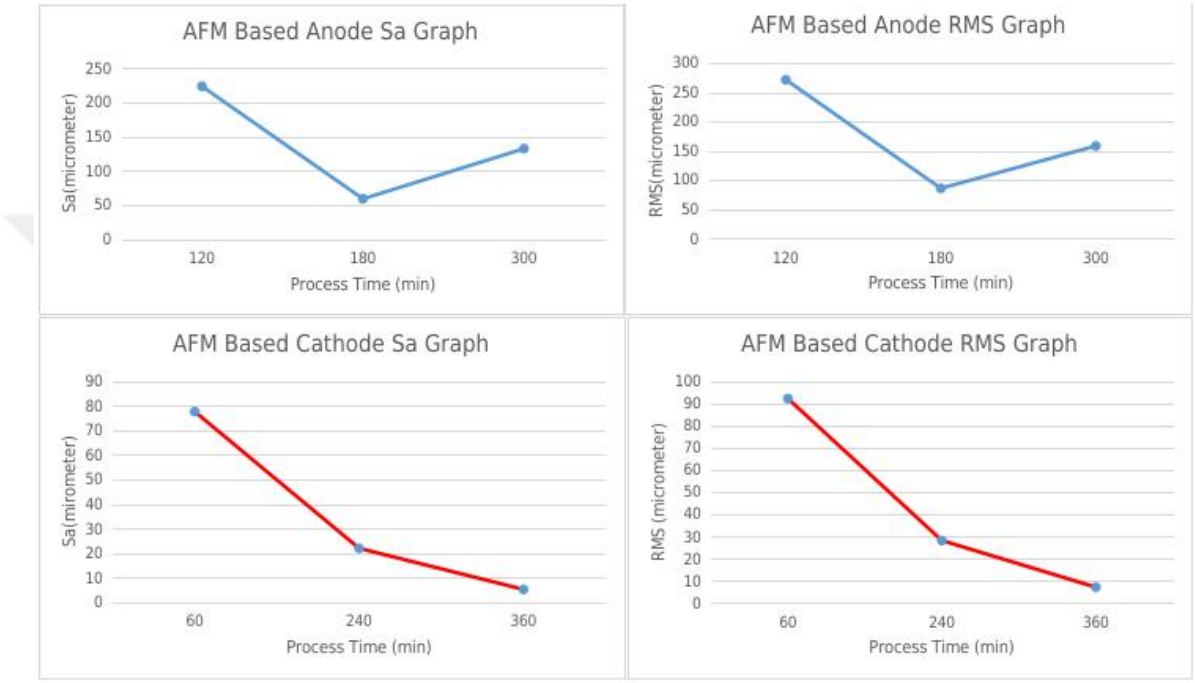

Figure 4.162 AFM Measured RMS and Sa Graphs of Anode and Cathode Surface Pellets Based on Different Process Times (min)

The AFM measurements of anode and cathode pellets both result in the production of the identical graphs, which are based on the results presented in Table 4.1 for the various process times. For these particular SEM images, the Ra and Rq values represent the measured optical roughness, and they were obtained through the use of the ImageJ software. The anode and cathode surfaces of Ra and Rq are seen in Figure 4.163 at the times indicated in Figure 4.162, which are the specified process timings.

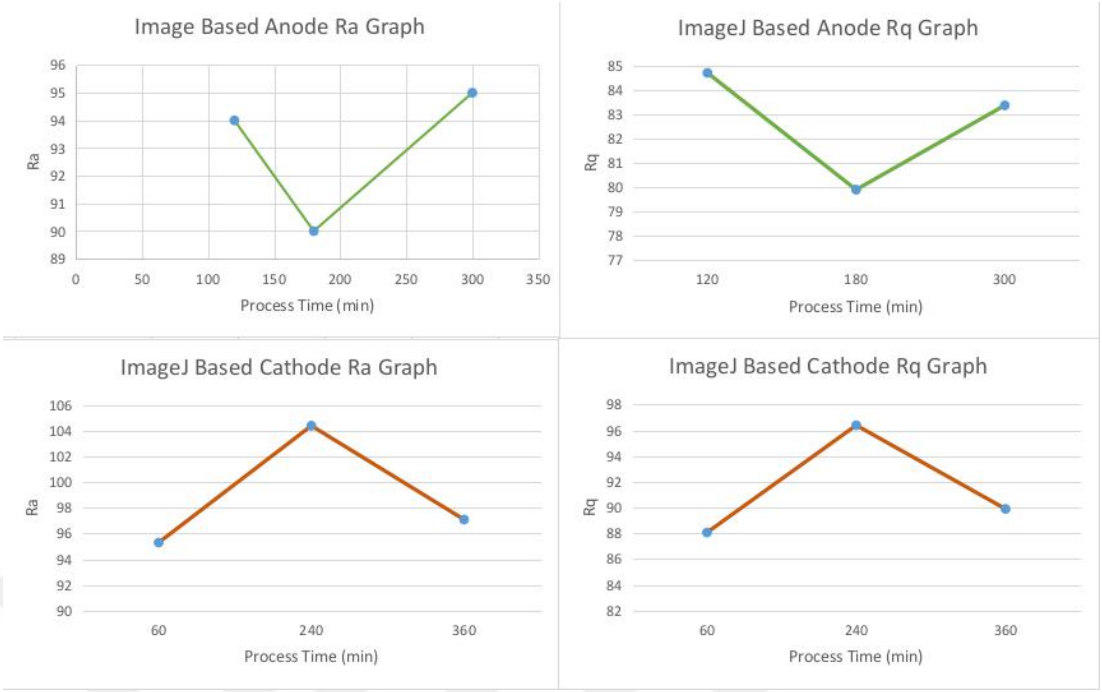

Figure 4.163 ImageJ Software Measured Rq and Rq Graphs of Anode and Cathode Surface Pellets Based on Different Process Times (min)

The correlation function is utilized to make the comparison between the two measurements in order to find out whether or not Ra values can be used for Sa and Rq values can be used for RMS. A statistical measure of strength that is used to determine the linear relationship that exists between two variables is called the correlation function. After receiving the input of the correlation between the two series, the correlation function will then map the range of the output to be between -1 and 1. A correlation value of -1 indicates a perfect inverse correlation, whereas a correlation coefficient of 1 indicates a perfect positive correlation. A correlation coefficient of 0 indicates no association at all. If the correlation coefficient is equal to zero, it indicates that the values do not have a linear relationship with one another. computing the correlation between two sets of data requires first determining each series' standard deviation and then computing the covariance between the sets. The correlation coefficient can be calculated by taking the covariance and dividing it by the product of the standard deviations of the two variables.

Table 4.5 He Plasma Al Anode and Cathode Plates AFM Measurements (Sa and RMS) and ImageJ Calculations (Ra and Rq) Correlation Results

Correlation Table	AFM Measurement of Anode for Sa	AFM Measurement of Anode RMS	AFM Measurement of Cathode for Sa	AFM Measurement of Cathode RMS
ImageJ Measurement of Anode Ra	0,711678358			
ImageJ Measurement of Anode Rq		0,92994807		
ImageJ Measurement of Cathode Ra			-0,468889172	
ImageJ Measurement of Cathode Rq				-0,474880479

According to Table 4.5, AFM recorded anode Sa and RMS values, while ImageJ estimated Ra and Rq values for the same processing duration, which shows a positive correlation above 0 for both sets of results. The values of AFM measured cathode Sa and RMS ImageJ computed Ra and Rq have a negative correlation with one another.

CHAPTER 5

CONCLUSIONS

The The Tokamak reactor is designed to obtain energy through the fusion reaction based on the combination of D and T nuclei, which are isotopes of hydrogen. One of the most important problems in fusion reactors is the interaction of tritium and helium nuclei with Al, C, Be, and W used in reactor construction. Tritium is a radioactive material, and its retention by these materials can make the material itself radioactive. In the long run, the Tokamak reactor may turn into a gigantic radioactive material. Therefore, it is very important to determine the material with the least tritium retention. The product resulting from the He nucleus reaction is the nucleus.

The ions must be continuously evacuated from the reactor. However, the nuclei cause erosion in the materials they hit, both during evacuation and because they escape from the magnetic field environment due to their heavy weight. For this reason, determining the material with high resistance to He nuclei is an important issue that must be determined in advance in reactor design.

In the first part of the study, the interactions of H, D, and He ions with Al, C, Be, and W, which are used as plasma meeting materials in the Tokamak reactors, were examined using molecular dynamics and Monte Carlo simulation techniques. From the molecular dynamics simulation results, it was seen that W was the material with the lowest total spray efficiency. This result shows that the material with the highest radiation resistance that can be used in the reactor is tungsten (W). Monte Carlo simulation results, physical spraying efficiency, chemical erosion efficiency, and radiation-enhanced sublimation calculations were carried out as a result of the interaction of H, D, T, and He ions with graphite. Results of the physical sputtering efficiency of He nuclei showed that chemical erosion efficiency was highest with In addition, the surface temperature varies depending on the plasma density (number of ions), and the number of atoms detached from the surface is a measure of the plasma energy. It was observed that it increased very rapidly after the threshold value (about 450 eV).

As stated in the theoretical results, hydrogen and helium atoms affect the surface wall structure material candidates (tungsten, aluminum, and diamond) of the Tokamak reactors in space applications. Hydrogen has less effect on tungsten and aluminum, as shown by 3D models. Plasma-material interactions affect the magnetic fusion device's operations. A sample of highly charged particles on the fusion wall structure can sputter particles into the plasma from the magnetic fusion devices. The molecular dynamics simulation showed that W had the lowest total sputtering yield. Tungsten (W) reactors are radiation-resistant. Physical sputtering yield, chemical erosion yield, and radiation-enhanced sublimation were evaluated using H, D, T, and He ions interacting with graphite (C). Physical and chemical sputtering were highest in cores. Plasma density (ion number) affects surface temperature, and atom removal accelerates above 450 eV. JET vacuum reactor walls use Be and W. Be possesses good heat conductivity, gettering, plasma impurity tolerance, and low nuclear activation, according to research. H-based deterioration and tritium retention occur during tests. Plasma purity is affected. Graphite walls are used in experimental reactors. Graphite crystals absorb too many plasma H atoms. Tungsten melts at high temperatures and resists heat, and construction engineers prefer to use it in fusion reactors and structures. The Tokamak reactor walls use beryllium instead of graphite. In 2011, JET tested new H-graphite molecular limits. Fusion reactors benefit from beryllium's thermal and mechanical properties. The ITER reactor and Tokamak divertor walls have tungsten and beryllium. The Tokamak reactor divertor regions employ aluminum, not beryllium. It's cheap and easy to supply as a material. He dramatically modifies its metal crystal structure. The interaction with the Al crystals creates retention in the bulk material. Under Be, C, and W, it melts. Studies of molecular dynamic models also provide these results. The model showed low tungsten sputtering yield love, followed by Be, Al, and C with similar visual values. Calculations suggest that tungsten (W) is best for Tokamak reactors' H, D, and He ions, but it retains tritium; hence, tritium-facing components should be Al or graphite.

In the experimental part of the study, a linear plasma designed in a laboratory environment was used. The interaction of He ions and the aluminum surface in the system was examined. Al surfaces interact with the plasma for periods of 60, 120, 180, 240, 300, and 360 minutes. The processed Al pellet surfaces are observed by

metal microscopy and analyzed under an atomic force microscope. Then the surface is magnified in high resolution under SEM and the chemical analysis of the surface is assessed with the EDS.

After a period of 360 minutes of He plasma exposure to Al material, physical retention deformation occurs on the surface. The material surface showed swells, which are caused by the retention of Al particles from cathode to anode. The surface roughness is assessed with AFM physically, and the surface is also analyzed with the ImageJ software to calculate the optical roughness values of the SEM images. The reliability of the material was determined using the Weibull prediction method using the surface roughness values resulting from the images. Experimental results conclude that Weibull distribution is a tangible method for calculating reactor wall plasma-material interaction structural dependability. This method is widely used in aviation and the military to estimate structural reliability by identifying material fault factors quickly. Before doing the experimental work like in this study, molecular dynamic simulations of reactor structural models can be performed. This will save the money before the experimental costs occur. Based on the Weibull reliability prediction calculations, Helium plasma etching of the cathode Al surface showed less surface deformation than the anode surface. The anode surface shows the Al retention physical deformations based on the surface roughness measurements. So that the Weibull reliability calculations of the anode also reflect this issue. The electron beam harmed the cathode sample as ion particles accumulated on the anode aluminum sample. Al parts are collected on the anode surface to create degradation. Due to the insolubility of non-metals like He plasma on the Al surface, our study showed that He can diffuse a long channel and self-trap at kinetic energies below the metal displacement threshold to form vacancy defects. He vacancy complexes the trap. He atomizes until hill-type surfaces solidify. When these reactions occur near the surface, metal atoms flake and create nanofiber structures. He neutrals are backscattered on the Al surface to react as He ions in metals. Atoms of Al boost surface mobility and kinetic energy so that the coupled mechanisms create porous microstructures. Results show that material safety increases exponentially as a function of irradiation time, showing that it is decreasing. This situation shows that it is not appropriate to use Al in parts where He plasma is discharged.

AFM and metal microscope reliability calculations show the results of these activities. AFM measurements to find the surface roughness parameters using Weibull reliability calculations cost time and money for the assessment of the surfaces. In order to eliminate these costs, replacing the surface roughness parameter with optical roughness measurements can be efficient. In this study, optical roughness measurements based on SEM images are used in a cost-effective manner. Optical roughness surface parameters and surface roughness parameters are compared by using the correlation function. According to the findings, ImageJ optical roughness parameters showed a positive correlation for anode pellet surfaces, while the cathode area resulted in a negative correlation. The reasons for the negative correlation results are assessed. The number of sample images of Cathode Al surface images is less, and more sharp resolution images should be taken. However, it is not an easy way to generate SEM images over time. SEM analysis is expensive in terms of time and money to generate images. Metal Microscope images are the most cost-effective and time-efficient way to photograph Al pellets. Metal microscope photos generate more image samples. The more samples of metal microscope images, the faster the optical roughness measurements in ImageJ software. So these findings can be used to correlate positively with the AFM surface roughness parameters. This will show a positive finding for future uses of this study. Future investigations using exact samples and computations of metal microscope images generated by optical roughness parameters can be used in material reliability estimations. This fact can be used in many quality control processes in industries that use plasma. For example, in the aviation and defense industries, structural reliability estimation processes will be cheaper, and they can also be used in the energy production field in selecting material acquisition processes. The five material-structural dependability approaches are well-established in reliability literature. Heat, stress, erosion, material choice, dependability analysis, upkeep, and inspection. Massive Tokamak fusion reactor experiments do not study material structural reliability prediction and calculation methods when the literature is analyzed. Cost is the main priority in Tokamak fusion reactor construction and design. Operation requires maintenance and material durability. Experts should calculate fusion reactor robustness and operational costs, including material life cycle and maintenance.

In summary, when theoretical and experimental results in this study are evaluated together, in the Tokamak reactors, tungsten (W) is the most suitable material that is resistant to H, D, and He ions. However, tungsten has a high retention of tritium, and it is not suitable for facing tritium ions. Where tritium is an issue in reactors, it is concluded that it is appropriate to make the parts from aluminum or graphite.

Future material theoretical simulation models and experimental research with active plasma characteristics like plasma collisionality and relative sputtering yields on structural material surfaces can leverage the Weibull approach for plasma material interactions. The structural material dependability of the nuclear fusion reactors is studied using five methods, according to reliability literature. Material selection, dependability analysis, maintenance and inspection, heat and stress, erosion, and damage. Maintenance and material resilience are other operational problems. Experts should include material life cycle and resilience maintenance costs to compute the operational costs of the nuclear fusion reactors. Construction and operation material reliability data affects life cycle costs. There is no study that uses material reliability prediction in nuclear fusion reactor experiments. Only surface-coated commercial plasma material dependability studies exist in the literature. For nuclear fusion reactors, reliability data must include fault data such as fatigue, crack, and deformation parameters. So that the parameters can improve fusion reactor structural material reliability evaluations in the operational and maintenance phases. This work directly integrates material surface roughness with plasma processing fault data to calculate the material structure's characteristic curve using the Weibull prediction method. This study provides a cost-effective approach to material selection and structural reliability analysis of the Tokamak fusion reactor design and planning.

REFERENCES

[1] Ongena, J. Nuclear fusion and its large potential for the future world energy supply. Nukleonika Journal, *(61),* 425-432. 2016

[2] Takeda, S., & Pearson, R. (Eds.). Nuclear Fusion Power Plants. *Power Plants in the Industry*. (101-122). IntechOpen publishing. 2018

[3] Guo, J., & Du, X. Reliability Analysis for Multidisciplinary Systems with Random and Internal variables. AIAA Journal, *(48),* 82-91. 2012

[4] Haider, Q. Nuclear Fusion: Holy Grail o Energy. *Nuclear Fusion.* (1-17). IntechOpen publishing. 2019

[5] Braams, J. (Ed). *Atomic and Plasma Material Interaction Data for Fusion*. IAEA. (15th ed.) (11-73). 2007

[6] Chudakov, M. & Malavasi, A. (Eds.). Clean Energy through Fusion Technology: A Sun on Earth. *Fusion Energy for Peace and Sustainable Development*. (2-18). IAEA. 2018

[7] Kikuchi, M., Lackner, K. & Tran Q. (Eds.). *Fusion Physics*. (20-21). IAEA. 2012

[8] Ibrahim, S., Lahboub, Z., Brault, P., Petit, A., et al. Influence of helium incorporation on growth process and properties of aluminum thin films deposited by DC Magnetron sputtering. Surface and Coatings Technology, *(426),* (2-22). 2021

[9] Behrish, R., & Harries R. Lifetime Predictions For The First Wall and Blanket Structure of Fusion Reactors. Nuclear Fusion Journal, *(26),* 685. 1986

[10] Braams, C. M. & Stott P. E. (Eds.). Nuclear Fusion. *Half a Century of Magnetic Confinement Fusion Research*. (230-258), IoP Publishing Ltd. 2002

[11] Jones, E. S. & Rafelski, J. Cold Nuclear Fusion. Scientific American. *(257)*, 84-89. 1987

[12] Kajita, S., Kawaguchi, O. N., Yoshida, N. Enhanced growth of large-scale nanostructures with mettalic ion precipitation in helium plasmas. Scientific Reports. *(8),* 56. 2018

[13] Kotov, V. Particle conservation in numerical models of the Tokamak plasma edge. Physics of Plasma. *(24),* 4. 2017

[14] Wojcyzkowski, K., N*ew Development in Corrosion Testing: Theory, Methods and Standards*. PF Products Finishing. Accessed at 20 November 2023. Available at: https://www.pfonline.com/articles/new-developments-in-corrosion-testing-theory-methods-and-standards

[15] Linden, T. *Compact Fusion Reactors*. Retrieved November 20, 2023, from http://cds.cern.ch/record/2004827. March 2015

[16] Rajablou, L., Motevalli, S. M., Fadaei, F. Study of alpha particle concentration effects as the ash of deuterium-tritium fusion reaction on ignition criteria. Physica Scripta. *(97)*, 9. 2022

[17] Malo, M., Morono, A., Hodgson, E. R., Plasma Etching to Enhance the Surface Insulating Stability of Aluminumina for Fusion Applications. Nuclear Materials and Energy. *(9),* 247-250. 2016

[18] Miyamoto, K., (Ed.). Fundamentals of Plasma Physics and Controlled Fusion (3rd Ed.) (1-21). CreateSpace Independent Publishing Platform, 2011

[19] Nadler, J., Inertial-Electrostatic Confinement (IEC) of A Fusion Plasma with Grids. Retrieved November 20, 2023 from http://sites.apam.columbia.edu/SMproceedings/11.ContributedPapers/11.Nadler.pdf

[20] Nordlund, K., Atomistic Simulations of Plasma-wall interactions in Fusion Reactors. Physica Scripta. *(T124),* 53-57. 2006

[21] Jefferson, M., *Energy Efficiency and Sustainability*. Proceedings of the 44th Season of the International Seminar on Nuclear War and Planetary Emergencies. *(70),* August Chapter. 2011

[22] Perrault, D., Nuclear Fusion Reactors-Safety and Radiation Protection Considerations for Demonstration Reactors that follow ITER facility. IRSN. *(Nov),* 15-27. 2017

[23] Krivosheev, M. V., & Kolbasov N. B., Safety of Fusion Reactors. *Fundamentals of Magnetic Thermonuclear Reactor Design.* (401-432). Woodhead Publishing Series in Energy. 2018

[24] Nakashima, N. H., The Crystallography of Aluminum and Its Alloys. *Encyclopedia of Aluminum and Its Alloys*. (488 – 586). CRC Press. 2018

[25] Xinruo, L., Nie, X., & Northwood, D. DC mode plasma electrolytic oxidation of aluminum alloys for corrosion protection. 46th Annual Conference of the Australasian Corrosion Association-Corrosion and Prevention, *(2006),* 219-226. 2006

[26] Pahsa, A., Modelling Plasma Material Interactions in Spacecraft Magnetic Fusion Devices. 9th International Conference on Recent Advances in Space Technologies (RAST), *(2)*, 655-662. 2019

[27] Kotov, V., Particle conservation in numerical models of the tokamak plasma edge. Physics of Plasmas, *(24-4),* 042511. 2017

[28] Rapp, J., Temmerman, D. G., Van RoolJ, G. J., et al. Plasma Facing Materials Research For Fusion Reactors At Fom Rijnhuizen. Journal Of Physics, *(56),* 30-35. 2011

[29] Malo, M., Morono, A., Hodgson E. R. Plasma Etching to Enhance the Surface Insulating Stability of Aluminum for Fusion Applications. Nuclear Materials and Energy, *(9),* 247-250. 2016

[30] Watson, R. D., Peterson, R. R., & Wolfer, W. G., Lifetime Analysis of Fusion Reactor First Wall Components. Journal of Vessel Technology, *(105)*, 144-152. 1983

[31] Cronwall, O. (Ed.). Structural Lifetime, Reliabiliy and Risk Analysis Approaches for Power Plant Components and Systems. Finland: VTT Publications. 2011

[32] Du, X., Unified Uncertainty Analysis by the First Order Reliability Method. Journal of Mechanical Design, *(30),* 091401-09410. 2008

[33] Zhao, Y., & Ono, T., Generated Procedure for First/Second Order Reliability Method (FORM/SORM). Structure Safety, *(21),* 95-112. 1999

[34] Guo, J., & Du, X., Reliability Analysis for Multidisciplinary Systems with Random and Internal variables. AIAA, Journal, *(48)*, 82-91. 2010

[35] Yan, M., Sun, B., Liao, B., Ren, Y. et al. Out-Crossing Combined Time-Variant Reliability Analysis Method for Ship Structures. IEEE Access, *(6),* 9723-9732. 2018

[36] Adegbulugbe, A. O. Comparison of lifetime calculation for fusion reactor first walls based on two creep fatigue design criteria. Nuclear Engineering and Design Fusion. *(1)*, 301-305, 1984

[37] Eckstein, W., Preuss, R., New Fit Formulae for the Sputtering Yield, Journal of Nuclear Materials, *(320),* 209-213. 2003

[38] Thompson, A., Monte Carlo Simulations with LAMMPS. Sandia National Laboratories. LAMMPS Users Workshop and Symposium Proceedings. 2015

[39] Conde, L., An Introduction to Langmuir Probe Diagnostics of Plasmas. Surface, ASME B46.1 Surface Texture, *(2019),* 2020

[40] ASME B46.1, Surface Texture (Surface Roughness, Waviness, and Lay). Technical Standards ASME, *(NS-996086)*, 2020

[41] Wojcyzkowski , K, .New Development in Corrosion Testing: Theory, Methods and Standards. AESF Foundation, Plating and Surface Finishing, (98), 2011

[42] Kikuchi, M., Lackner K., Tran, M. Q., (Eds.). Fusion Physics, 20-21. 2012

[43] Freidberg, J.P., Mangiarotti, F.J., Minervini J., Desgining a Tokamak Fusion Reactor-How Does Plasma Physics Fit In?. MIT, *(16),* 2015

[44] Miyamoto, K., Fundamentals of Plasma Physics and Controlled Fusion. (3rd Edition). 1-21, 2011

[45] Brams, C. M. & Scott P. E., Nuclear Fusion-Half a Century of Magnetic Confinement Fusion Research. Plasma Physics and Controlled Fusion, *(44),* 230-258. 2002

[46] Chan, A. Y., Herdrich, G., & Syring, C. Development of Inertial Electrostatic Confinement in IRS. Space Propulsion Conference, *(SP2016)*, 3125348 .2016

[47] Jones, E. S., & Rafelski, J. Cold Nuclear Fusion. Scientific American, *(257),* 84-89. 1987

[49] Deshpande, S. P., Raole, P. M., et al. Simulation of Radiation Damage and Ion Irradiation Experiments with Tungsten. Atomic and Plasma-Material Interaction Data for Fusion, *(18),* 3-49. 2012

[50] Petkow, D., Gabrielli, R. A., et al. Generalized Lawson criterion for magnetic fusion applications in space. Fusion Engineering and Design, *(87),* 30-38. 2012

[51] Rene, A., Iglesias, R., & Cerdeira, M. A. Materials to Be Used in Future Magnetic Confinement Fusion Reactors: A Review. Materials, *(15),* 6591. 2022

[52] Motevalli, S. M., Dashtban, N., & Maleki, M. Determination of optimum conditions in ITER tokamak by using zero-dimensional model. Indian Journal of Physics, *(94),* 1-7. 2020

[53] Selinger, T. S., Schimid, K., et al. Latest results of Eurofusion plasma-facing components research in the areas of power loading, material erosion and fuel retention. Nuclear Fusion, *(62)*, 4. 2022

[54] Sindhu, S., Nehra, V., & Malik, S. C. Reliability estimation of photovoltoic system using Markov processes and dynamic programming approach. International Journal of Reliability and Safety, *(1),* 132-151. 2017

[55] Eaton, D. C. G., Pradier, A., & Lambert, M. Technical Note: New structural materials for space applications. International Journal of Materials and Product Technology, *(6),* 68-80. 2014

[56] Abdelrahman, M. M. Study of Plasma and Ion Beam Sputtering Processes. Journal of Physical Science and Application, *(5)*, 128-142. 2015

[57] Ukar, E., Lamikiz, A., Martinez S., et al. Roughness Prediction on laser polished surfaces. Journal of Materials Processing Technology, *(212)*, 1305-1313. 2012.

[58] Bowler, M. G. Self-Sustaining Nuclear Reactions and Nuclear Energy Sources. *Nuclear Physics* (1st ed.) (300-357). Oxford. Pergamon Press. 1973.

[59] Castro, D. A. Use of Nitrogen Compounds for Tritium Retention and Tungsten Sputtering Control in Nuclear Fusion Reactors. Pubslished Phd Dissertation, Universidad Rey Juan Carlos. 2015

[60] Sefta, F. Surface Response of Tungsten to Helium and Hdyrogen Plasma Flux as a Function of Temperature and Incident Kinetic Energy. Published Phd. Thesis, University of California. 2013

[61] Akgün, Y. Düşük Enerjili Plazma Odak Füzyon Cihazı Yapıı ve Nötronik Ölçümler. Yayınlanmış Doktora Tezi, Ankara Üniversitesi. 2010

[62] Teke, E. Vakum Ortamında Plazma Kaplama ve Plazma Parametrelerinin İncelenmesi. Yayınlanmış Yüksek Lisans Tezi, Isparta Süleyman Demirel Üniversitesi. 2012

[63] Somboonkittichai, N., & Zuo, G. Numerical Study of Heat Transport in Static Liquid Metal Exposed to Plasma with Magnetic Field. Plasma and Fusion Research, *(18),* 2403027. 2023

[64] Petty, C. C., et al. DIII-D research towards establishing the scientific basis for future fusion reactors. Nuclear Fusion, *(59),* 112002. 2019

[65] Görür, A. Görünür Spektrumdaki Işımanın Plazma Ortamında Soğrulması ve Plazma Parametrelerinin İncelenmesi. Yayınlanmış Doktora Tezi, Erciyes Üniversitesi. 1992

[66] Gürsoy, G. Low Pressure Glow Discharge Plasma Diagnostics. Published Master Thesis, Yeditepe University. 2012

[67] Sakal, M. Nükleer Füzyon Enerjisi Üreten Reaksiyonlarda Kullanılan Çekirdeklerin Yapılarının İncelenmesi. Yayınlanmış Yüksek Lisans Tezi, Osmaniye Korkut Ata Üniversitesi-Mustafa Kemal Üniversitesi. 2015

[68] Sullivan, R. Preliminary density and temperature measurements in Lockheed Martin's magnetically encapsulated linear ring cusp confinement configuration. Proceedings of 57th of Annual Meeting of the APS Division of Plasma Physics, *(60)*, YP12. 2015

[69] Miley, G. H. & Murali K. S. Background, Basics, and Some IEC Experiments. *Inertial-Electrostatic Confinement (IEC) Fusion Fundamentals and Applications* (1st ed.) (1-29). Springer. 2014

[70] Radel, F. R. Detection of Highly Enriched Uranium and Tungsten Surface Damage Stuies Using a Pulsed Inertial Electrostatic Confinement Fusion Device. Published Phd. Dissertation, University of Wisconsion. 2007

[71] Chan, A. Y., Herdrich, G., & Syring, C., Development of Inertial Electrostatic Confinement in IRS. Proceedings of Space Propulsion Conference, (*SP2016*), 3125348. 2016

[72] Krupakar, M. S., Diagnostic Study of Steady State Advanced Fuel (D-D and D-3He) Fusion in an IEC Device. Published Phd. Thesis, University of Wisconsion. 2004

[73] Takashi, H., Atsushi, O., et al. Helium Volumetric Recombining Plasma Formation for Energetic Ion Injection in Radio-Frequency Plasma Device DT-Alpha. Plasma and Fusion Research: Regular Articles, *(11),* 2402059. 2016

[74] Yu, Z., Inertial Electrostatic Confinement (IEC) Device as Plasma Injection Source. Published Master Thesis, University of Washington. 2015

[75] U.S. Department of Energy, Office of Science, Fusion Energy Sciences. Report on Science Challanges and Research Opportunities in Plasma Material Interactions. (OSTI Identifier: 1414414). New Jersey, United States; USDOE. 2015

[76] Clark, R. E. H. (Ed.) Atomic and Plasma Material Interaction Data for Fusion, IAEA, *(13),* 1-112. 2007

[77] Şerer, B., Hançerlioğulları, A., & Savruk, N. A. Design For APEX Fusion Reactor Model By Using Monte Carlo Method. Gazi Üniversitesi Fen Bilimleri Dergisi, *(18)*, 201-2010. 2005

[78] Kripner, L. Distribution of power fluxes to plasma-facing components of a Tokamak due to edge-localized modes. Published Master Thesis, Charles University. 2016

[79] Airilia, M, & Hakola A. (Eds.). Fusion Yearbook Association Euratom-Tekes Annual Report 2013. Finland: VTT Science Publications. 2014

[80] Ruiz, J.A., Rivera A., et al. Plasma-wall interaction in laser inertial fusion reactors: novel proposals for radiation tests of first wall materials. Plasma Physics and Controlled Fusion, *(54)*, 124051. 2012

[81] Brooks, J. N., Hassanein, A., et al. Scientific and Computational Challanges in Coupled Plasma Edge/Plasma-Material Interactions for Fusion Tokamaks. Plasma Physics, *(54),* 329-340. 2014

[82] Kreter, A. Reactor-Relevant Plasma-Material Interaction Studies in Linear Plasma Devices. Fusion Science and Technology, *(59)*, 51-56, 2017

[83] Ohya, K. Progress in Modeling erosion and redeposition on plasma facing materials. Journal of Nuclear Materials, *(415)*, 10-18. 2010

[84] Brooks, J. N., Allain, J. P., & Rognlien T. D. Plasma Material Interactions (PMI) Thrust for Enhancing Modeling Predictive Computations. ReNEW Meeting Workshop, UCLA 2009. Date Retrieved November 2023. Available from Slideplayer web site (https://slideplayer.com/slide/3846428/). 2023

[85] Hassanein, A., Sizyuk, V., & Miloshevsky G. (PMI) Thrust for Enhaning Modeling and Simulation of Various Plasma Instabilities with Innovative Mitigation Techniques, DOE ReNeW Process Workshop, UCLA, 2009. Date Retrieved November 2023. Available from UCLA web site (https://cestar.seas.ucla.edu/FNST/Renew_Presentations/Thursday/8-Hassanien-HEIGHTS-PWI-for.pdf). 2023

[86] Zanino, R. Advanced Finite Element Modeling of the Tokamak Plasma Edge. Journal of Computational Physics, *(138)*, 881-906. 1997

[87] Yang, X. Atomistic Simulation of Plasma Interaction With Plasma Facing Components In Fusion Reactors. Published Phd Dissertation, Purdue University. 2013

[88] Esquisabel, A. L. Atomistic Simulations of Divertor-Plasma Interations in Fusion Reactors. Published Academic Dissertation, University of Helsinki. 2014

[89] Nordlund, K. Atomistic Simulations of Plasma-wall interactions in Fusion Reactors. Physica Scripta, (*T124*). 53-57. 2006

[90] Blanken, C. T., Felici, F. et al. Control-oriented modeling of the plasma particle density in tokamaks and application to real-time density profile construction. Fusion Engineering and Design, *(126)*, 87-103. 2018

[91] Rapp, J., Temmerman, D. G., et al. Plasma Facing Materials Research For Fuision Reactors At Fom Rijnhuizen. Romania Journal Of Physics. *(56)*. 30-35. 2011

[92] Diegele, E., Beghini, M., et al. Results of the IAEA benchmark on lifetime predictions of first wall components. Journal of Nuclear Materials, *(233-237),* 62-71. 1996

[93] Bittencourt, J. A. Fundamentals of Plasma Physics (3rd Ed.). Springer. 2004

[94] Haikel, J., & Benredjem, D. (Eds). Plasma Science and Technology (3rd ed.) 47-66. IntechOpen. 2019

[95] Brault, P., Chuon, S., & Bauchire, J. M. Molecular Dynamics Simulations of Platinum Plasma Sputtering: A Comparative Case Study. Front. Physcs, *(4),* 20. 2016.

[96] Doerner, R. P., Whyte, D. G., & Goebel, D. M. Sputtering Yield of measurements During Low Energy Xenon Plasma Bombardment. Journal of Applied Physics, *(93)*, 5816-5823. 2003

[97] Nordlund, K., Björkas, C., et al. Multiscale modelling of plasma-wall interactions in fusion reactor conditions., Journal of Physics D: Applied Physics, *(47),* 224018. 2014

[98] Schwerdfeger, P., Burrows, A., & Smits, O. R. The Lennard-Jones Potential Revisited: Analytical Expressions for Vibrational Effects in Cubic and Hexagonal Close-Packed Lattices. Journal of Physical Chemistry, *(125),* 3037-3057. 2021

[99] Desai, A. M., Mesquita, N., & Fernandes, V. A new modified Morse potential energy function for diatomic molecules. Physica Scripta, *(95),* 085401. 2020

[100] Daw, S. M., Foiles, M. S., & Baskes, I. M. The embedded-atom method: a review of theory and applications. Material Science Reports, *(9),* 251-310. 1993

[101] Atomic Simulation Environment. Documentation. web site retrieved in April, 2019, from https://wiki.fysik.dtu.dk/ase/

[102] Taylor, K. J., Yun, S., & Tynan, G. R. Control of plasma parameters by using noble gas admixtures. Journal of Vacuum Science & Technology A, (22), 2131-2138. 2004

[103] Dejarnette, D. Low-temperature helium plasma generated at atmospheric pressures by a non-standard field applicator. Scilight, *(33),* 330006. 2018

[104] Yamamura, Y., Matsunami, N., & Itoh, N. A new emprical formula for the sputtering yield, Radiation Effects and Defects in Solids, *(68)*, 83-87. 1982

[105] Göktaş, F. Theoretical and Experimental Investigation of Plasma-Wall Interaction and Material Reliability in Fusion Based Tokamak Reactor. (Project No Report: 118F052). Ankara; Turkiye, TÜBİTAK. 2022

[106] Whitehouse, D. Surfaces and their Measurement (1st Ed). (Chps 2-3). Boston: Butterworth-Heineman. 2014

[107] Bramfit, L. B., & Benscoter, O. A. Metallographer's Guide-Practices and Procedures for Irons and Steels (1st Ed). (Chp 5). United States: ASM International. 2002

[108] Metallurgical Microscopes. (n. d.). Retrieved from https://www.kemet.co.uk/products/metallography/microscopes/metallurgical-microscopes

[109] Binnig, G., Qate, C. F., & Gerber, C. Atomic Force Microscope. Physical Review Letters, (56), 930–933. 1986

[110] Swapp, S. *Scanning Electron Microscopy (SEM)-What is Scanning Electron Microscopy*. Date Retrieved November 2023,

https://serc.carleton.edu/research_education/geochemsheets/techniques/SEM.html. November 2023

[111] Schneider, C. A., Rasband, W. S., & Eliceiri, K. W. *Image Processing and Analysis in Java.* Date Retrieved November 2023, https://imagej.nih.gov/ij/docs/index.html. November 2023

[112] Ellingham T. D. S., Thompson, J. U. T., & Islam, M. Scanning Electron Microscopy-Energy Dispersive X-Ray (SEM/EDX): A Rapid Diagnostic Tool to Aid the Identification of Burnt Bone and Contested Cremains. Journal of Forensic Sciences, *(63),* 504-510, *2017*

[113] Girao, A. V.., Caputo, G. & Ferro, C. M., Comprehensive Analytical Chemistry (1st Ed). (Chp 6). Elsevier. 2017

[114] Bian, K., Gerber, C., et. Al. Scanning Probe Microscopy. Nature Review Methods Primers, *(1),* 36. 2021

[115] Voter, A. F. Introduction to Kinetic Monte Carlo Method. Radiation Effects in Solids, *(235)*, 1-23. 2007


ANKARA YILDIRIM BEYAZIT ÜNİVERSİTESİ